AD-A093 109 NAVAL RESEARCH LAB WASHINGTON DC F/6 13/10
NUMERICAL CALCULATION OF SURFACE WAVE EFFECTS ON MARINE STRUCTU--ETC(U)
DEC 80 E W MINER, O M GRIFFIN, S E RAMBERG
UNCLASSIFIED NRL-MR-4395 NL

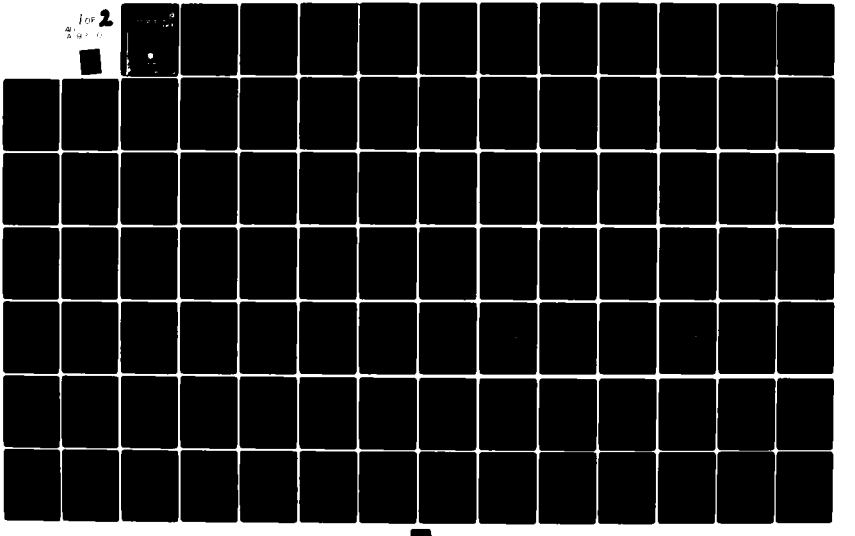

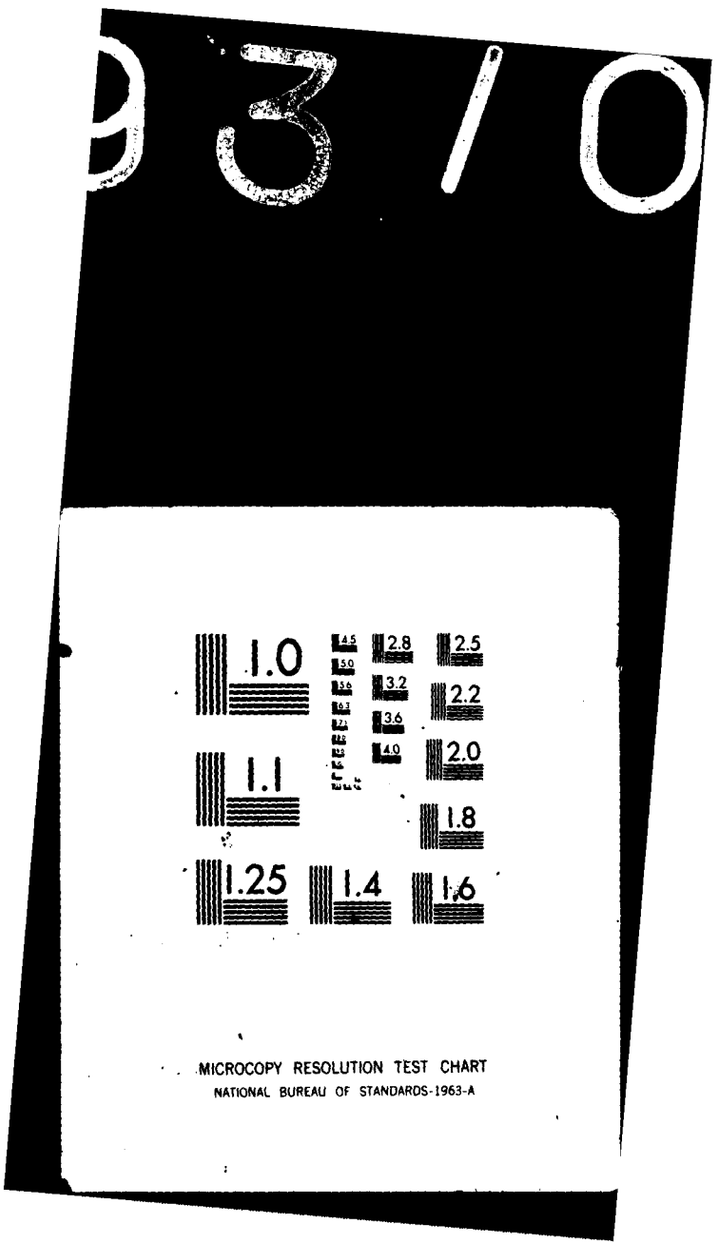
3 / 0
1.0
1.1
1.25
1.4
1.6
2.8
3.2
3.6
4.0
2.5
2.2
2.0
1.8
MICROCOPY RESOLUTION TEST CHART
NATIONAL BUREAU OF STANDARDS-1963-A

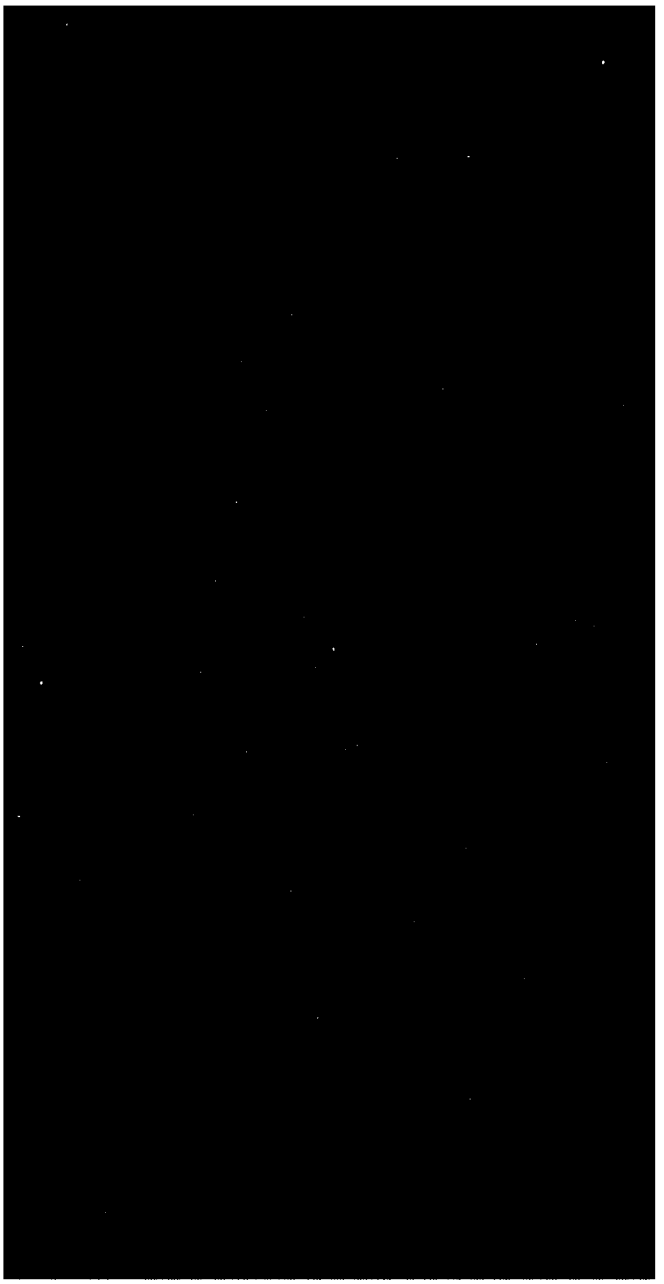

SECURITY CLASSIFICATION OF THIS PAGE *(When Data Entered)*

REPORT DOCUMENTATION PAGE

READ INSTRUCTIONS BEFORE COMPLETING FORM

1. REPORT NUMBER: NRL Memorandum Report 4395
2. GOVT ACCESSION NO.: AD-A093109
3. RECIPIENT'S CATALOG NUMBER: NRL-MR-4395

4. TITLE (and Subtitle): NUMERICAL CALCULATION OF SURFACE WAVE EFFECTS ON MARINE STRUCTURES
5. TYPE OF REPORT & PERIOD COVERED: Interim report on a continuing problems
6. PERFORMING ORG. REPORT NUMBER

7. AUTHOR(s): E.W. Miner, O.M. Griffin, S.E. Ramberg, M.J. Fritts, Laboratory for Computational Physics
8. CONTRACT OR GRANT NUMBER(s)

9. PERFORMING ORGANIZATION NAME AND ADDRESS: Naval Research Laboratory, Washington, DC 20375
10. PROGRAM ELEMENT, PROJECT, TASK AREA & WORK UNIT NUMBERS: 61153N, RR02314, 0273-0-0

11. CONTROLLING OFFICE NAME AND ADDRESS: Office of Naval Research, Washington, DC 22217
12. REPORT DATE: December 1980
13. NUMBER OF PAGES: 97

14. MONITORING AGENCY NAME & ADDRESS *(if different from Controlling Office)*
15. SECURITY CLASS. (of this report): UNCLASSIFIED
15a. DECLASSIFICATION/DOWNGRADING SCHEDULE

16. DISTRIBUTION STATEMENT *(of this Report)*

Approved for public release; distribution unlimited.

17. DISTRIBUTION STATEMENT *(of the abstract entered in Block 20, if different from Report)*

18. SUPPLEMENTARY NOTES

19. KEY WORDS *(Continue on reverse side if necessary and identify by block number)*

Ocean Waves
Marine Structures
Computational Fluid Dynamics
Finite Difference Models
Fluid Mechanics

20. ABSTRACT *(Continue on reverse side if necessary and identify by block number)*

A research program is underway at NRL to develop new methods for the numerical calculation of surface wave effects on marine structures. Sufficient progress has been made with one particular NRL-developed computer code, SPLISH, to demonstrate the attractiveness of numerical calculations for problems such as the wave flow over a submerged structure. A brief description is given in this report of the numerical method and of some recent computational results. The present results demonstrate that realistic time-varying local flow fields, pressures and forces on and near structures such as the half-cylinder on the ocean floor

(continued)

DD FORM 1 JAN 73 1473 EDITION OF 1 NOV 65 IS OBSOLETE
S/N 0102-014-6601

SECURITY CLASSIFICATION OF THIS PAGE *(When Data Entered)*

251950

20. ABSTRACT (Continued)

can be determined from numerical calculations for certain conditions. Comparisons between the numerical results from SPLISH and recent linear and fifth-order solutions for wave flow over a bottom seated half-cylinder show good agreement as do comparisons between the numerical results and experiments in a wave channel.

CONTENTS

NUMERICAL CALCULATION OF SURFACE WAVE EFFECTS ON MARINE STRUCTURES

INTRODUCTION

The effects of ocean waves on man-made structures are of great practical interest, but until quite recently the complexities of the problems have limited theoretical calculations to idealized flows and structural geometries. In the absence of flow separation the complexity arises primarily from the presence of the free surface, particularly if wave-breaking, surging or slamming are involved. Not only does a regular free surface alone easily dominate the flow, but also it usually is accompanied by directional and irregular waves, and wave/current interactions. The development of means to calculate the effects of these complex flows poses intractible problems not only analytically, but also numerically, and only the latest generation of computers has made practical calculations even remotely feasible. This is particularly true for parametric studies which require the calculation of time-dependent flow fields and surface pressure distributions for a variety of body shapes over a spectrum of wave heights, wavelengths, and depth conditions.

A research program is underway at the Naval Research Laboratory to develop means for determining the effects of surface waves on submerged and partially submerged structures in the ocean. One principal thrust of the program has been to develop a capability for the numerical calculation of nonlinear free-surface waves, with verification through comparisons with existing wave theories and force models, and with experiments in a wave channel. The initial stages of this aspect of the research program have centered upon extending the capabilities of the computer code SPLISH which was developed at NRL by Fritts and Boris (1975, 1977b).

Manuscript submitted October 20,1980.

While there are many approaches that might be taken for the numerical calculation of free-surface waves, e.g. the finite-element work of Bai and Yeung (1974) and Wellford (1978), and the marker-and-cell codes of Nichols and Hirt (1977), there are distinct advantages in using a technique which naturally tracks the wave flow field and which employs a grid by which the free-surface and structural boundaries can be readily defined. The non-orthogonal curvilinear coordinate systems developed by Shanks and Thompson (1977) can accommodate irregular boundaries without interpolation but require transformation calculations at each time step. SPLISH couples the advantages of a Lagrangian approach to a triangular grid which can be restructured easily in a conservative, reversible manner to meet the needs of calculations of transient phenomena.

This report presents a description of the numerical method upon which SPLISH is based. The numerical results are compared with linear and fifth-order wave theory results and the numerical and theoretical results are compared with experimental data. For one range of conditions the agreement is good between the present numerical results and results from both theory and experiment, and this agreement seems to validate the SPLISH computer code. However, the results obtained for another set of conditions characterized by large wave reflection illustrate the need for alternate boundary conditions in the code.

THE NUMERICAL METHOD

Ideally, calculation of the effects of ocean waves on a structure should incorporate boundary conditions which permit a spectrum of wavelengths and an adequate range of wave heights for different sea conditions. The modeling of transient phenomena such as surges, wave-breaking, and spray production is necessary in the long term since these phenomena account for a major portion of wave energy dissipation. The SPLISH code is structured to permit calculations in the presence of these complex effects under certain conditions.

For two-dimensional, incompressible, and inviscid fluid flow — which is the situation of concern for calculating free-surface wave flows in the ocean — the governing equations are almost deceptively simple. The equations are the momentum equation

$$\rho \frac{d\mathbf{V}}{dt} = -\nabla p - \rho g \vec{y} \tag{1}$$

and the continuity equation

$$\nabla \cdot \mathbf{V} = 0. \tag{2}$$

Closure of the system of equations is given by the boundary conditions. At solid boundaries, such as the bottom of the channel, the normal velocity is given by

$$V_{\hat{n}} = 0. \tag{3a}$$

At the free surface the pressure (relative to atmospheric) is

$$P = 0. \tag{3b}$$

The periodic boundary conditions used in the current version of SPLISH require (at the sides of the computational region)

$$f(0) = f(\lambda), \tag{4}$$

where f is an arbitrary dependent variable and λ is the wave length, which limits consideration to domains of integral numbers of wavelengths. At the free surface $y = \eta$, dynamic and kinematic boundary conditions on the wave flow are derived by satisfying Bernoulli's equation and by requiring that the substantial derivative

$$\frac{D}{Dt}(y - \eta) = 0. \tag{5}$$

Here η is the time-dependent elevation of a point on the free surface (see Appendix B).

The governing equations are solved by a finite-difference method which was developed especially for use on a triangular grid which moves with the flow. The finite-difference method, the Lagrangian approach, and the triangular grid are discussed in depth in Appendix A and are summarized below.

A Lagrangian grid will distort in any non-trivial flow field, and as grid distortion becomes severe the calculation quickly loses accuracy. However a triangular grid can be manipulated locally in several ways to extend realistic calculations of transient flows. Each grid line represents a quadrilateral diagonal, and the opposite diagonal can be chosen whenever vertices move in the flow to positions which

favor that connection. Such a reconnection involves just the four vertices describing the quadrilateral. No fluid moves relative to the quadrilateral, eliminating one form of numerical dissipation. Vertices may also be added or deleted to preserve the desired resolution by local algorithms which involve only those vertices in the vicinity of the grid anomaly. Major advantages of this technique are that the algorithms can be conservative, they permit a minimum of numerical dissipation and yet they require very little computer time since most of the grid remains unaltered.

A basic technique of differencing the equations over such a grid for the case of inviscid incompressible flow is given in Appendix A. The current version of the code employs centered implicit integration to advance the physical variables in time and has been shown to be second-order accurate. Vorticity is conserved identically and the pressure is advanced to conserve the divergence about each vertex. These new pressures are then used to advance the velocities and update the grid positions.

Although much of the work thus far has centered on the finite-difference techniques and on the grid restructuring algorithms, the problems of realistic boundary conditions and initial conditions remain. Inflow and outflow boundary conditions which do not adversely affect the rest of the computational region over a spectrum of wavelengths are goals which have not yet been reached even on more standard grids. Similarly, initialization procedures for nonlinear, transient flows involving a free-surface have been investigated only minimally and on a case-by-case basis.

Since techniques for boundary conditions and initialization procedures of free-surface waves are still in an early stage of development, the present results necessarily are restricted in their range of application. The choice of periodic boundary conditions restricts the calculation domain to an integral number of wavelengths and requires that the domain is one element of an array of identical domains. For many conditions of wave flow this yields a quite realistic situation and there is no concern for numerical damping at radiative boundaries. This restriction on the problem has in fact permitted considerable progress to be made in the numerical calculation of free-surface, progressive waves, even for cases with obstacles such as bottom-seated half-cylinders in the flow. The present findings show that

when wave reflection from an obstacle is small, the periodicity of domains does not prevent good agreement between numerical results, experimental data and theoretical results. In fact, the agreement is quite good. This is an unexpected result, since the blockage due to the obstacle can be quite large and deviations from purely periodic flow would be expected.

However, if wave reflection from an obstacle is significant, the domains to the left and right of the center computational domain have a very large influence on the numerical results. For the high reflection case considered here, the periodicity of domains leads to a solution of a problem which is different from the problem of interest. This is not surprising since the problem posed numerically is quite different. Even so, some of the numerical results appear to be useable. The high reflection case does emphasize the desirability of future research to include the formulation of continuative (i.e., non-periodic) boundary conditions which would permit more realistic calculation of the wave flow over a single obstacle.

The calculation is started by a sinusoidal pressure pulse on the free surface which initiates a standing wave. At the quarter period of the standing wave ($t = T/4$ sec) a second pulse (phase shifted a quarter wave length) is applied to form the progressive wave. This initialization procedure may not be the most appropriate, especially when an obstacle is in the flow field, but it is simple, easy to apply, and exhibits good numerical stability for standing waves (Fritts and Boris, 1977a) and for progressive waves in a straight channel. Also, it allows the periodic boundary conditions to be retained and introduces minimal grid distortion and variation in the triangle areas.

RESULTS AND DISCUSSION

In the following sections we have three primary objectives. The first objective is to validate the numerical method, i.e., the computer code SPLISH, for calculating progressive free-surface waves. The second objective is to demonstrate the applicability of the numerical results. The third objective is to demonstrate the potential of the numerical approach, especially for those cases where theory is limited by approximations.

The results are presented in the following two sections. First, the numerical results are discussed and compared with results from classical wave theory. In the subsequent section the present numerical results from SPLISH are compared with experimental data obtained in the NRL wave channel. Good agreement is obtained between the numerical results and various theories and between the numerical results and the experiments when the numerical simulation appropriately models the theory or experiment.

Numerical Results and Comparison With Theory

Results from calculations for three sets of conditions are presented and a comparison is made with results obtained from wave theories. Although the numerical formulation is not limited to linear or nearly-linear waves, the calculations were performed for small amplitude waves to permit meaningful comparison with theory.

The first conditions considered are for a two-dimensional wave channel with no obstruction to the flow. For single frequency waves, the periodic boundary conditions are quite appropriate and the good agreement with the theory establishes, in part, the validity of the numerical calculations. The next conditions considered are for a half-cylinder mounted on the bottom of the channel with wavelength (λ), depth (d) and cylinder radius (a) chosen to yield minimal wave reflection from the half cylinder, according to the theory of Naftzger and Chakrabarti (1979). In the third case, the values of λ, d and a are changed so that the amount of wave reflection is significant. The numerical results for this case clearly show the need for continuative boundary conditions since the numerical simulation does not properly model the same physical situation.

Uniform Depth Channel

For this simplest of cases to consider, the computational domain is divided into triangles as shown in Figure 1. Twenty-six vertices were used in the horizontal direction and six in the vertical direction, for a total of 156 vertices. The lack of direct correspondence between vertices and triangles is discussed

in Appendix A and is illustrated here as 250 triangles form the computational domain. Once the domain is divided into triangles, the calculation is started by a sinusoidal pressure pulse on the free surface which initiates a standing wave. Then at the quarter period of the standing wave ($t = T/4$ sec) a second pulse (phase shifted a quarter wave length) is applied to initiate the progressive wave. The advantages of this initialization procedure are simplicity, lack of grid distortion, and good results which have been obtained. A disadvantage is the transients from the pressure pulses, but these transients do not seem to cause any serious problems. The transients can be reduced by an alternative initialization procedure wherein the free surface is displaced to a modified sine wave (Penny and Price, 1952) and the progressive wave then formed by a single pressure pulse at $t = 0$. With this procedure the pressure transients are reduced but some grid distortion is introduced.

The triangular grid (for depth $d = 1$ m and wavelength $\lambda = 2.5$ m) plotted for three points in time in Figure 2 illustrates a potential disadvantage of the Lagrangian approach. The grid is shown at times $t = 1.2$, 1.6 and 2.0 sec (or at time steps 31, 41 and 51) and the wave motion from left to right is clearly shown. Since this particular calculation was performed without grid reconnections, the movement of fluid particles (i.e. triangle vertices) with the progressive wave introduces some very obvious distortion into the grid. With further time increments, the grid distortion would become even more pronounced and surface vertices could be carried far to the right of vertices initially below them. Since pressure gradients are calculated over triangles, it is necessary that a subsurface vertex be connected to surface vertices near it and not to vertices which the flow has carried far to the right. As discussed in Appendix A, the reconnection algorithms reestablish the grid connections so that nearby vertices are connected. Triangles which are carried off to the right by the flow are replaced at the left by identical triangles under the periodic boundary conditions. Such grid reconnections and triangle movements eliminate most of the grid distortion. Figure 3 shows the grid at $t = 2.0$ sec for a similar calculation with grid reconnection permitted and with most grid distortion eliminated. The reconnection algorithms are crucial to the success of a Lagrangian procedure, especially when there is significant long term, net motion of some fluid particles relative to other particles. The simplification achieved with the periodic boundary conditions is also illustrated.

The calculations with SPLISH for the uniform depth case also gave good agreement with classical wave theory for the wave period and for the mean drift. Previous calculations with SPLISH (Fritts and Boris, 1977) had given wave period values for a standing wave which agreed very well with theory. In fact the period converged to the theoretical value as the grid step size was reduced. Two cases for a progressive wave (depth d = 1 m and wavelength λ =2.5 m and thus d/λ = 0.4) were considered and good agreement was obtained with the theory for both the wave period and the mean drift motion. For these values of d and λ the dispersion relation in Appendix B (Equation B6) yields a wave period T = 1.28 sec. For deep water waves the period would be T = 1.27 sec, so for this case the progressive waves are very nearly deep water waves and the deep water approximation can be used.

The path over which a surface particle moves during several wave cycles is plotted in Figure 4. The wave amplitude is H = 0.047 m, or H/λ = 0.019, so that the linear wave potential given by Equation B5 is applicable. The SPLISH-generated path of a surface particle is shown in the figure by the solid line, and the particle path predicted by integrating Equations B12 and B13 is shown by the dotted line. (Note that the horizontal scale is stretched relative to the vertical scale.) The results obtained by the two methods are generally in good agreement, but the linear theory predicts slightly greater mean drift over three cycles of the wave. The predicted drift of the surface particle is $\Delta \bar{x}_l$ = 0.09 m ($\Delta t = 3T$) from the computer code, whereas $\Delta \bar{x}_l$ = 0.105 m ($\Delta t = 3T$) from Equation B17. The average calculated wave period is T_{SPLISH} = 1.32 sec over three cycles and this is in good agreement with the wave period obtained from the dispersion relation T_{STOKES} = 1.28 sec. As in the standing wave case, T_{SPLISH} should converge to T_{STOKES} for decreasing grid size.

The Lagrangian particle paths for vertices initially at y = 0 and y = -0.2 m are plotted in Figure 5 for a wave amplitude H = 0.066 m (H/λ = 0.026) at the surface. For this series of computations the wave period is T_{SPLISH} = 1.34 sec averaged over the five cycles in the figure. The corresponding wave period from Equation B6 is T = 1.29 sec, again for d/λ = 0.4. The vertical particle displacement H at a depth of y = -0.2 m (-0.08λ) is H' = 0.042 m, which results in the ratio H'/H = 0.64. From the linear theory the particle displacement H' at the depth y is given by

$$H' = H\frac{\sinh k(y + d)}{\sinh kd}.$$

Applying this equation for $ky = -0.5$ and $kd = 2.51$ as in Figure 5 results in the ratio $H'/H = 0.60$. which is in good agreement with the SPLISH-generated particle displacements over five wave cycles at $y = -0.2$ m.

The mean drift of the fluid particles in the direction of the wave motion, computed from Equation B17, is plotted in Figure 5 and on the average agrees well both on and below the surface with the SPLISH-generated particle paths shown there. While the results at $y = -0.2$ m agree on the average over five wave periods, it should be noted that the particle drift per cycle varies from $\Delta\bar{x}_l = 0.014$ m to 0.038 m about a mean value of $\Delta\bar{x}_l = 0.026$ m in the case of the computer-generated Lagrangian particle paths for the individual cycles.

These results establish, at least in part, the validity of the numerical approach even though these particular calculations were made with one of the earlier versions of the SPLISH code. Subsequent developments in the code have improved the numerical results, especially the uniformity of the particle paths, as will be seen below. While the numerical simulation of the uniform depth channel configuration closely corresponds to a realistic physical situation, other configurations are of more practical interest. Two such configurations are discussed next.

Low Reflection Wave Flow over a Half-Cylinder

One configuration which is of some practical interest is the wave flow over a bottom seated half-cylinder, which might correspond to a half buried pipe or a storage tank on the ocean floor. This case is also relatively easy to model numerically. However, with periodic boundary conditions the numerical simulation corresponds to an array of pipes which are spaced one or more wavelengths apart. Fortunately, there are combinations of wavelength, depth, and cylinder radius for which only a very small amount of the incident wave is reflected by the half-cylinder. For example, for $\lambda = 2.5$ m, $d = 1$ m,

and the cylinder radius $a = 0.5$ m together with the assumption of linear theory, Naftzger and Chakrabarti (1979) find that the reflection coefficient $R = 0.03$. With a reflected wave in this case having only 3% of the amplitude of the incident wave (and thus less than 1% of the energy), neighboring half-cylinders should have negligible effect on the flow.

A series of calculations was made for the low reflection conditions described above. The computational grid for one such case (without grid reconnections) is shown in Figure 6. Here the presence of the half-cylinder is indicated by the upward displacement of the triangle vertices above it. In subsequent calculations the amount of grid distortion was reduced by permitting grid reconnections and by using more layers of vertices. For most wave amplitudes, the best results for this case were obtained when 9 rows of 26 vertices were used to form the triangular grid.

Figure 7 shows the free surface contour and the resultant bottom pressure P_b at one instant in the passage of a wave (from left to right) over a half-cylinder (radius $a = 0.5$ m) in a channel (depth $d = 1$ m) for a wave length $\lambda = 2.5$ m. The finite amplitude of the wave ($H = 0.045$ m, from the undisturbed free surface) causes only a very small deviation from a sinusoidal surface shape in spite of the presence of the bottom seated half-cylinder. Note that the pressure scale increases downward. Since the calculation was started from still water, the pressures at step 1 correspond to the hydrostatic pressure on the channel bottom and on the surface of the half-cylinder. At step 25 the wave gives an increased pressure on the left side of the half-cylinder and a reduced pressure on the right side. This, of course, is responsible for a net force (at this instant) from left to right. At other steps in the calculation, the pressure fluctuation accurately follows the passage of peaks and troughs of the wave as will be shown.

The full wave shape and the bottom pressure distributions are well documented in Figure 7, but the details of the pressure around the half-cylinder are not shown as well as might be the case. In Figures 8-12, the domain from $x = 0.3$ m to $x = 2.2$ m is shown for times of $t = 0$, 0.96, 1.28, 1.64 and 1.92 sec. As in Figure 7 the scale for the pressure increases downward. The scale for the bottom pressure has been selected so that at $t = 0$ the P_b curve coincides with the plot of the bottom contour. The

calculation was started at still water level (as seen in Figure 8) and the wave travels from left to right. Figures 9-12 are approximately a quarter period apart and the progress of the wave can be seen clearly.

Figures 9-12 also show a depth dependence of the pressure fluctuation. As the crest and the trough of the wave pass, the pressure fluctuation on top of the half cylinder (at a depth of 0.5 m) is approximately twice that on the channel bottom (at a depth of 1.0 m). At intermediate depths (i.e. along the sides of the cylinder) the magnitude of the pressure fluctuation is between that on the channel bottom and that on the top of the cylinder. These figures also show how the pressure field on the channel bottom and on the half cylinder correspond to the passage of the wave on the free surface. In Figures 9-12 the scale for the pressure curve was chosen, as mentioned above, so that at $t = 0$ the curve for P_b coincided with the contour of the channel bottom. This scale suppresses the apparent magnitude of the pressure fluctuation. The fluctuation in P_b can be accentuated by normalization.

In Figures 13 and 14 the fluctuation in P_b, i.e. ΔP, is normalized by its maximum value (ΔP_{REF}) which occurs at the top of the cylinder as the wave crest passes by. Figure 13 shows the pressure distribution around the half-cylinder at times $t = 1.28$ and $t = 1.92$ sec which are the instants when the wave crest and trough pass over the half-cylinder. Figure 14 shows the pressure distributions around the half-cylinder at $t = 0.96$ sec and at $t = 1.64$ sec which correspond to times when the wave crest is first to the left of the cylinder and then to the right of the cylinder. In these two figures the values of ΔP from the SPLISH numerical calculations are shown by the open symbols. The solid and dashed curves shown in these figure are the values of ΔP obtained for these conditions using the approach of Chakrabarti and Naftzger (1974) which was based on Stokes' fifth-order wave theory and the assumption that the effect of the free-surface on the reflected wave potential could be neglected. For the present low-reflection conditions (with a reflection coefficient of 3%) such an assumption is quite appropriate. For these conditions the SPLISH results are in good agreement with the fifth-order theory results.

We might note here that for this case there is properly some departure from the results that would be obtained with linear wave theory. In particular, in linear wave theory the magnitude of the

pressure fluctuation on top of the cylinder (i.e. at $\theta = 0°$) is exactly the same when the wave crest and the trough pass by. Such is not the case with higher order theories. When the wave is described by higher order theories, the crest is more sharply peaked and the trough is more shallow than for the linear theory. Consequently, the distance from the still water level to the crest is greater than the distance from the still water level to the trough, whereas in the linear theory these two distances are equal. Thus, for $\Delta P = 0$ corresponding to the still water level, the magnitude of ΔP on the cylinder for the crest's passage is greater than for the trough's passage. As may be seen in Figure 13, $\Delta P/\Delta P_{REF}$ is 1.0 for the passage of the crest but is only 0.9 for the passage of the trough. The results of SPLISH and the fifth-order theory agree well.

The wave-induced force or force components on the half-cylinder can be obtained by integrating the pressure distribution, such as those in Figures 13 and 14, around the half-cylinder. This integration has been done in this case for the SPLISH calculations and the results of this operation are shown in Figures 15 and 16. The curves for the force components are started at $t = 0.76$ sec, after the initial transients caused by the pressure pulses which form the progressive wave have died out. The first two extrema of the F_x curve in Figure 15 correspond closely to the times of Figures 9 and 11 when the crest was to the left and then to the right of the half cylinder and with the free surface at the still water line above the half-cylinder. Also, the first two extrema of the F_y curve in Figure 16 correspond closely to the times of Figure 10 and 12 when the wave crest and then the wave trough passed above the half-cylinder. Also shown in Figures 15 and 16 are the linear theory limits for the maximum values of F_x and F_y which agree well with the SPLISH results. The limit values were calculated using a wave amplitude $H = 0.038$ m in the linear theory results obtained by Naftzger and Chakrabarti (1979). The value of $H = 0.038$ m was chosen here to match the average amplitude (over the first four wave cycles) of the wave in the numerical calculation. This was necessary since the wave amplitude (and thus the pressure and the force component amplitudes) show a decrease with time. This decrease in wave amplitude (and thus wave energy) is not due to viscous effects in the governing equations, but it

is caused by an effective dissipation of energy due to the incomplete convergence of the successive-over-relaxation (SOR) method used for the solution of the Poisson equation for the pressure. The effect of this decrease in wave amplitude will also be seen below.

The time history for the pressure (in kiloPascals or kN/m^2) at a vertex on the top of the half-cylinder is shown in Figure 17. The solid curve shows the SPLISH data and the open symbols are values obtained using full fifth-order wave theory in results obtained by Chakrabarti and Naftzger (1974) for wave flow over a bottom seated half-cylinder. The pressure here represents the actual gauge pressure that might be measured. The wave amplitude was assumed to be $H = 0.038$ m for the fifth-order calculations; this had been done in calculating the linear theory limits for the force components plotted in Figures 15 and 16. Here the agreement between the numerical calculations and the fifth-order calculation is quite good. With the finite grid size employed here the period given by the numerical results is about 4% greater than that from the theoretical dispersion relation, so that the theoretical and numerical results shift slightly relative to each other with time. From fifth-order theory $T = 1.269$ sec and from linear theory $T = 1.274$, while SPLISH gives here a value of $T = 1.30$ sec based on the intervals between maxima or between minima in the pressure-time history in Figure 17.

The forces and pressures on the half-cylinder are the principal results of the numerical calculations, but at times the necessary information about the quality of the numerical solution is not given by the pressure and force data. Plots of the Lagrangian particle paths have proven to be a very useful diagnostic aid for determining the quality of the solution and for examining the physical mechanism in some wave flow situations. We noted previously in the consideration of the uniform depth channel that those calculations were made with an early version of the SPLISH code. While the wave period and wave drift were predicted accurately in that case, the Lagrangian particle paths were not as regular as desired even though the calculation was for a simple channel flow without the half-cylinder. Subsequent progress in the development of SPLISH has substantially improved the quality of the results for particle paths. Figure 18 shows the Lagrangian paths of three surface vertices, in Figure 18a the vertex initially at $x = 0$ m, in 18b the vertex at $x = 0.6$ m, and in 18c the vertex at $x = 1.2$m. The particle

paths begin at step 11 after the standing wave is fully formed and the second pressure pulse has been applied. The presence of the half-cylinder in the flow seems to affect the path of the surface particle above it only slightly. A larger effect would be seen for a larger wave amplitude or for vertices nearer to the cylinder. The particle paths in Figure 18 also exhibit a slight decrease in amplitude with time as mentioned earlier.

Even though there is some loss of energy in the numerical solution (due to incomplete convergence of the SOR method, mentioned previously), the Lagrangian particle paths clearly show that, for these low wave reflection conditions, SPLISH is generating a stable, well-behaved solution for the surface wave flow over the half-cylinder. The particle paths seem to indicate that the wave reflection from the half-cylinder is sufficiently low that it neither adversely affects the quality of the solution nor significantly changes the physical situation which is being modeled numerically. A case in which the amount of wave reflection is significant and the periodic boundary conditions appear inappropriate is considered in the next section.

High Reflection Wave Flow over a Half-Cylinder

While the numerical results for a low reflection case presented in the preceding section are promising, reasonable numerical simulations cannot be made for high wave reflection from the half-cylinder using periodic boundary conditions. The results of Naftzger and Charabarti (1979) show that quite high reflection coefficients can be obtained. Unfortunately, the higher reflection coefficients are obtained at values of $d/a \rightarrow 1.0$, i.e. nearly complete blockage of the channel. With the value of $d/a = 2.0$, as used in the low reflection case, a reflection coefficient, $R_{max} = 0.24$ can be obtained by decreasing ka ($=2\pi a/\lambda$) from 1.25 to 0.5 (corresponding to increasing λ from 2.5 m to 6.3 m). For this value of R, the reflected wave would have only 6% of the energy of the incident wave. Whereas for $d/a = 1.5$, $R_{max} = 0.4$ (at $ka = 0.5$) and the reflected wave has 16% of the energy of the incident wave. These latter values were chosen for the high reflection case. The corresponding conditions for the SPLISH calculations are $d = 1.0$ m, $a = 0.667$ m and $\lambda = 8.4$ m.

In choosing these conditions, not only the amount of an incident wave energy that is reflected by the bottom seated half-cylinder is changed, but also the deep water/shallow water characteristics of the wave flow were altered. For the low reflection case the product of the wave number and depth has the value $kd = 2.51$ which gives almost deep water waves ($kd > 3.14$). However, for the high reflection case $kd = 0.75$ and the wave flow is distinctly *not* in the deep-water regime. Some test calculations previously had been made with SPLISH for a shallow water uniform depth channel with good results, so for the present high reflection conditions the presense of the half-cylinder was the critical element in the numerical simulation.

Figures 19-22 show plots of the surface contour, the bottom contour and the bottom pressure between $x = 3.2$ m and $x = 5.2$ m with the half-cylinder centered at $x = 4.2$m. The automatic grid restructuring algorithms in SPLISH modified the initial grid slightly after the first time step in that several triangles were added near the intersection of the half-cylinder and the channel bottom. Thus P_b for $t = 0.22$ sec instead of for $t = 0.0$ sec is plotted in Figure 19, closely approximating the initial still water conditions. As in Figures 8-12 the pressure scale in kiloPascals increases with depth and was chosen so that P_b at $t = 0$ would correspond to the bottom contour. Figure 20, for $t = 1.88$ sec, represents that time in the simulation when the water depth above the half-cylinder was at the still water level and a wave crest was to the left of the half-cylinder. Figure 21 is for $t = 2.68$ sec and for the wave crest directly above the half-cylinder, and Figure 22 is for $t = 3.28$ sec with the wave crest to the right of the half-cylinder. As before, the direction of wave travel is from left to right. These figures show much the same information as did Figures 8-12, but with the half-cylinder larger and less of the surface wave visible in the figures because of the longer wavelength. The curves for the pressure around the half-cylinder (in these figures) do not show any detrimental effect of the wave reflection and in fact appear to be quite reasonable representations of the physical situation.

The time history of the pressure at a point on top of the half-cylinder ($\theta = 0°$) shown in Figure 23 also does not clearly indicate any detrimental effect from the reflection of the incident wave from the obstacle. Again there is a decrease in the amplitude of the numerically generated pressure curve much like that seen in Figure 17.

Somewhat clearer evidence of the wave reflection is seen in Figures 24 and 25. Figure 24 shows $\Delta P/\Delta P_{REF}$ around the half-cylinder at $t = 2.68$ sec and $t = 4.14$ sec, corresponding to a crest and a trough above the half-cylinder. Figure 25 shows $\Delta P/\Delta P_{REF}$ at $t = 1.88$ and 3.28 sec corresponding to a wave crest first to the left of the half-cylinder and then to the right. For all four sets of data the value of ΔP_{REF} was the same — the value of ΔP at $t = 2.68$ sec and at $\theta = 0°$. Also shown in these figures are curves for the fifth-order theory (Reference 3) results and curves for the linear theory (Reference 9) results. Some significant differences are noted between the linear and fifth order theory results, especially on the sides of the half-cylinder. For the times when the crest or the trough is above the half-cylinder, the fifth order theory results are symmetric with respect to $\theta = 0°$. That is, the pressure fluctuation distribution on the upstream (left) side of the half-cylinder is the same as that on the downstream (right) side. In contrast, for the linear theory results there is a pronounced bulge in the distribution curve on the upstream side of the half-cylinder for both crest and trough passage. Thus, while the fifth-order theory results would predict no side force on the half-cylinder at either crest or trough passage, the linear theory results would show a rather large force to the right at crest passage and a comparable force to the left at the time that the trough passes over the half-cylinder.

Another difference in the results of the linear and fifth-order theories is seen in the magnitudes of the pressure fluctuation distributions at the time of the trough passage. The linear theory distribution curve has the same magnitude as the curve for the wave crest passage, whereas, for the trough passage over the half-cylinder, the fifth-order theory results show a reduction in magnitude of the pressure fluctuation distribution curve. For crest passage, the linear theory results seem to more properly show the pressure distribution, whereas, for the trough passage, each theory seems to model one aspect of the distribution curve. The linear theory properly shows the effect of wave scattering from the half-cylinder, and the fifth-order theory properly shows the nonlinear effect of finite-amplitude waves.

For the pressure fluctuation distributions shown in Figure 25 there is only a slight difference between the linear and fifth-order theory results. Both the vertical and horizontal forces acting on the half-cylinder would be slightly greater if calculated from the linear theory instead of from the fifth-order

theory. This difference between the results of the two theoretical approaches is quite small compared to the differences at the time of crest and trough passage as shown in Figure 24.

For this case, the agreement is much poorer between the theoretical results and the SPLISH results. For the crest over the half-cylinder (at $t = 2.68$ sec), the SPLISH results agree quite well with the fifth-order results, but the linear theory results are the more realistic because the boundary condition on the reflected wave is satisfied in the latter case. For the trough passage over the half-cylinder (at $t = 4.14$ sec) the SPLISH results seem to show both an effect of wave reflection and an effect of finite-amplitude waves. However, a corresponding effect of wave reflection should have been evident in the distribution for the crest passage (at $t = 2.68$ sec) but was not. Thus what appears to be an effect of wave reflection could instead be due to the changing nature of the wave flow which is considered later in the discussion of the particle paths for this case.

The SPLISH results for $t = 1.88$ and 3.28 sec shown in Figure 25 have two interesting features; one seems to show an effect of wave reflection, the other almost certainly is due to the effect of wave reflections from neighboring half-cylinders in the numerical simulation. The SPLISH results for the wave to the left of the half-cylinder ($t = 1.88$ sec) agree well with the theoretical results except on the downstream (right) side for $\theta > 30°$. This might be an effect of wave scattering which the theoretical results do not show, but such is not certain. The difference in the theoretical and SPLISH values of $\Delta P/\Delta P_{REF}$ for $\theta > 30°$ does have the effect of decreasing the horizontal force on the half-cylinder. This effect is also seen in Figure 26. For the wave to the right of the half-cylinder ($t = 3.28$ sec) the SPLISH results agree poorly with the theoretical values. For this time in the wave cycle, the pressure distribution around the half-cylinder from the SPISH results gives a value for the horizontal force which is much too small as is discussed further later. This poor agreement between the numerical and theoretical results seems to be caused by the use of the periodic boundary conditions in the SPLISH code with the resulting, non-physical, wave reflections from the neighboring half-cylinders which exist only in the numerical simulation. The interaction between the periodic boundary conditions and the wave reflections is discussed further in the consideration of the Lagrangian particle paths.

Time-history plots of the numerically-calculated force components on the half-cylinder are shown in Figures 26 and 27. Again, as in Figures 15 and 16, the plotting of the curves is begun after the initial transients die out. Linear wave calculations from Naftzger and Chakrabarti's predictions (1979) are shown. As for the previous low reflection case, the vertical force component curve shown in Figure 27 appears quite similar to the pressure curve for the location on top of the half-cylinder shown in Figure 23. The local extrema of the two curves show quite similar characteristics. Indeed, both the force and the pressure-time variations seem most nearly like slightly modified sine or cosine curves.

Such is not the case, however, for the horizontal force component F_x as shown in Figure 26. There is part of a sine curve from $t = 1$ to 2 sec, then something like a saw-tooth curve from $t = 2$ to 5 sec, followed by a full cycle of a sine wave and then another saw-tooth. Consideration was given to the possibility that this behavior was due to the difficulty in accurately calculating the horizontal force component along the steep vertical sides of the half-cylinder. However, this behavior of the F_x curve did not appear in Figure 16 for the low reflection case, and so the manner of calculating F_x did not appear to be the cause of the irregularities in the horizontal force component. Considering Figures 25 and 26 together shows that at $t = 1.88$ seconds the pressure distribution from the numerical simulation agreed well with the theoretical distribution and that the horizontal force component still is quite regular. However, at $t = 3.28$ sec, the numerical and theoretical pressure distributions agree poorly. Closer examination of the two curves in Figure 25 shows that they give similar values for F_y but very different values for F_x. Indeed, as may be seen in Figure 26, the magnitude of F_x at $t = 3.28$ sec is much lower than would be obtained if F_x followed the expected sine curve. This behavior of the horizontal force — time history can be attributed to the interaction between the reflected waves and the periodic boundary conditions. Further effects of this interaction are seen in the Lagrangian particle paths which are considered next.

In Figures 28-31 the Lagrangian particle paths are shown for surface vertices initially at $x \simeq 0.0$ m, 2.0 m, 4.2 m and 6.4 m. The initial positions of the particles on the still water level are indicated by a circled x. The anomalies in the Lagrangian particle paths are the most striking features of these

figures. In addition to specific comments about the individual figures, several general observations can be made. Since for these conditions the progressive waves can be characterized as approaching shallow water waves, the particle paths should be more elliptic in nature than circular. This is the case in Figures 29 and 31 for the vertices at $x \simeq$ 2.0 m and 6.4 m. However, in Figures 28 and 30 the particle paths for the vertices at x = 0.0 m and 4.2 m are much more circular in nature, at least initially. The overall effect is that at x = 0.0 m and 4.2 m the wave amplitude is approximately twice what it is at x = 2.0 and 6.4 m.

In all four figures it appears that the open orbits of the particle paths are collapsing to flattened, inclined, paths along the streamlines characteristic of a standing wave pattern. It is here that the interactions of the wave reflections and periodic boundary conditions are most evident. In the numerical simulation the bottom seated half-cylinder seen in the figures represents one member of an array of half-cylinders, uniformly spaced one wavelength apart. The periodic boundary conditions require that conditions at x = 0 m and at x = 8.4 m be the same, so that the computational domain is one of a set of identical domains. Because of the high reflection coefficients in this physical situation, the reflected waves from one barrier should interfere with the transmitted waves from the preceding barrier. If a progressive wave is viewed as a superposition of standing waves, interference would be expected among the standing wave components of the reflected and transmitted waves. Thus, with repeated reflections of waves between adjacent half-cylinders, the initial progressive wave seems to transform into standing waves. Also, the manner in which the progressive wave is initiated does not represent an incoming wave field, but rather a wave field suddenly springing up (under, of course, the influence of the applied pressure pulses).

We note that at x = 4.2 m the surface vertex is a full wave length away from the neighboring half-cylinders (excepting the one directly under it), and it should move independently of the effects of reflected waves for a full wave cycle or more. This does indeed seem to be the case, as shown in Figure 30. In a similar manner, the particle at x = 0 m should be free of the effect of wave reflection for three quarters of a wave cycle as the trough formed at x = 2.1 m reaches the half-cylinder at $T/4$ sec

and the first reflection reaches $x = 0$ in a time of $T/2$ sec or at $t = 3T/4$ sec. As shown in Figure 28, this seems to be the case. The particle at $x = 2.1$ m should be first influenced by the wave reflection at $T/2$ sec as the trough takes $T/4$ sec to reach the half-cylinder and the reflection takes $T/4$ sec to return. The particle path in Figure 29 suggests this sort of behavior.

The Lagrangian particle path for the vertex initially at $x = 6.4$ m should show about one wave cycle of motion before being affected by any wave reflection. The trough initially formed at $x = 10.5$ m (i.e., 8.4 m + $\lambda/4$) should reach the half-cylinder to the right in $T/4$ sec and the reflection back should reach $x = 6.4$ m in an additional $3T/4$ sec. However, there is some effect on the particle path at $T/2$ sec, as observed in the bent shape of the ellipse, and then nearly a full wave cycle passes before the particle path appears to collapse to that of a standing wave. The first irregularity could be due to the half-cylinder having some unrecognized effect on the passage of the first wave trough over it.

Most of the characteristics of the Lagrangian particle paths in Figures 28-31 seem to be due to the reflections of waves from adjacent half-cylinders. However, one characteristic remains unexplained. The wave heights at $x = \lambda/4$ and $3\lambda/4$ are only half of the wave heights at $x = 0$ and $\lambda/2$. Wave reinforcement and cancellation does not provide a fully satisfactory explanation. The points at $x = 0$ and $\lambda/2$ are points where the reflected wave should reinforce the incident wave. Likewise, the points at $x = \lambda/4$ and $3\lambda/4$ are points where the reflected waves should partially cancel the incident waves. As the initial wave is formed by the first pressure pulse, the nodes are at $x = 0$ m and 4.2 m (i.e., at 0 and $\lambda/2$), the trough is at $x = 2.1$ m ($\lambda/4$), and the crest is at $x = 6.3$ m ($3\lambda/4$). However, at least half of a wave cycle (if not full wave cycle) should pass before any such wave reinforcement or cancellation occurs. The particle paths in Figures 28 and 30 show that the wave reaches full amplitude at $T/4$ sec (measured from the second pressure pulse which forms the progressive wave) with no assistance of reinforcement from a reflected wave. The particle paths in Figures 28-31 almost seem to indicate that the primary wave flow is modulated by a secondary standing wave. Unless the half-cylinder poses more blockage to the progressive wave flow than had been assumed, it is not clear what the source of such a standing wave component might be.

While the development of a standing wave is perhaps most obvious in Figures 28-31, as discussed above, other figures also suggest such an occurrence. For example, the pressure-time history for the top of the half-cylinder (shown in Figure 23) is really quite remarkably regular and in good agreement with fifth-order wave theory considering the irregularities in the flow field. Yet this pressure-time history would be quite consistent with a standing wave flow field with crests and troughs nearly above the half-cylinder. The vertical force time history shown in Figure 27 is also remarkably regular but is also consistent with the existence of a standing wave. The irregularities in the horizontal force shown in Figure 26 could be explained in part by a standing wave. That is, with crests and troughs of a standing wave centered above the half-cylinder, there would be little, if any, horizontal force on the half-cylinder. Indeed, the horizontal force calculated in the numerical simulation is much less than predicted by the linear wave scattering theory of Naftzger and Chakrabarti (1979).

Also, pressure distributions around the half-cylinder, such as those shown in Figures 24 and 25, for later times in the SPLISH calculation show a further effect of a developing standing wave. Specifically, for times corresponding to crests and troughs, the distribution of $\Delta P/\Delta P_{REF}$ are much like those shown in Figure 24. However, the distribution for intermediate times (as in Figure 25) show an increasingly large difference between the SPLISH results and the results from wave theory. In particular, the SPLISH results approach $\Delta P/\Delta P_{REF} = 0$ even more strongly than was the case for $t = 3.28$ sec. Thus, at times when the wave theories would give maximum side forces on the half-cylinder, the SPLISH results show only very small side forces. Such behavior is fully consistent with a standing wave pattern with crests and troughs approximately above the half-cylinder. While we see considerable evidence for a standing wave pattern in the numerical results, most of the evidence points to the gradual development of the standing wave after repeated wave reflections. It remains unexplained why in the SPLISH results the wave height at $x = 0$ m and at $x = 4.2$ m is nearly twice the wave height at $x = 2.0$ m and $x = 6.4$ m.

The results for the low reflection case indicate that, even with the periodic boundary conditions, SPLISH can be used with reasonable confidence for calculating the flow of waves over obstacles (thus

wave-structure interactions) if wave reflections are not significant. However, for cases with significant wave reflection in the flow, alternate (non-periodic) boundary conditions are clearly needed, since under the periodic boundary conditions a different physical situation is modeled with a correspondingly different flow as a result. Further alternate techniques for initiating the progressive wave seem to be needed. It would also be very desirable to achieve large reductions in computing costs and time. Each of the SPLISH calculations for the two sets of conditions presented here required about 20 minutes of computing time on the Texas Instruments (TI) Advanced Scientific Computer (ASC) at NRL at a cost of approximately $400. These times and costs were incurred even though the code had been especially developed to take maximum advantage of the vector characteristics of the ASC. Thus, significant reductions in computing costs and times may be difficult to achieve. Additionally, the large memory requirements of the code would make it difficult to implement SPLISH on other computers.

In the above discussion we have only compared the results obtained with SPLISH with results from classical linear and fifth-order wave theories. Even though most of these comparisons showed good to very good agreement, it is also appropriate to compare all of the calculations with experimental data. This is done in the next section.

Comparisons With Experimental Data

Several wave flow experiments were performed in the NRL wave channel with a bottom-seated half-cylinder so that actual pressure measurements could be compared both to the numerical results and to the models developed by Chakrabarti and Naftzger (1974, 1979). A 1.07 m (3-1/2 ft) diameter cylinder, which spanned the entire width of the channel, was placed about one-half of the channel's length from the mechanical wavemaker. At the other end of the wave channel a sloping, porous beach with a rubberized horsehair blanket served to absorb nearly all of the incident wave energy. A more detailed description of the facility is available (see reference C1 of Appendix C). Nineteen equally-spaced ($\Delta\theta = 10°$) pressure taps were located around the circumference of the bottom-seated half-cylinder at its midsection. The individual taps were connected to a differential pressure transducer by a

rotary pressure switch. The wave height along the channel was obtained from several traversing capacitance-type wave gauges. Calibrations were performed on all sensors before and after each test series to insure that the overall accuracy of the measurement system remained well within ± 5 percent. The pressure and waveheight signals were digitized and processed by means of a Hewlett-Packard 5420A Digital Signal Analyzer. The experimental systems and methods are discussed further in Appendix C.

The cylinder reflection coefficient R, defined as the ratio of reflected to incident wave amplitudes, was obtained for a range of wavelengths and water depths. The results of these measurements, after a rudimentary adjustment for the unwanted effects discussed in Appendix C, are plotted in Figure 32 versus the wavenumber $ka = 2\pi a/\lambda$ and for several values of the relative water depth d/a. Also shown in the figure (as solid lines) are theoretical values based on linear theory with wave scattering which were taken from the paper by Naftzger and Chakrabarti (1979) and are in general agreement with the observed cylinder reflections. It should be noted, however, that some care was taken to avoid finite amplitude effects through the use of small wave steepness ratios ($H/\lambda \lesssim 0.05$). The wave steepness values during the $d/a = 1.25$ tests were reduced further, typically less than 0.02, in order to avoid second harmonic wave generation at the cylinder. This nonlinear effect seemed to be associated with the finite waveheight being a significant fraction of the finite water depth at the top of the cylinder. The second harmonic wave could be seen as the formation of a secondary crest when a trough was over the cylinder. A rule of thumb emerged from this observation and from several wave gauge spectral records (FFT) wherein second harmonic amplification did not occur for waveheights less than about 1/7 to 1/10 of the water depth over the cylinder. This criterion for the validity of the analytical method is considerably more stringent than the one originally proposed by Naftzger and Chakrabarti. The onset and form of this nonlinearity will be the subject of further investigation in the near future.

From the range of water depths and wavelengths shown in Figure 32, two cases were selected for detailed pressure studies and for comparisons with the theoretical and numerical results. The first is a relatively low reflection case ($d/a = 2.0$ and $ka = 1.25$), so that $R \lesssim 0.05$. This represents a situation

where good agreement between the three sets of results was expected. The second case is a relatively high reflection condition ($d/a = 1.5$, $ka = 0.5$, $R \approx 0.4$) which was selected as a significant test for SPLISH with regard to the use of periodic boundary conditions in the code.

Low Reflection Case

A comparison between the linear asymptotic theory and the experimental results is given in Figure 33. The asymptotic form was selected for comparison here because of its simplicity. The amplitudes and the relative phases of the pressure fluctuations are plotted against azimuthal position around the cylinder as measured in degrees from the top of the cylinder. All pressures are nondimensionalized by the maximum pressure amplitude predicted by the theory. This maximum occurs at the top of the cylinder in this case ($\theta = 0°$). The phase angles are also plotted relative to the linear theory value at $\theta = 0°$. The two sets of experimental data correspond to two wave steepnesses and indicate the absence of finite amplitude effects in this range. Except for the data at the largest azimuthal angles, the agreement between the various results is reasonably good and supports the use of the linear asymptotic theory. The differences which exist at the azimuthal extremes are possibly a residual of the reflection adjustment and/or a consequence of a small gap which existed between the bottom of the cylinder and the wave tank floor.

Since the numerical results are Lagrangian whereas the theoretical and experimental results are Eulerian, the simplest format for comparing all three is the pressure distribution around the cylinder at selected times in the wave cycle. Figures 34 and 35 presents several such comparisons for the experimental conditions cited above. Again the three sets of results compare well except near the bottom of the cylinder. Although the discrepancy appears to be small in such a plot the effect on a measured horizontal component of the wave force can be significant.

High Reflection Case

Similar results and comparisons for a relatively high reflection case ($d/a = 1.5$, $ka = 0.5$, $R \approx 0.4$) are shown in Figures 36 through 38. As before, the pressures are normalized by the magnitude at the top of the cylinder. In this case, however, the maximum pressure fluctuation occurs on the

upstream side of the cylinder where both the incident and reflected waves are present. The experimental pressures and phases shown in the figures were obtained from the data after a correction for the additional standing waves in the laboratory channel (see Appendix C). This correction, often large, neglected secondary reflections and was based on linear wave theory which may be responsible for all or part of the discrepancies between results. The theoretical results shown for the method of Naftzger and Chakrabarti were kindly provided by them (R.A. Naftzger, private communication, 1980).

In spite of the difficulties implied above and discussed in Appendix C, the agreement between the linear theory and the experiments is fair. The previously mentioned restriction on wave amplitude ought to be reiterated. The comparisons with the SPLISH results show the detrimental effect of surprisingly good agreement considering the use of periodic boundary conditions in the code.

SUMMARY AND CONCLUSIONS

A finite-difference numerical method for solving the governing equations of motion for inviscid, irrotational flow with a free surface using a Lagrangian triangular grid has been used and shown to yield reasonable results. Calculations for progressive surface wave flows have given results for the wave period, the drift velocity and the surface particle movements with are in good agreement with results obtained from classical wave theory.

Calculations for the passage of waves over a submerged obstacle are encouraging and show some promise of providing practical results for more complex flows such as breaking-wave forces. These calculations demonstrate the adaptability which the triangular grid provides. The advantages of the Lagrangian formulation are shown in that the grid conforms to the fluid area and that no interpolation is needed to locate the free surface or the surface of the submerged obstacle.

Two cases of flow over a submerged, half-cylindrical obstacle have been considered. The results for the low wave reflection case indicate that, even with the periodic boundary conditions, SPLISH can be employed with reasonable confidence to calculate the flow of waves over obstacles (thus wave-structure interactions). However, for cases with significant wave reflection in the flow, continuative or

radiative boundary conditions are clearly desirable, if not necessary, since the periodic boundary conditions lead to the simulation of a flow quite different from that desired. Also, alternative techniques for initiating the traveling surface wave seem to be required.

While additional work on non-periodic boundary conditions, initial conditions and gridding of the flow field is clearly necessary, the present numerical method is a promising computational tool for predicting the velocities and pressure fields produced by nonlinear, finite-amplitude regular wave motions. It is hoped that future developments will extend the capabilities of codes such as SPLISH to transient phenomena such as wave breaking and wave slamming and that significant reductions in computing times and costs can be achieved. Reduction in the memory requirements would also be desirable.

ACKNOWLEDGMENTS

This report has been prepared as part of the research program of the Naval Research Laboratory. The authors wish to thank S.K. Chakrabarti and R.A. Naftzger of the Chicago Bridge and Iron Company for providing detailed computational results for several of the test cases discussed in this report.

REFERENCES

1. Bai, K. J. and R. W. Yeung (1974). "Numerical Solutions to Free-Surface Flow Problems," *Proceedings of the Tenth Symposium on Naval Hydrodynamics,* MIT, Cambridge, Mass., 609-647.

2. Boris, J. P., K. L. Hain, and M. J. Fritts (1975), "Free Surface Hydrodynamics Using a Lagrangian Triangular Grid," *Proceedings of the First Int'l Conference on Numerical Ship Hydrodynamics,* NBS, Gaithersburg, MD., pp. 683-716.

3. Chakrabarti, S. K. and R. A. Naftzger (1974), "Nonlinear Wave Forces on Half Cylinder and Hemisphere," *Proceedings of the ASCE, Journal of the Waterways, Harbors and Coastal Engineering Division,* Vol. 100, 189-204.

4. Dean, W. R. (1948), "On the Reflection of Surface Waves by a Large Cylinder," *Proceedings of the Cambridge Philosophical Society, Vol. 44, 483-491.*

5. Fritts, M. J. and J. P. Boris (1977a), "Solution of Transient Problems in Free-Surface Hydrodynamics," NRL Memorandum Report 3446.

6. Fritts, M. J. and J. P. Boris (1977b), "Transient Free Surface Hydrodynamics," *Proceedings of the Second International Conference on Numerical Ship Hydrodynamics,* Berkeley, CA., pp. 319-328.

7. Fritts, M. J., E. W. Miner and O. M. Griffin (1980), "Numerical Calculation of Wave-Structure Interactions," *Computer Methods in Fluids,* Pentech Press; London, pp. 1-25.

8. Miner, E. W., M. J. Fritts and O. M. Griffin (1978), "A finite-difference method for calculating free surface waves," *Proceedings of the First Int'l Conference on Numerical Methods in Laminar and Turbulence Flow,* Swansea, U. K., pp. 597-608.

9. Naftzger, R. A. and S. K. Chakrabarti (1979), "Scattering of Waves by Two-Dimensional Obstacles," *Journal of Ship Research,* Vol. 23, 32-42.

10. Nichols, B. D. and C. W. Hirt (1977), "Nonlinear Hydrodynamic Forces on Floating Bodies," *Proceedings of the Second Int'l Conference on Numerical Ship Hydrodynamics,* Berkeley, CA. pp. 382-394.

11. Ogilvie, T. F. (1963), "First and second order forces on a cylinder submerged under a free surface," *Journal of Fluid Mechanics,* Vol. 29. 451-472.

12. Shanks, S. P. and J. F. Thompson (1977), "Numerical Solutions of the Navier-Stokes Equations for 2D Hydrofoils in or below a Free Surface," *Proceedings of the Second Int'l Conference on Numerical Ship Hydrodynamics,* Berkeley, CA., pp. 202-220.

13. Ursell, F. (1950), "Surface waves on deep water in the presence of a submerged cylinder," *Proceedings of the Cambridge Philosophical Society,* Vol. 46, 141-152.

14. Ursell, F., R. G. Dean and Y. S. Yu (1959), "Forced small-amplitude water waves: a comparison of theory and experiment," *Journal of Fluid Mechanics,* Vol. 7, 33-52.

15. Wellford, L. C., Jr. (1978), "Calculation of Free Surface Hydrodynamics Problems Using a Finite Element Method with a Hybrid Lagrange Line," *Proceedings of the First Int'l Conference on Numerical Methods in Laminar and Turbulent Flow,* Swansea, U. K., pp. 995-1006.

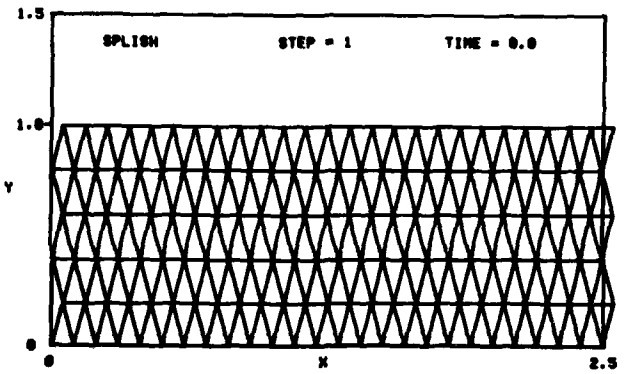

Figure 1 — An initial triangular mesh
for the SPLISH computer code.

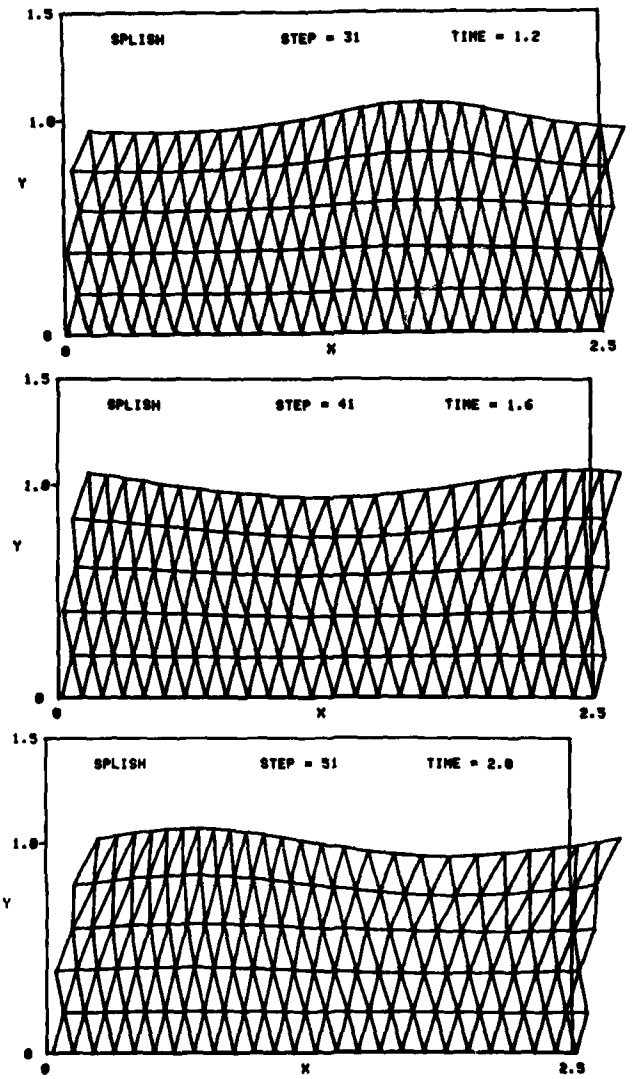

Figure 2 — An example of a SPLISH-generated
progressive wave.

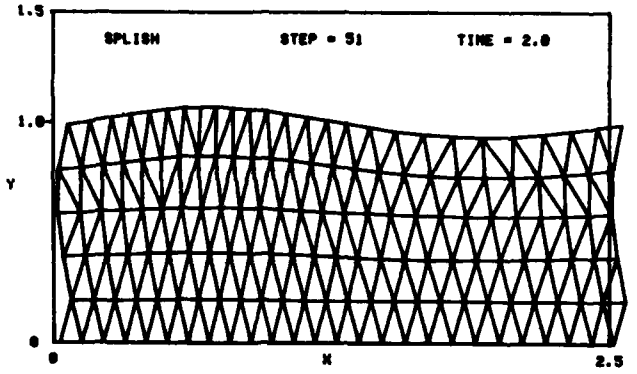

Figure 3 — An example of a SPLISH-generated computational grid with triangle reconnections.

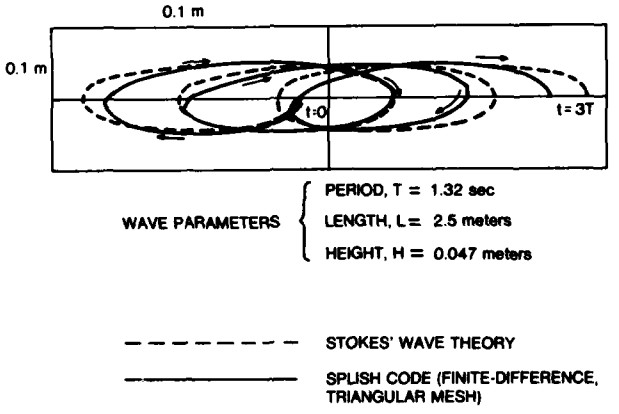

Figure 4 — A comparison between Stokes' second-order wave theory and SPLISH-generated particle paths for wavelength $\lambda = 2.5$ m and depth $d = 1$ m.

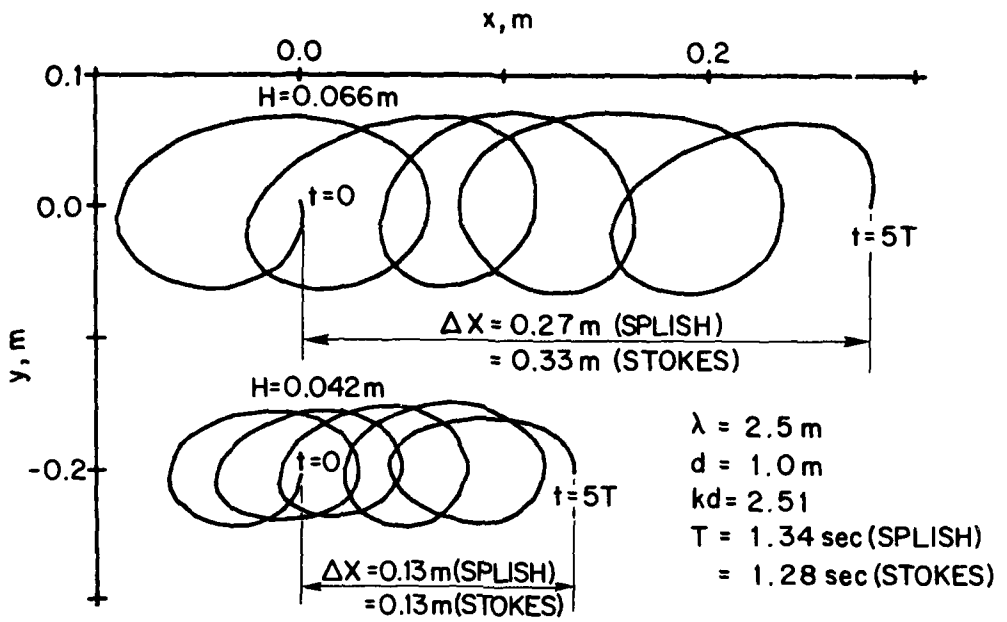

Figure 5 — Examples of SPLISH-generated particle paths for wavelength $\lambda = 2.5$ m and depth $d = 1$ m.

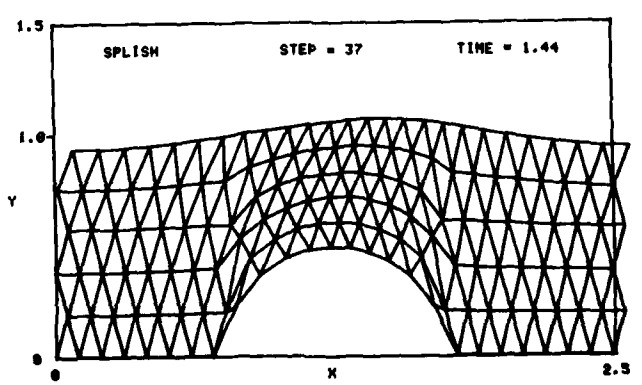

Figure 6 — An example of a SPLISH-generated triangular grid for computing the wave flow over a bottom seated half-cylinder.

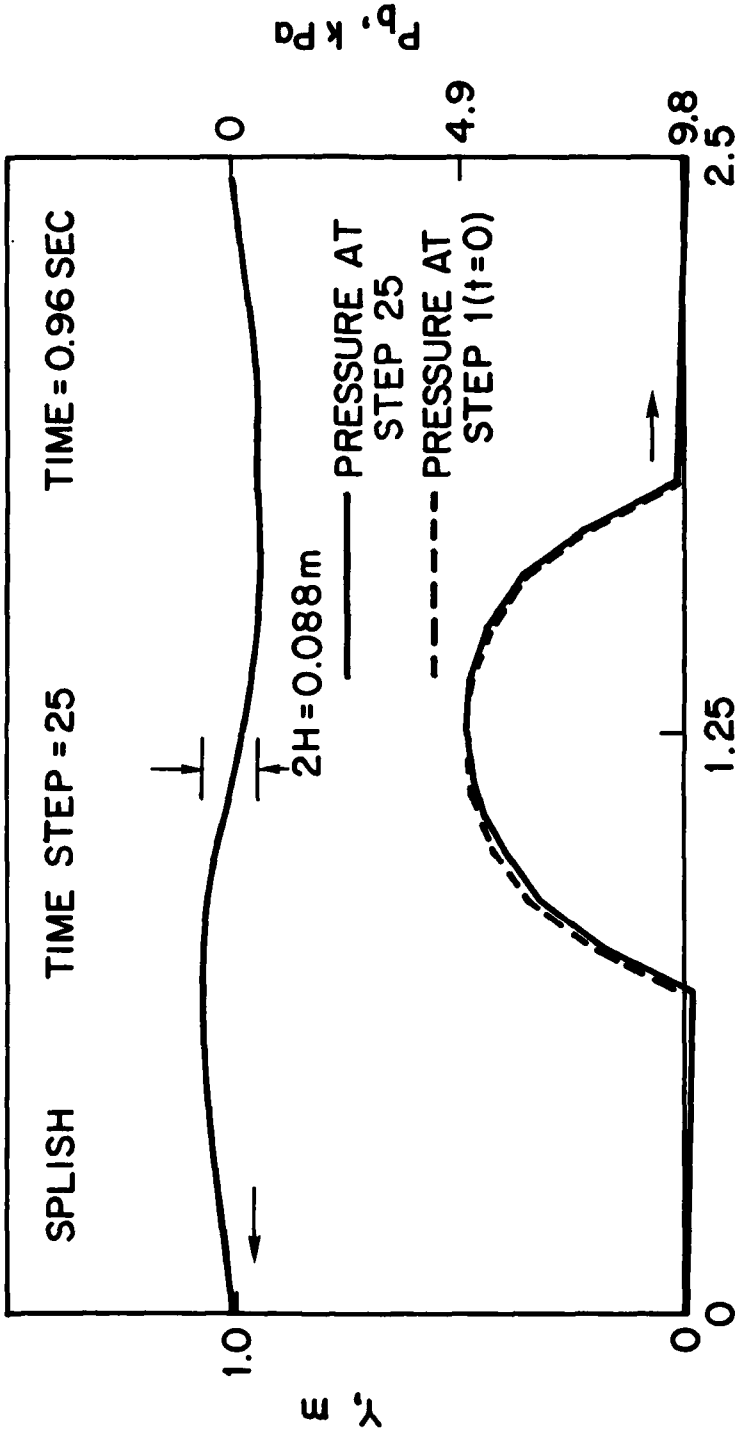

Figure 7 – The surface contour and the bottom pressure from a numerical calculation of the wave flow over a bottom seated half-cylinder.

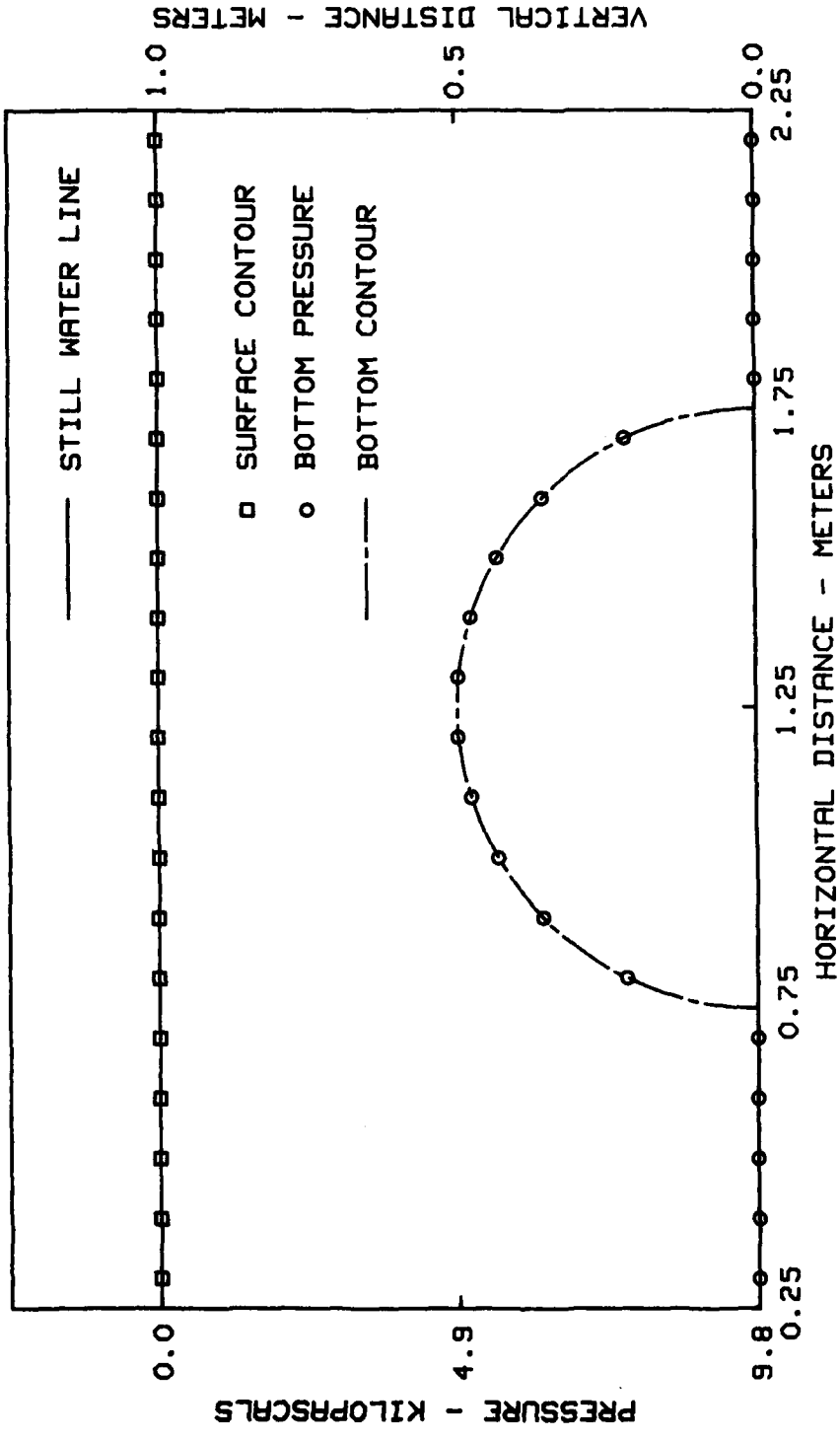

Figure 8 — The surface contour and the bottom pressure from a numerical calculation of the wave flow over a bottom seated half-cylinder at $t = 0$ sec (time step = 1, wavelength $\lambda = 2.5$ m, depth $d = 1$ m, radius $a = 0.5$ m).

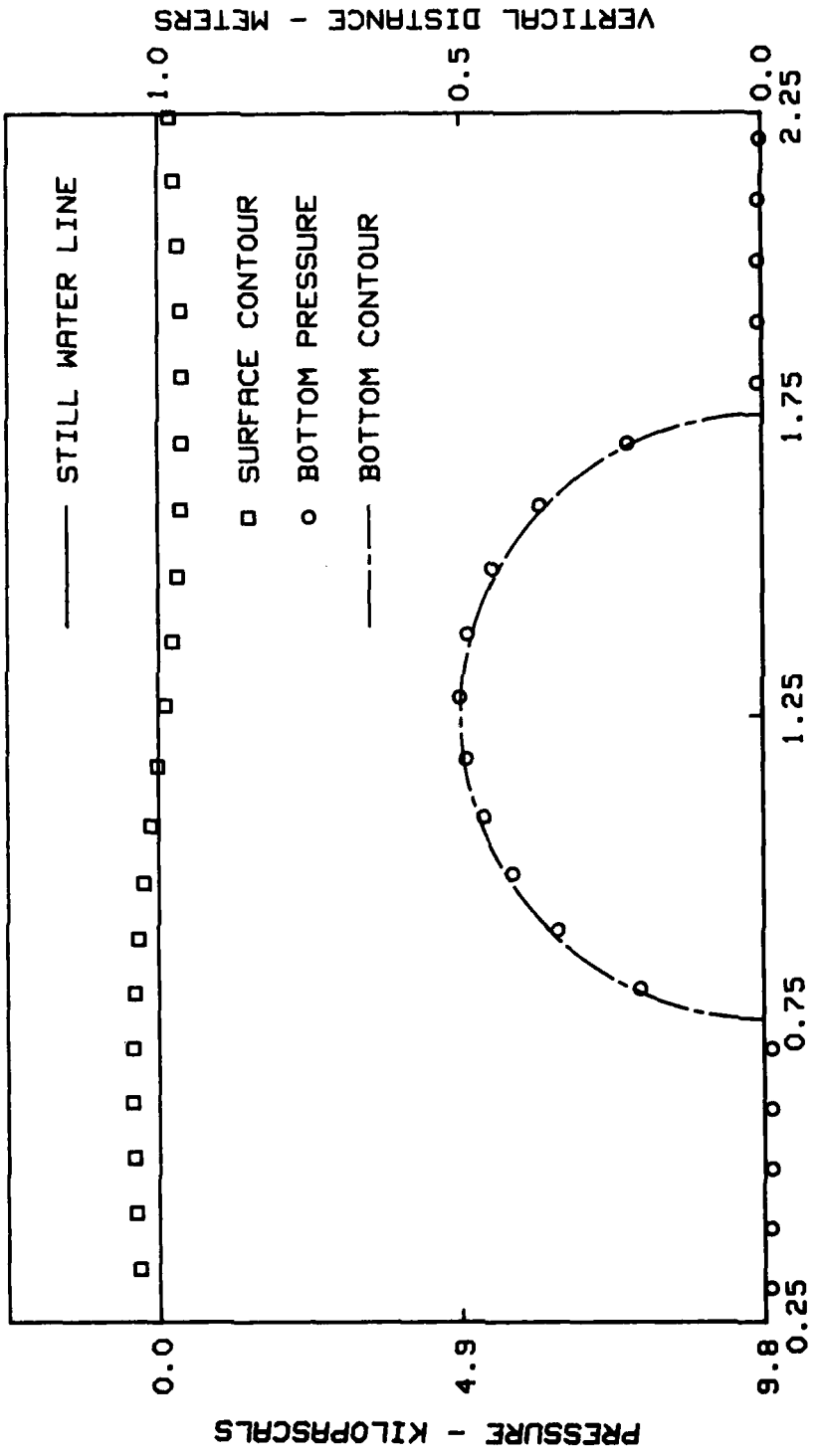

Figure 9 — The surface contour and the bottom pressure from a numerical calculation of the wave flow over a bottom seated half-cylinder at $t = 0.96$ sec (time step = 25, wavelength $\lambda = 2.5$ m, depth $d = 1$ m, radius $a = 0.5$ m).

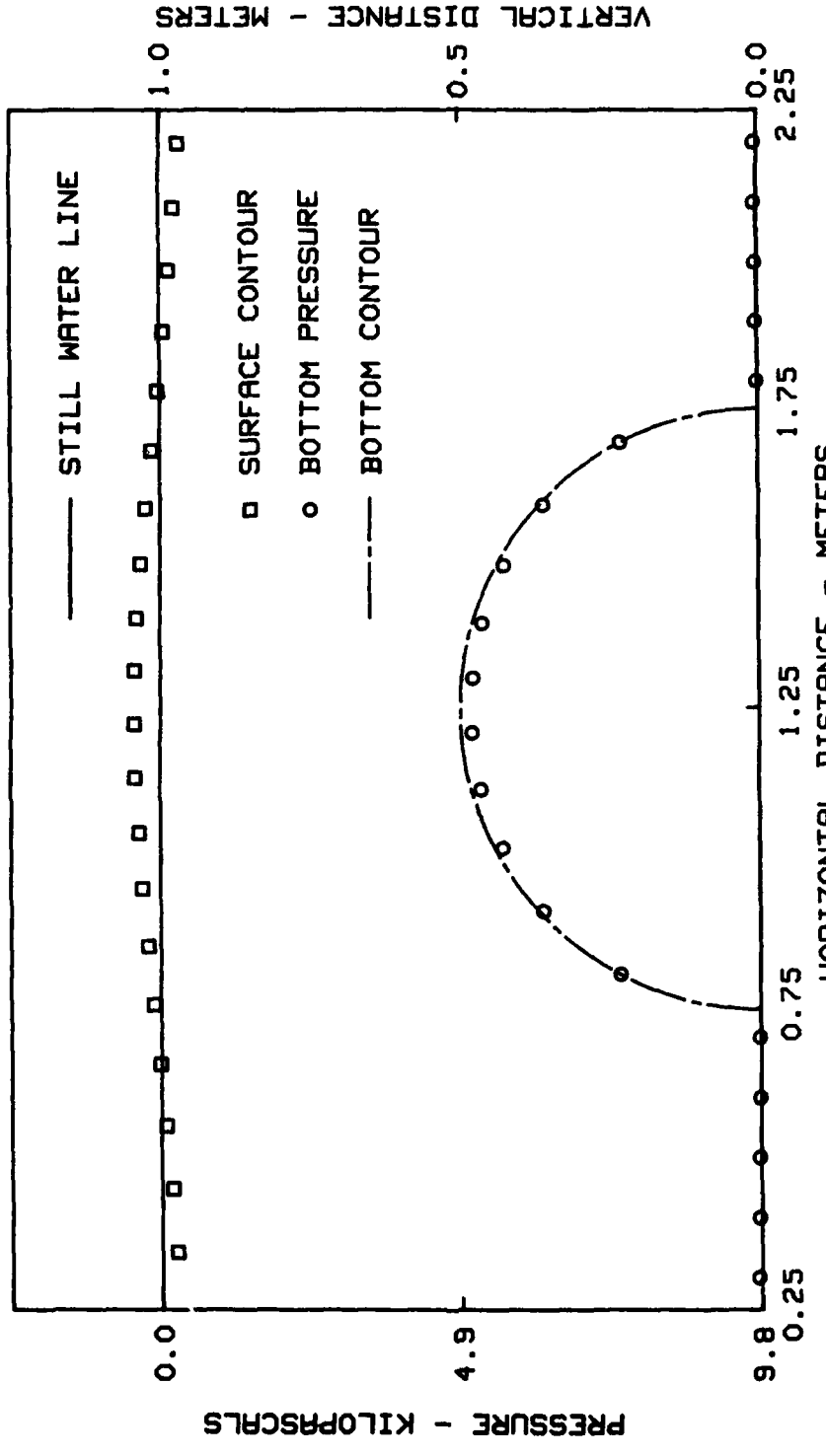

Figure 10 — The surface contour and the bottom pressure from a numerical calculation of the wave flow over a bottom seated half-cylinder at $t = 1.28$ sec (time step = 33, wavelength $\lambda = 2.5$ m, depth $d = 1$ m, radius a 0.5 m).

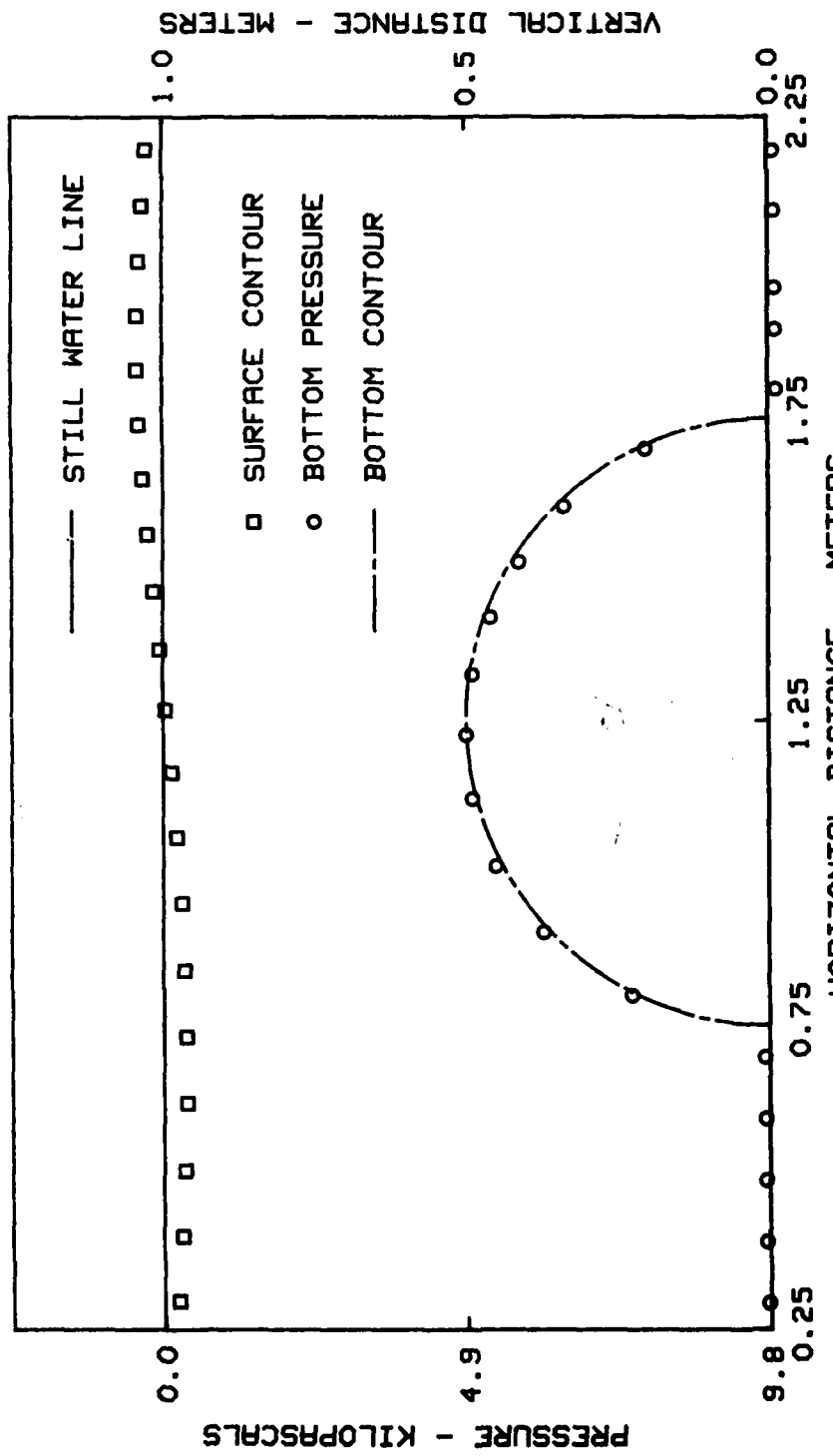

Figure 11 — The surface contour and the bottom pressure from a numerical calculation of the wave flow over a bottom seated half-cylinder at $t = 1.64$ sec (time step = 43, wavelength $\lambda = 2.5$ m, depth d m, radius a 0.5 m).

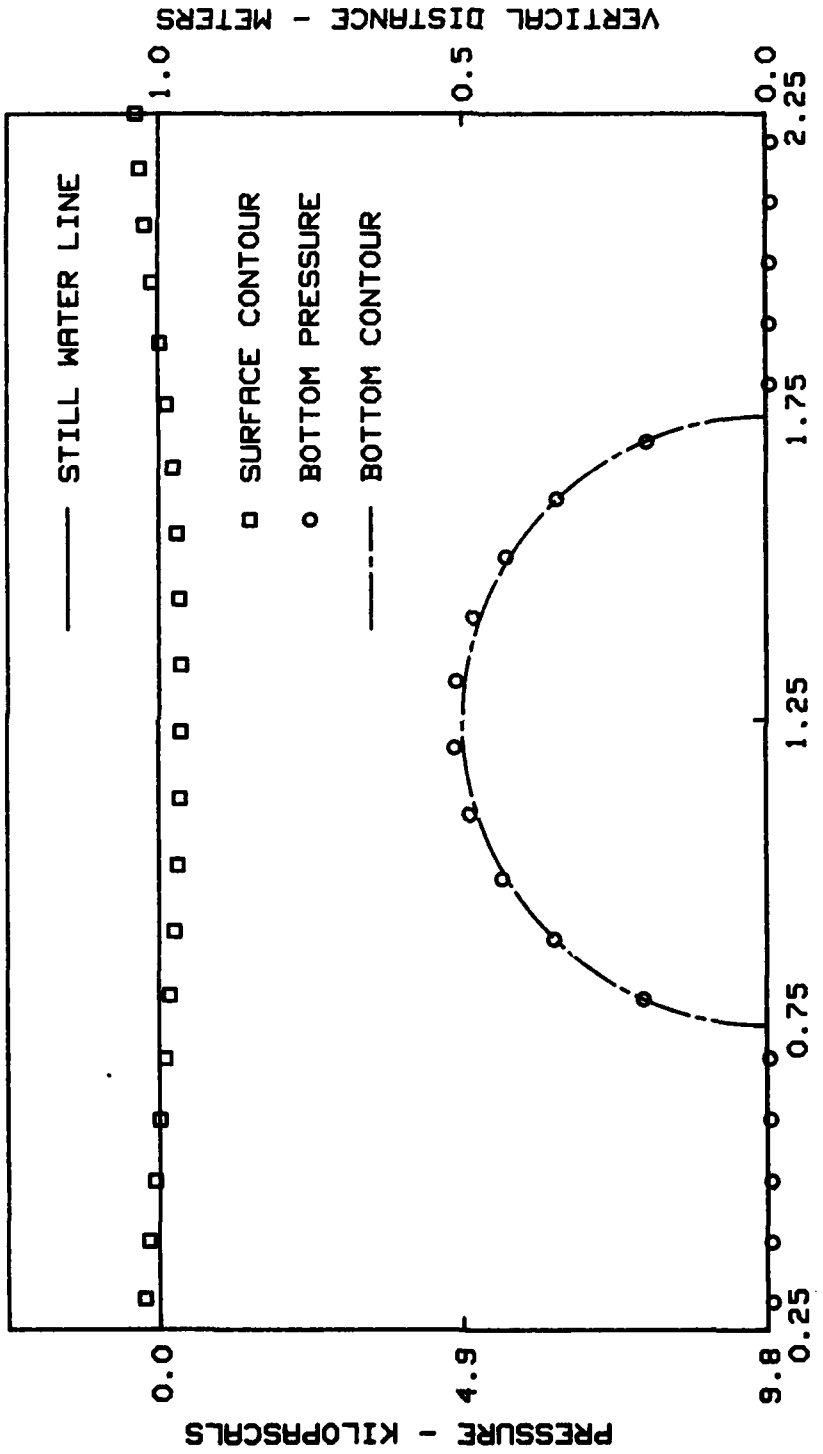

Figure 12 — The surface contour and the bottom pressure from a numerical calculation of the wave flow over a bottom seated half-cylinder at $t = 1.92$ sec (time step = 49, wavelength $\lambda = 2.5$ m, depth d 1 m, radius $a = 0.5$ m).

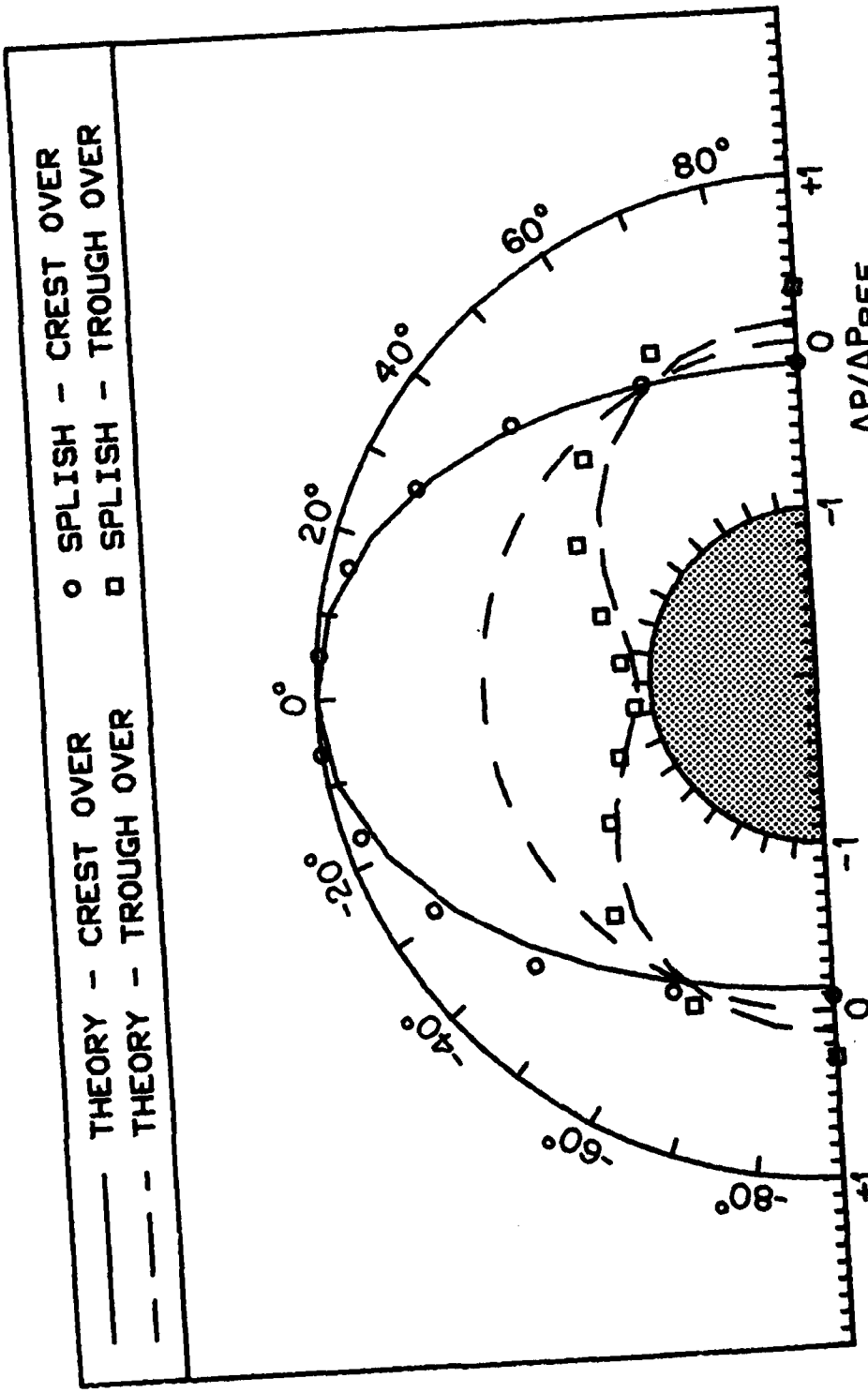

Figure 13 — A comparison of the distribution of pressure fluctuations around the half-cylinder from fifth-order wave theory and from a SPLISH calculation, for wave crest and through passage (wavelength $\lambda = 2.5$ m, depth $d = 1$ m, radius $a = 0.5$ m).

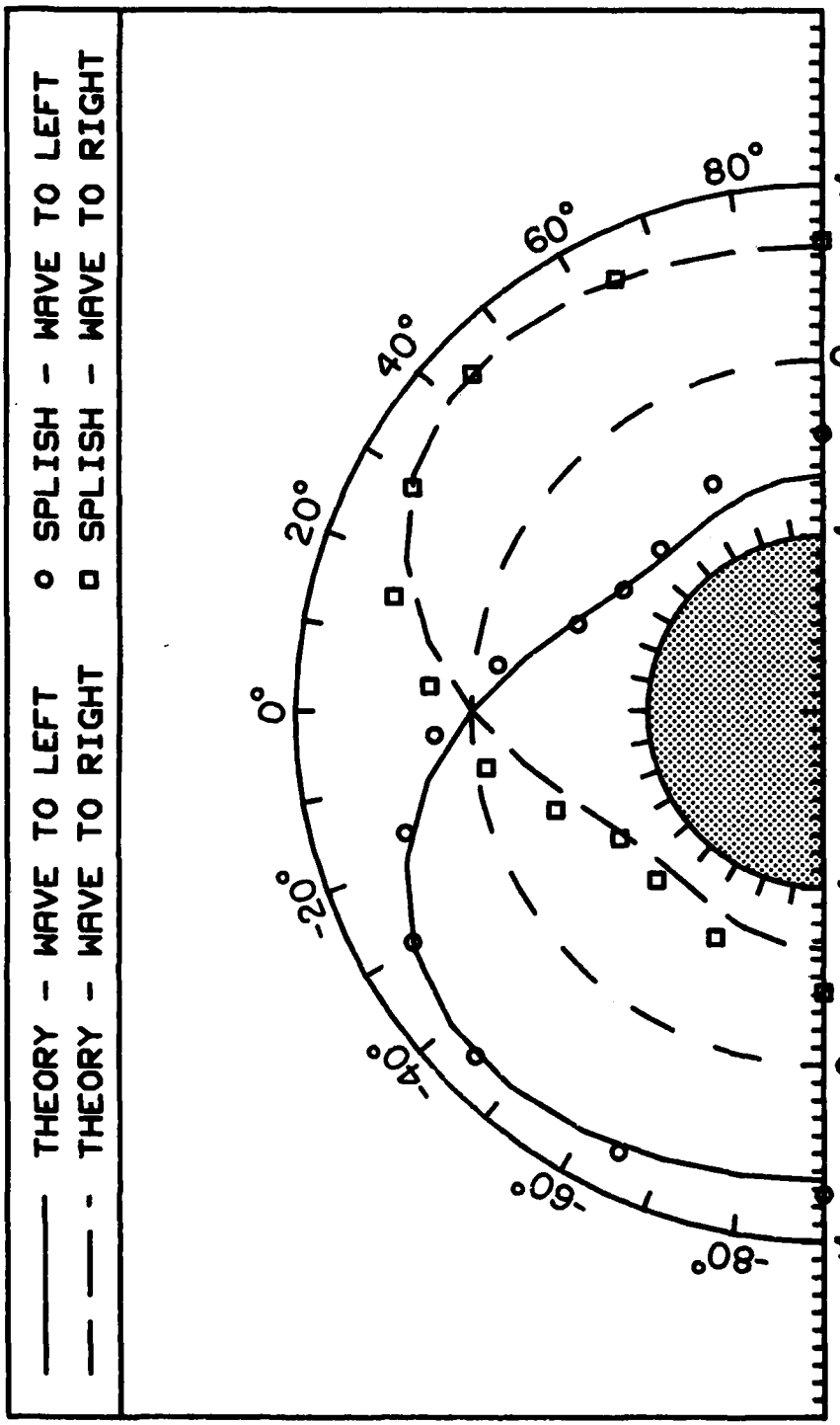

Figure 14 — A comparison of the distribution of pressure fluctuations around the half-cylinder from fifth-order wave theory and from a SPLISH calculation, for wave crest to the left and the right of the half-cylinder (wavelength λ = 2.5 m, depth d = 1 m, radius a = 0.5 m).

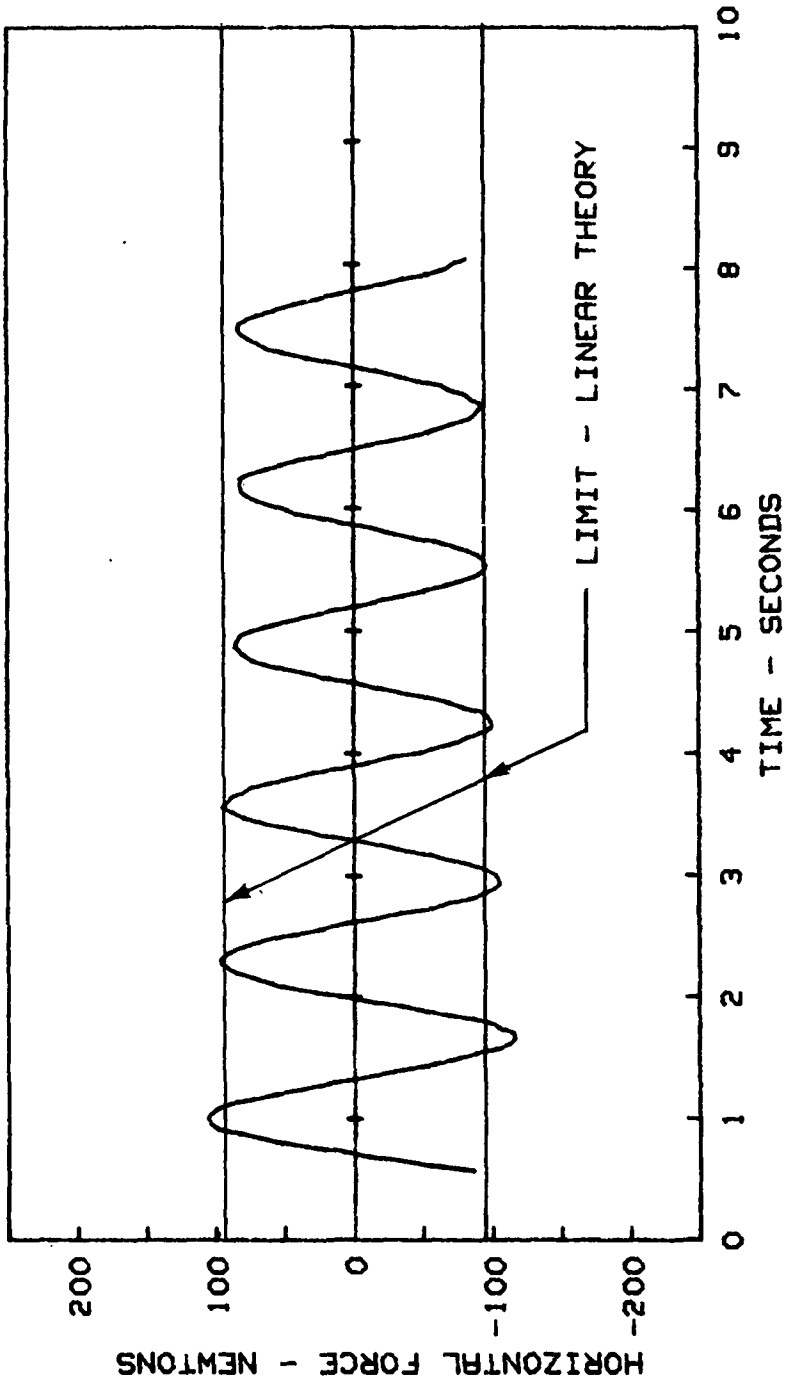

Figure 15 — The horizontal component of force on the half-cylinder from a SPLISH calculation (wavelength $\lambda = 2.5$ m, depth $d = 1$ m, radius $a = 0.5$ m).

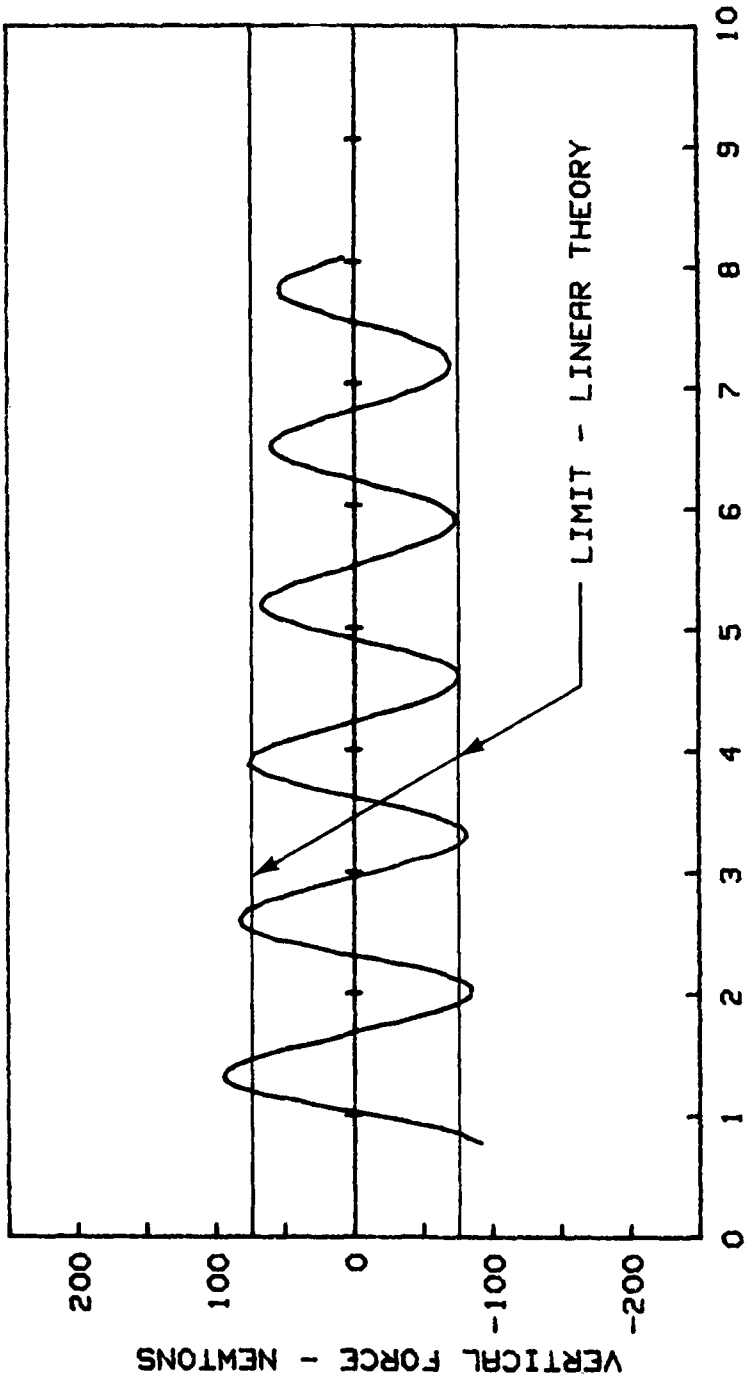

Figure 16 — The vertical component of force on the half-cylinder from a SPLISH calculation (wavelength $\lambda = 2.5$ m, depth $d = 1$ m, radius $a = 0.5$ m).

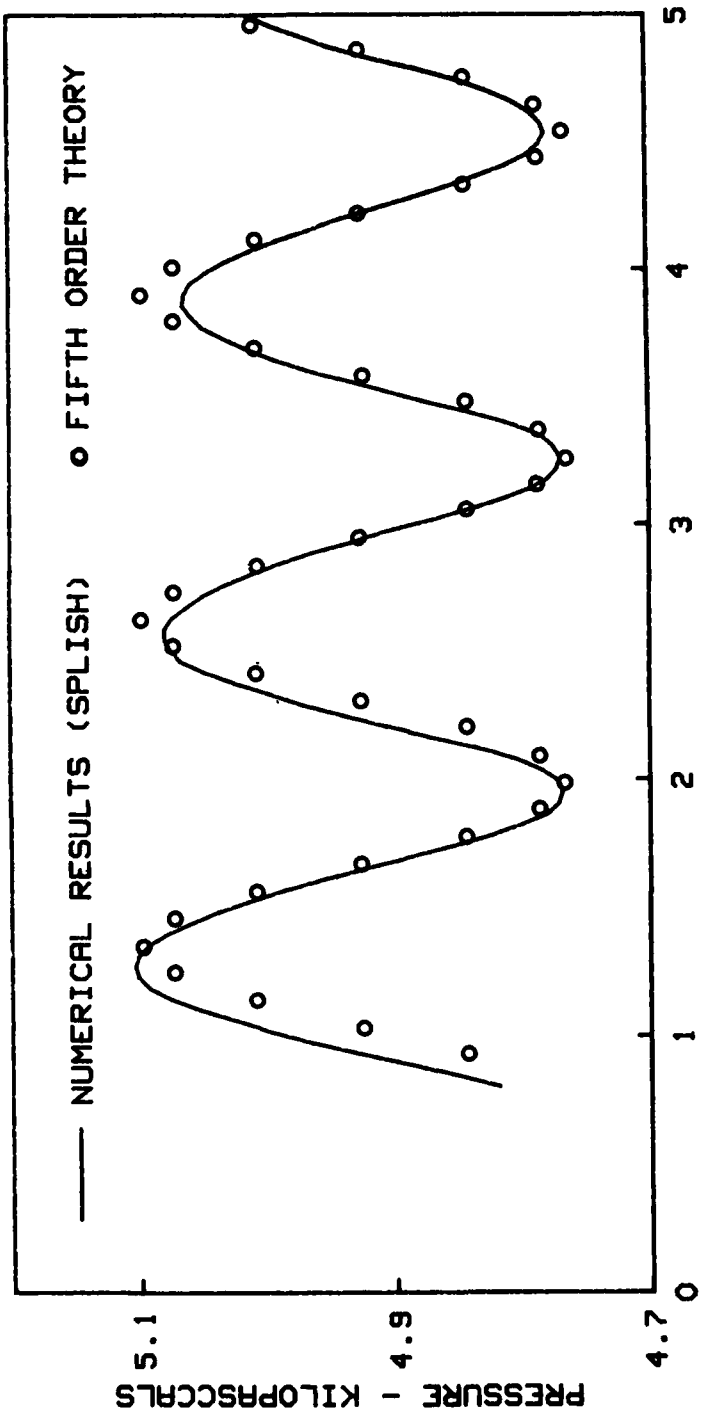

Figure 17 — A comparison of the pressure time history at the top of a bottom seated half-cylinder from a SPLISH calculation and from fifth-order wave theory (wavelength $\lambda = 2.5$ m, depth $d = 1$ m, radius $a = 0.5$ m, wave amplitude $h = 0.38$ m).

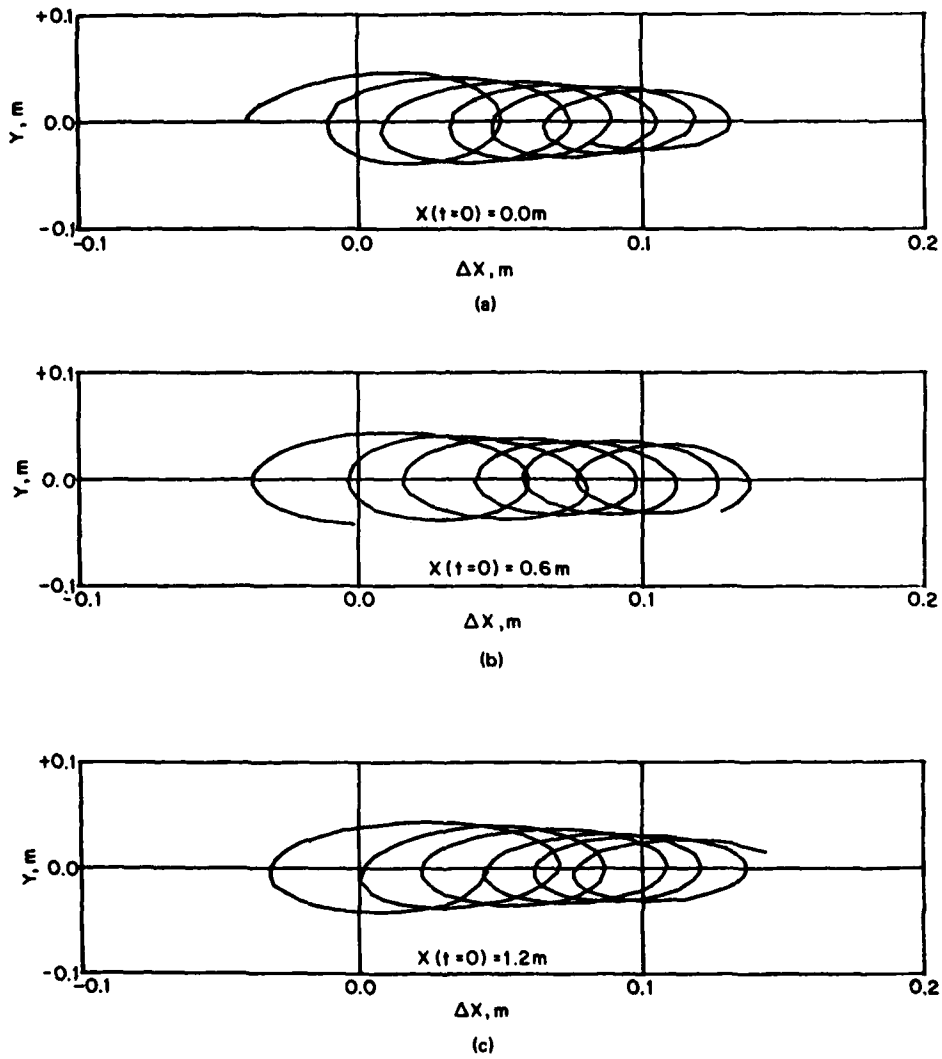

Figure 18 — Particle paths on the free surface from a numerical calculation of wave flow over a bottom seated half-cylinder (wavelength $\lambda = 2.5$ m, depth $d = 1$ m, radius $a = 0.5$ m).

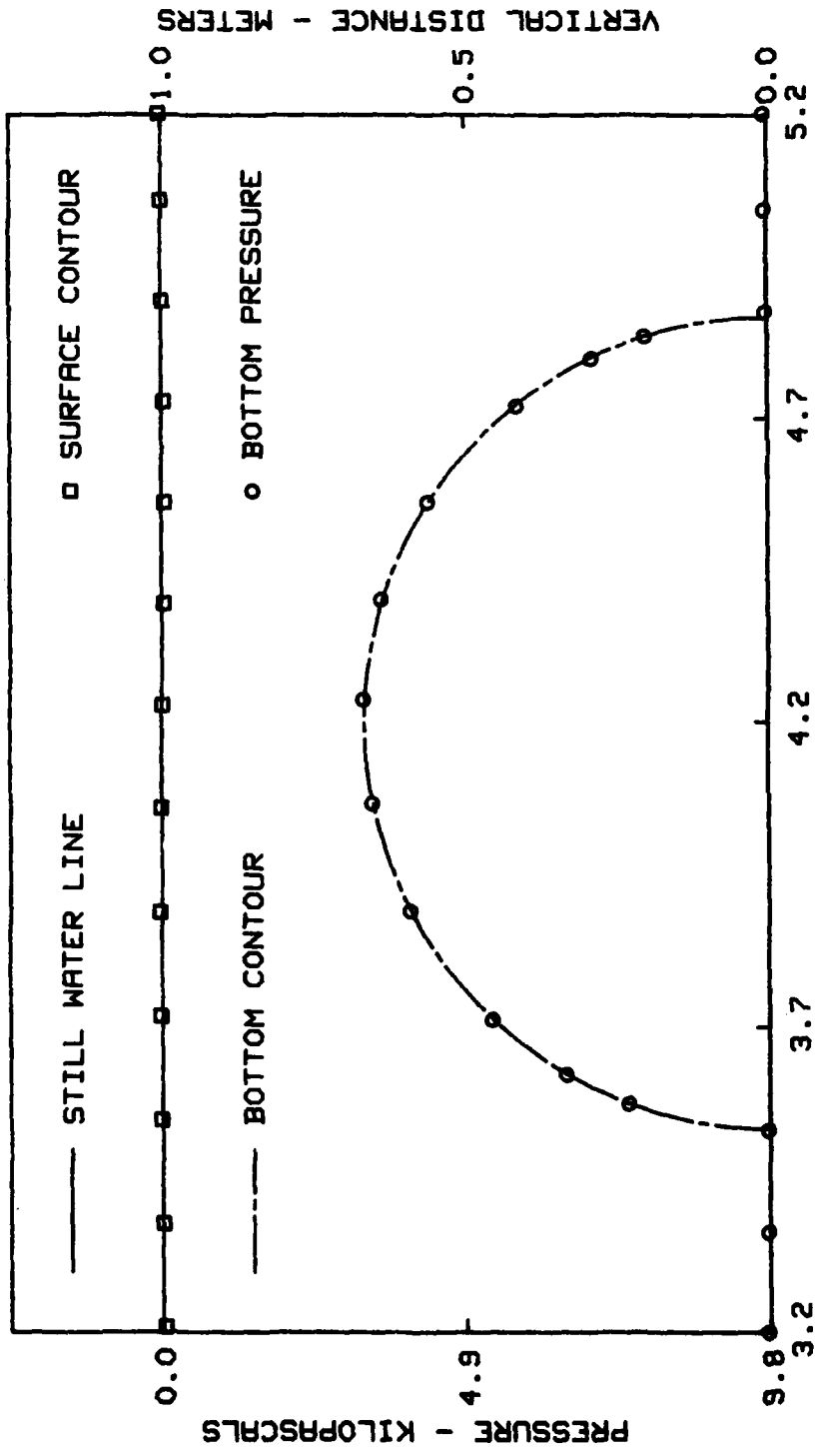

Figure 19 — The surface contour and the bottom pressure from a numerical calculation of the high reflection wave flow over a bottom seated half-cylinder at $t = 0.2$ sec (time step = 11, wavelength $\lambda = 8.4$ m, depth $d = 1$ m, radius a 0.667 m).

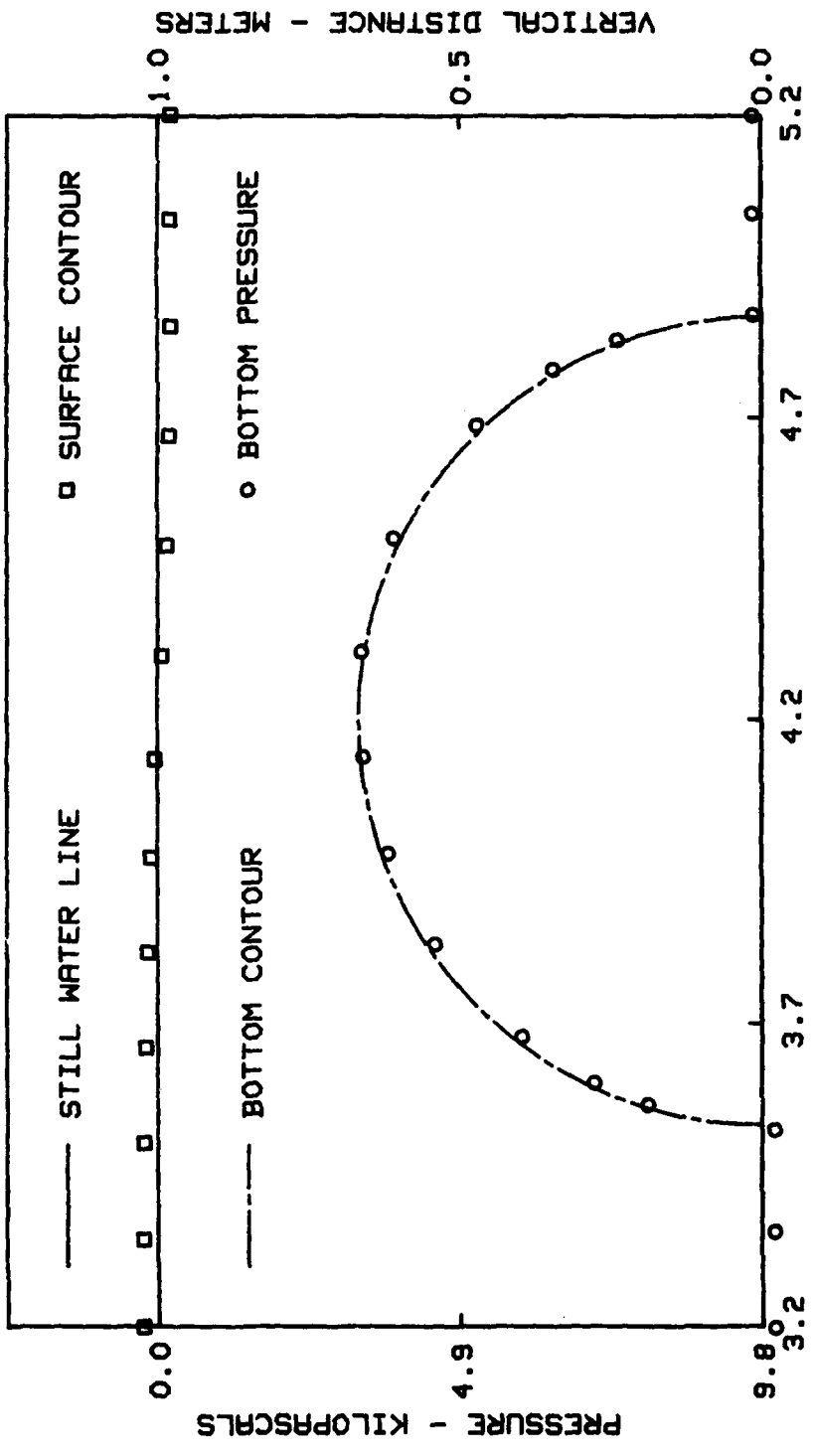

Figure 20 — The surface contour and the bottom pressure from a numerical calculation of the high reflection wave flow over a bottom seated half-cylinder at t = 1.88 sec (time step = 95, wavelength λ 8.4 m, depth d = 1 m, radius a = 0.667 m).

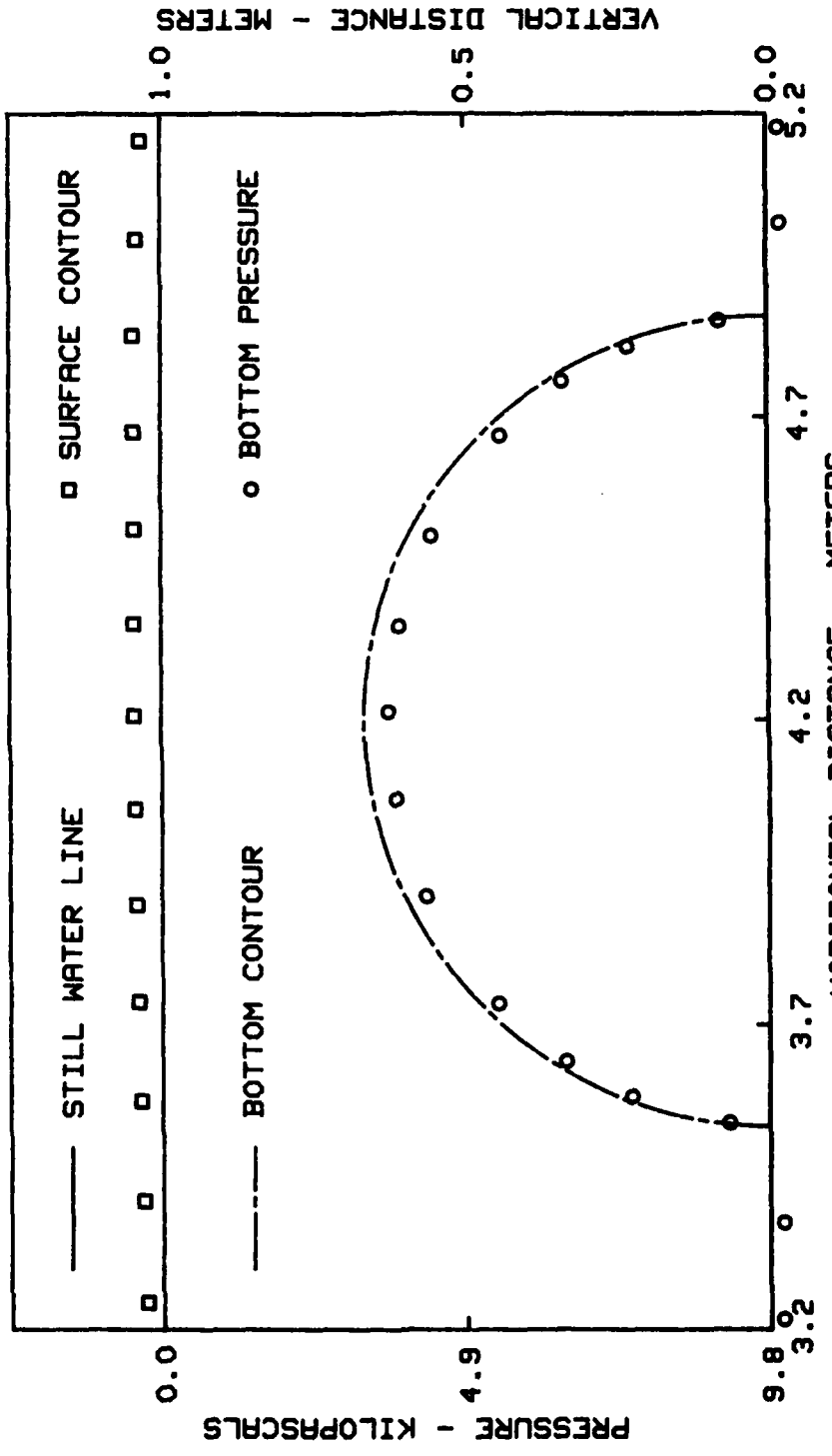

Figure 21 — The surface contour and the bottom pressure from a numerical calculation of the high reflection wave flow over a bottom seated half-cylinder at $t = 2.68$ sec (time step = 135, wavelength $\lambda = 8.4$ m, depth $d = 1$ m, radius $a = 0.667$ m).

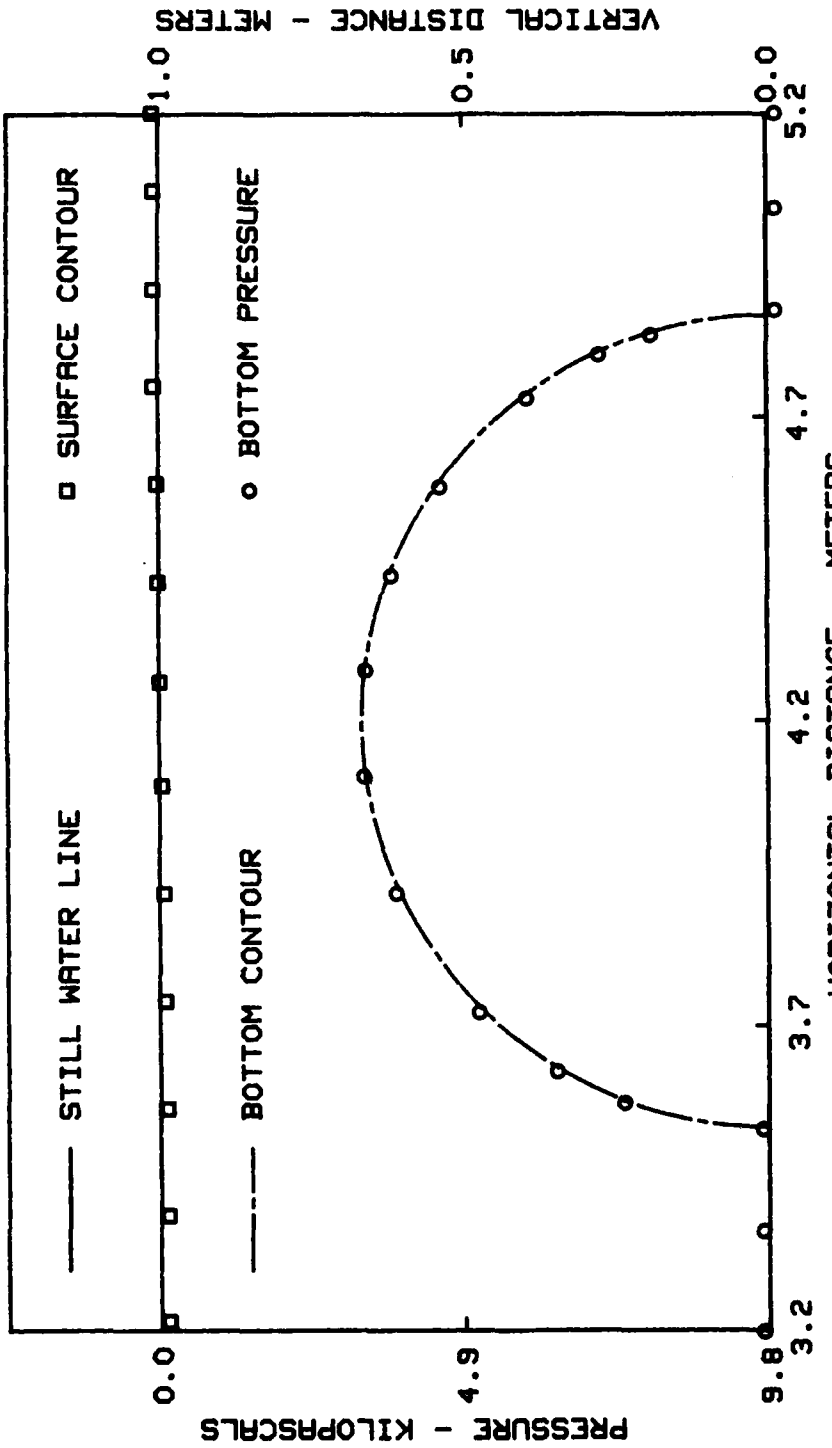

Figure 22 — The surface contour and the bottom pressure from a numerical calculation of the high reflection wave flow over a bottom seated half-cylinder of $t = 3.28$ sec (time step = 165, wavelength $\lambda = 8.4$ m, depth $d = 1$ m, radius $a = 0.667$ m).

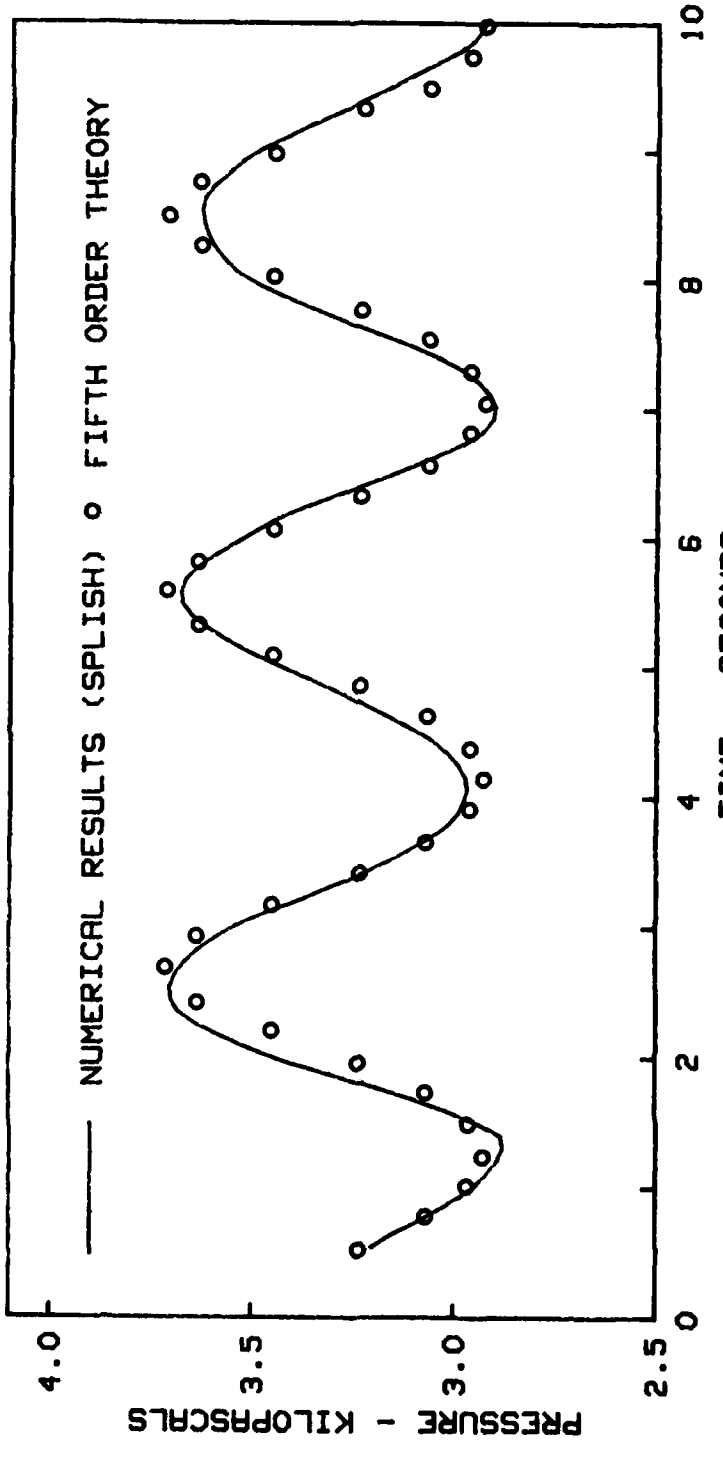

Figure 23 — A comparison of the pressure-time history at the top of a bottom seated half-cylinder from a SPLISH calculation and fifth-order wave theory calculation for high reflection wave flow (wave length $\lambda = 8.4$ m, depth $d = 1$ m, radius $a = 0.667$ m wave amplitude $H = 0.04$ m).

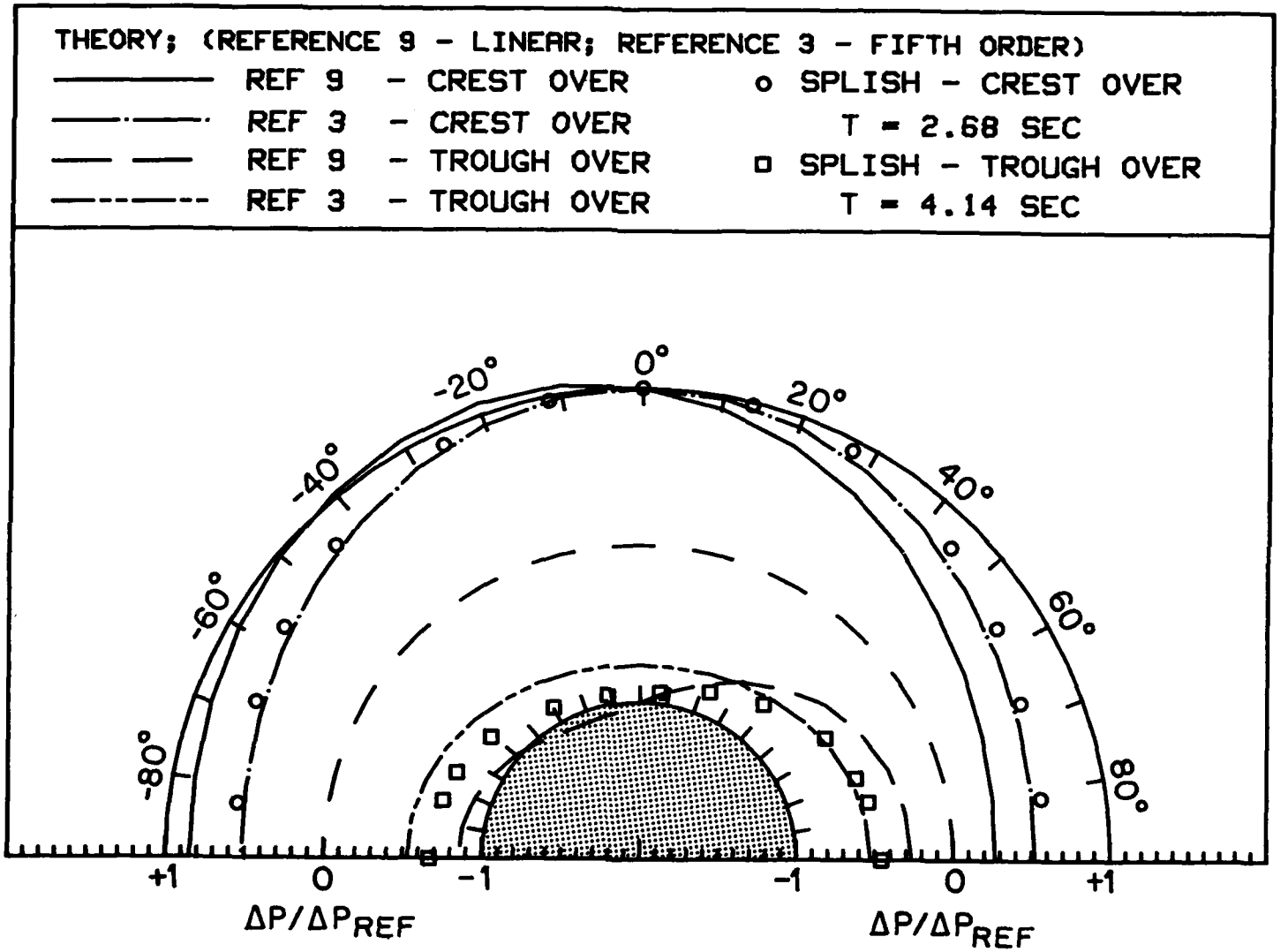

Figure 24 — A comparison of the distribution of pressure fluctuations around the half-cylinder from linear (Reference 9) and fifth-order (Reference 3) wave theory and a SPLISH calculation, for wave crest and trough passage over the cylinder (high reflection wave flow; wavelength $\lambda = 8.4$ m, depth $d = 1$ m, radius $a = 0.667$ m).

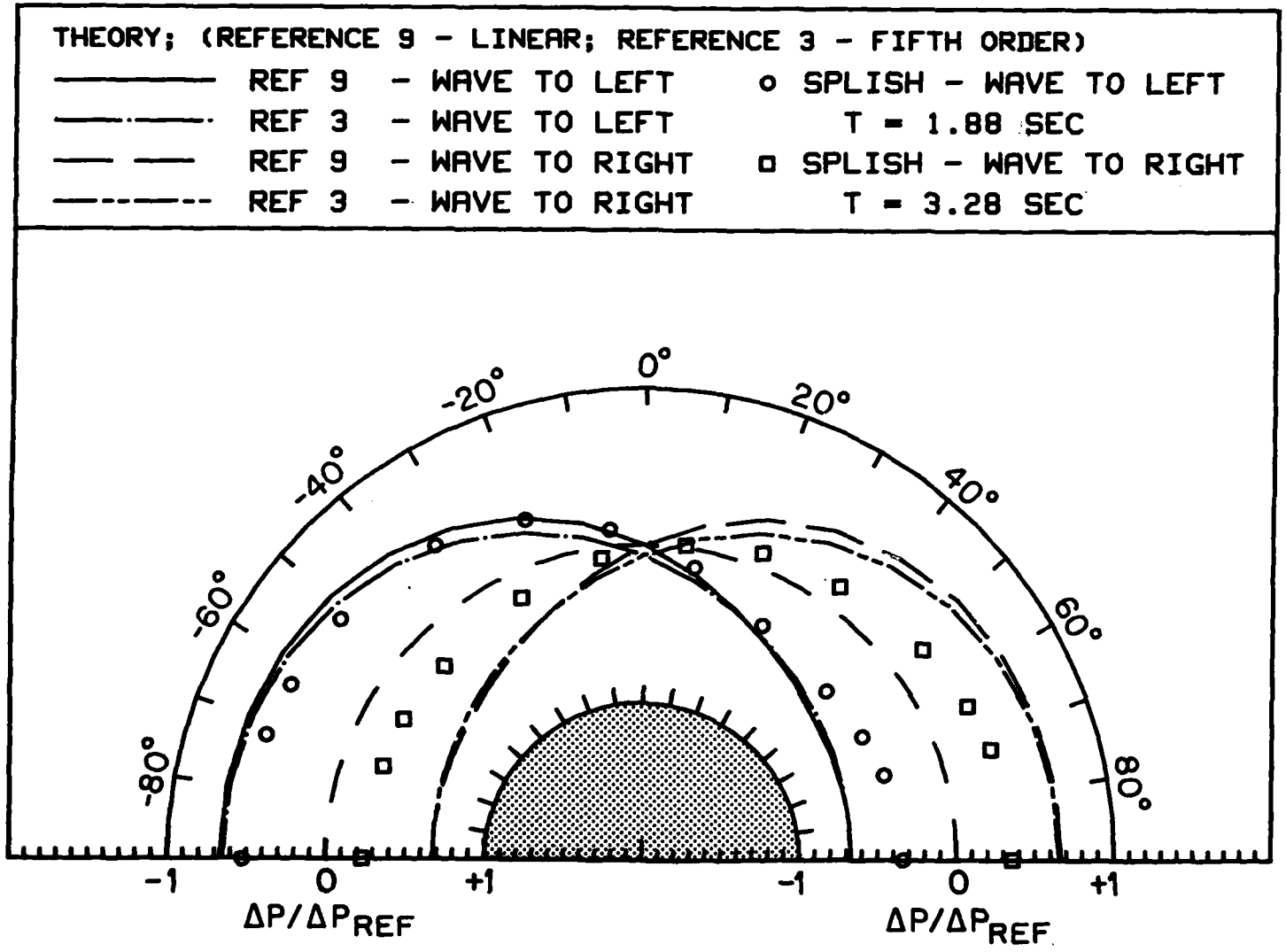

Figure 25 — A comparison of the distribution of pressure fluctuations around the half-cylinder from linear (Reference 9) and fifth-order (Reference 3) wave theory and a SPLISH calculation for wave crest to the left and to the right of the half-cylinder (high reflection wave flow; wavelength $\lambda = 8.4$ m, depth $d = 1$ m, radius $a = 0.667$ m).

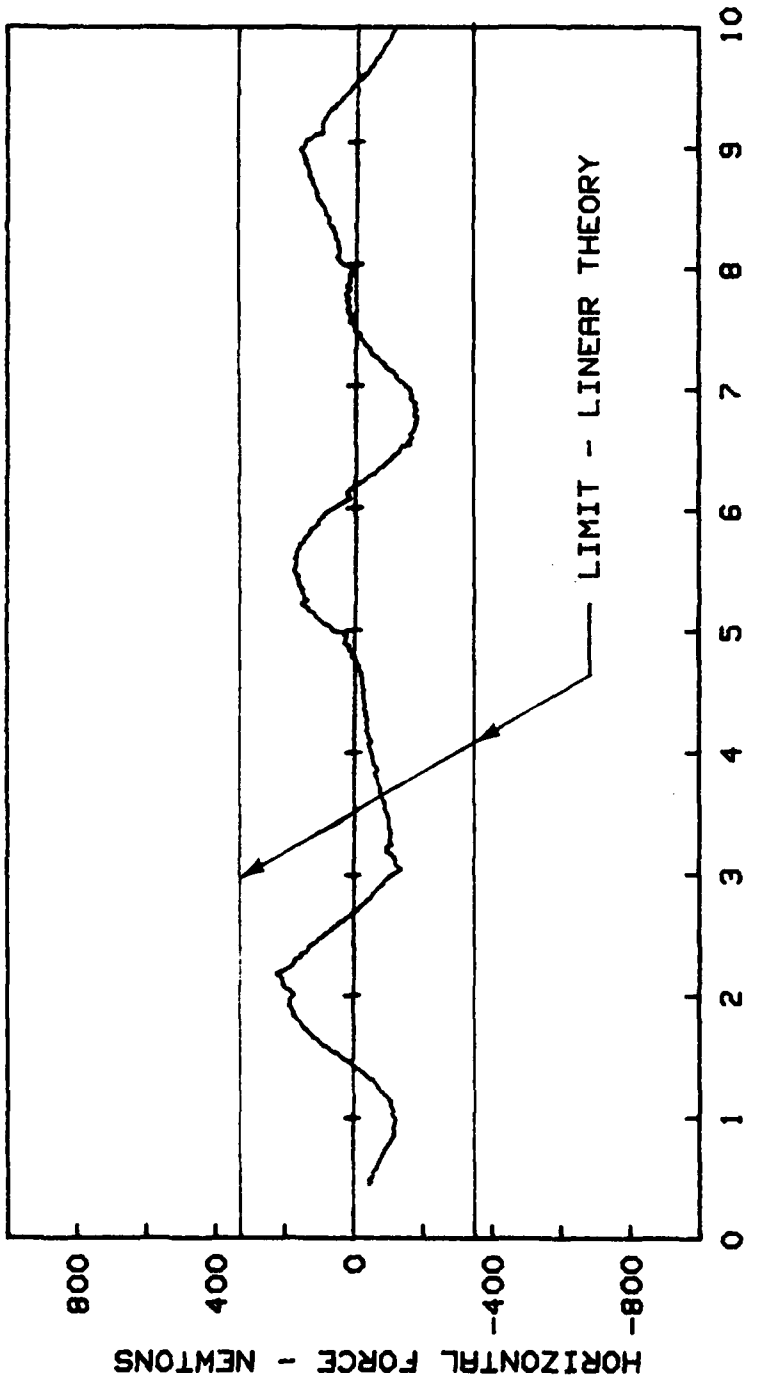

Figure 26 — The horizontal component of force on the bottom seated half-cylinder from a SPLISH calculation (high reflection wave flow; wavelength $\lambda = 8.4$ m, depth $d = 1$ m, radius $a = 0.667$ m).

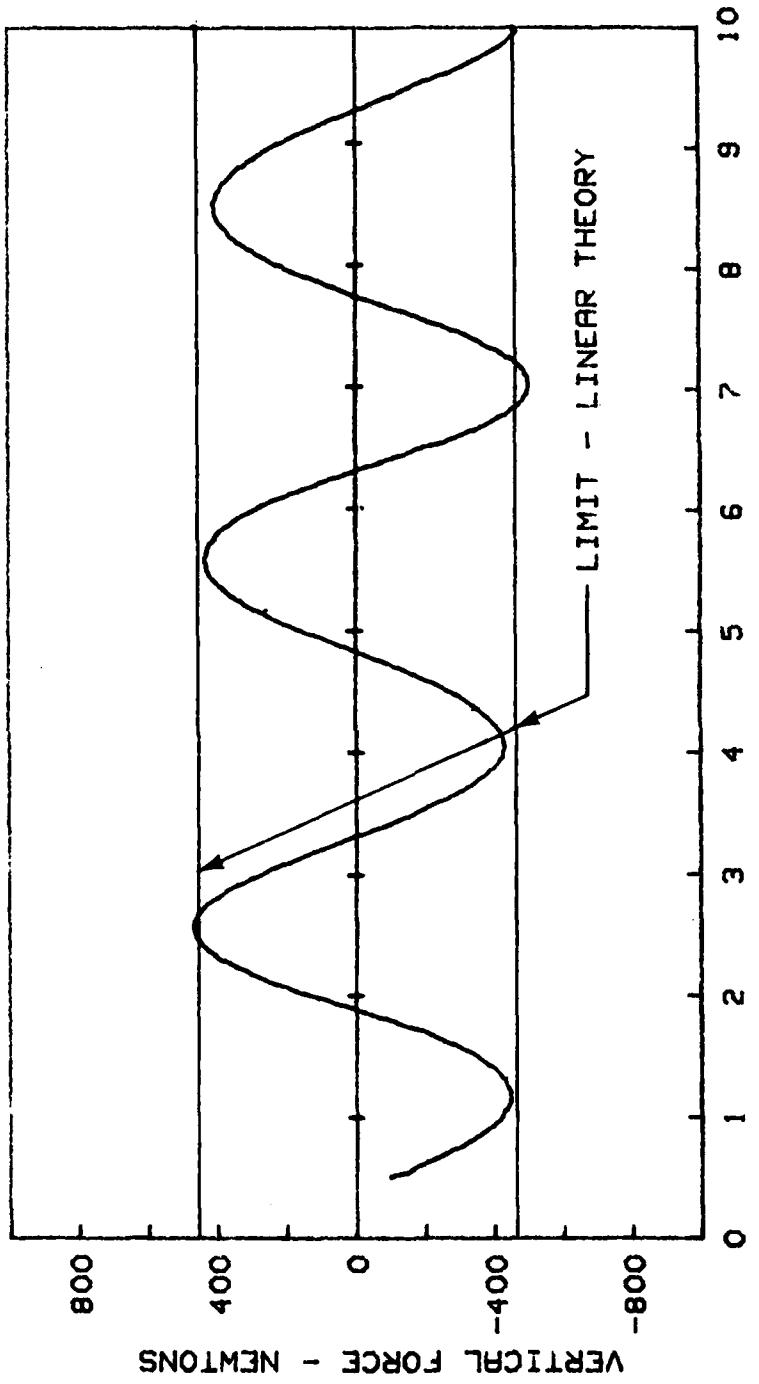

Figure 27 – The vertical component of force on the bottom seated half-cylinder from a SPLISH calculation (high reflection wave flow; wavelength λ = 8.4 m, depth d = 1 m, radius a = 0.667 m).

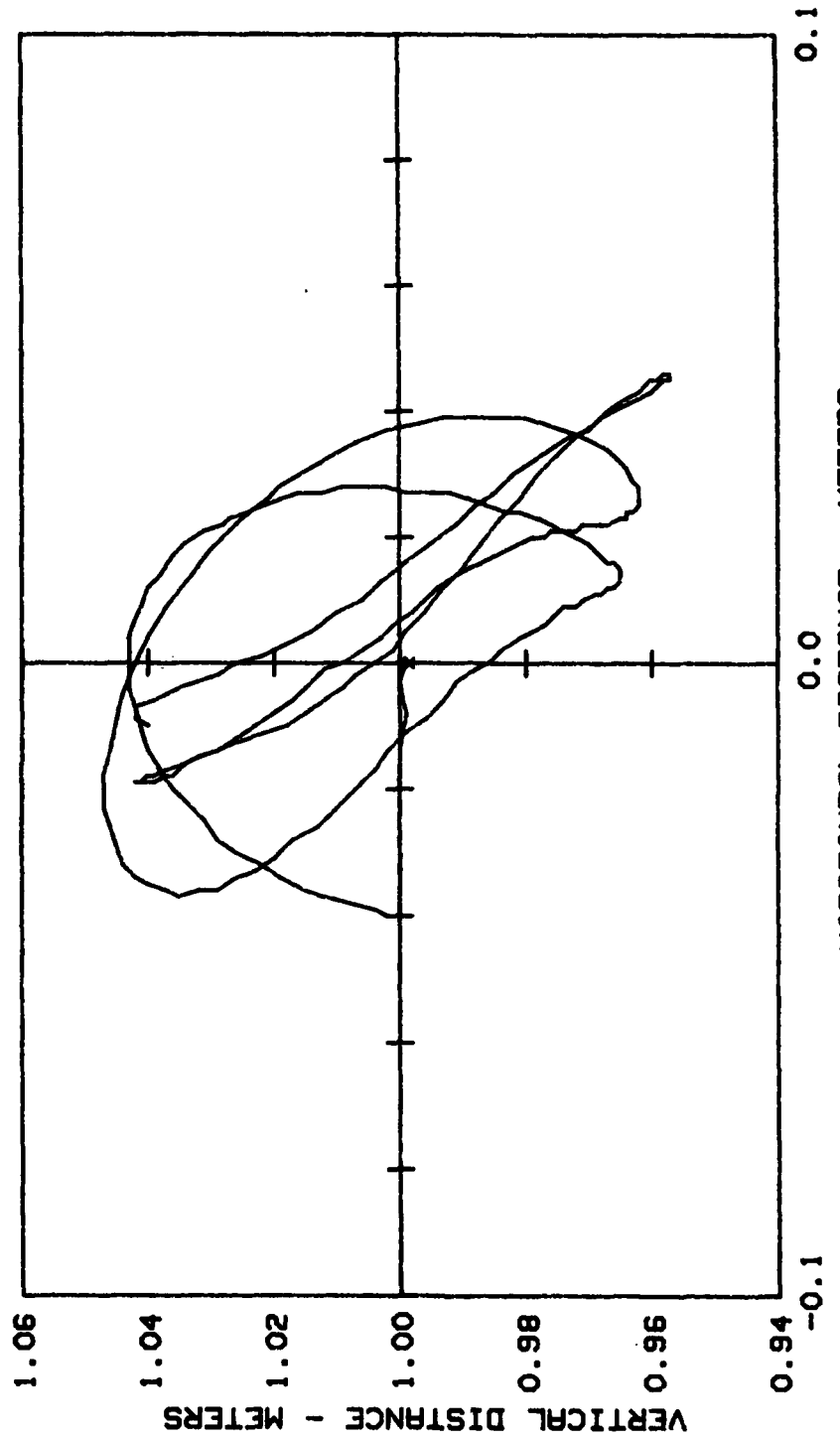

Figure 28 – The particle path (at $x = 0$ m) on the free surface from a SPLISH calculation of the high reflection wave flow over a bottom seated half-cylinder (wavelength $\lambda = 8.4$ m, depth $d = 1$ m, radius $a = 0.667$ m).

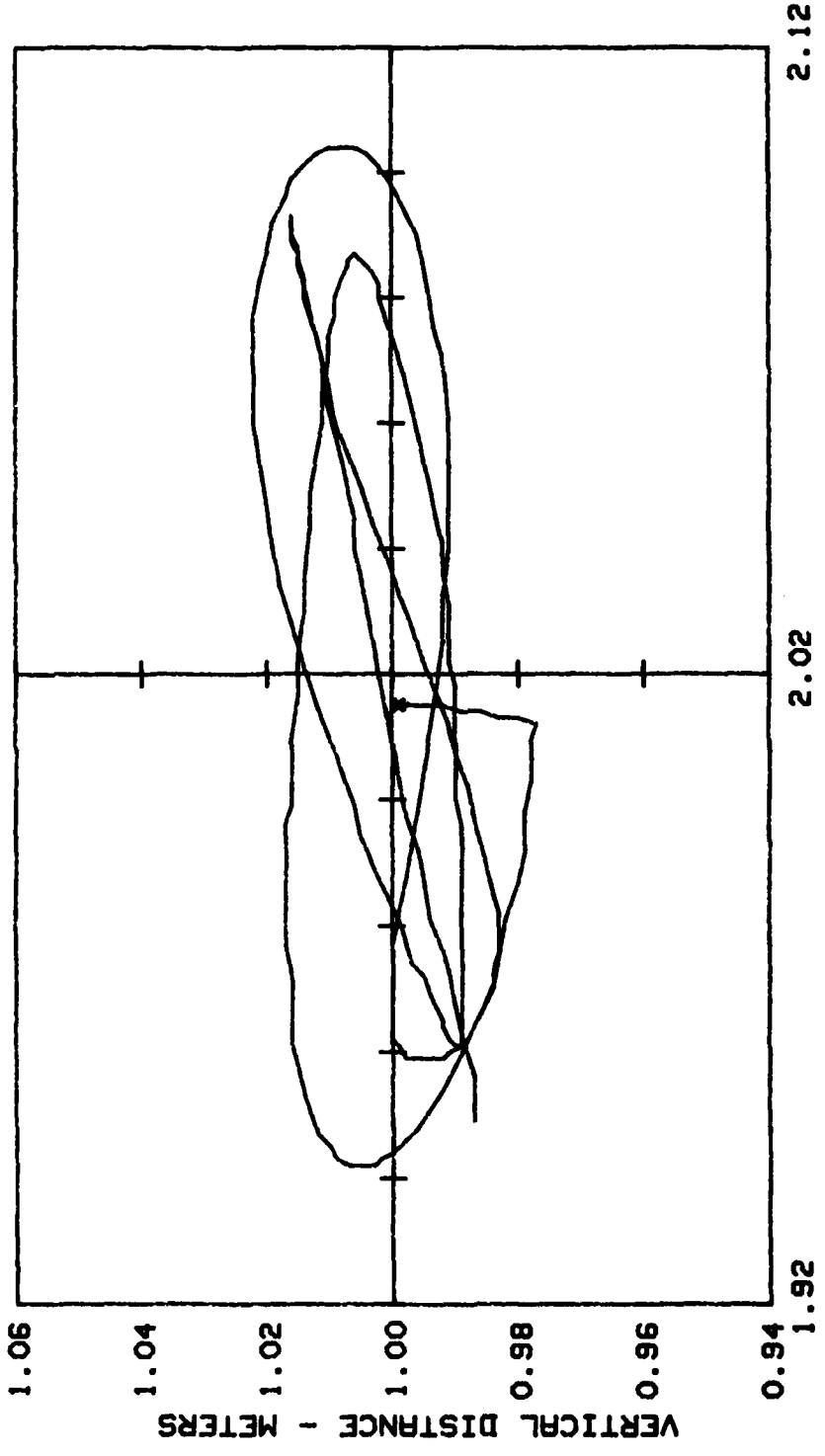

Figure 29 — The particle path (at $x = 2.0$ m) on the free surface from a SPLISH calculation of the high reflection wave flow over a bottom seated half-cylinder (wavelength $\lambda = 8.4$ m, depth $d = 1$ m, radius $a = 0.667$ m).

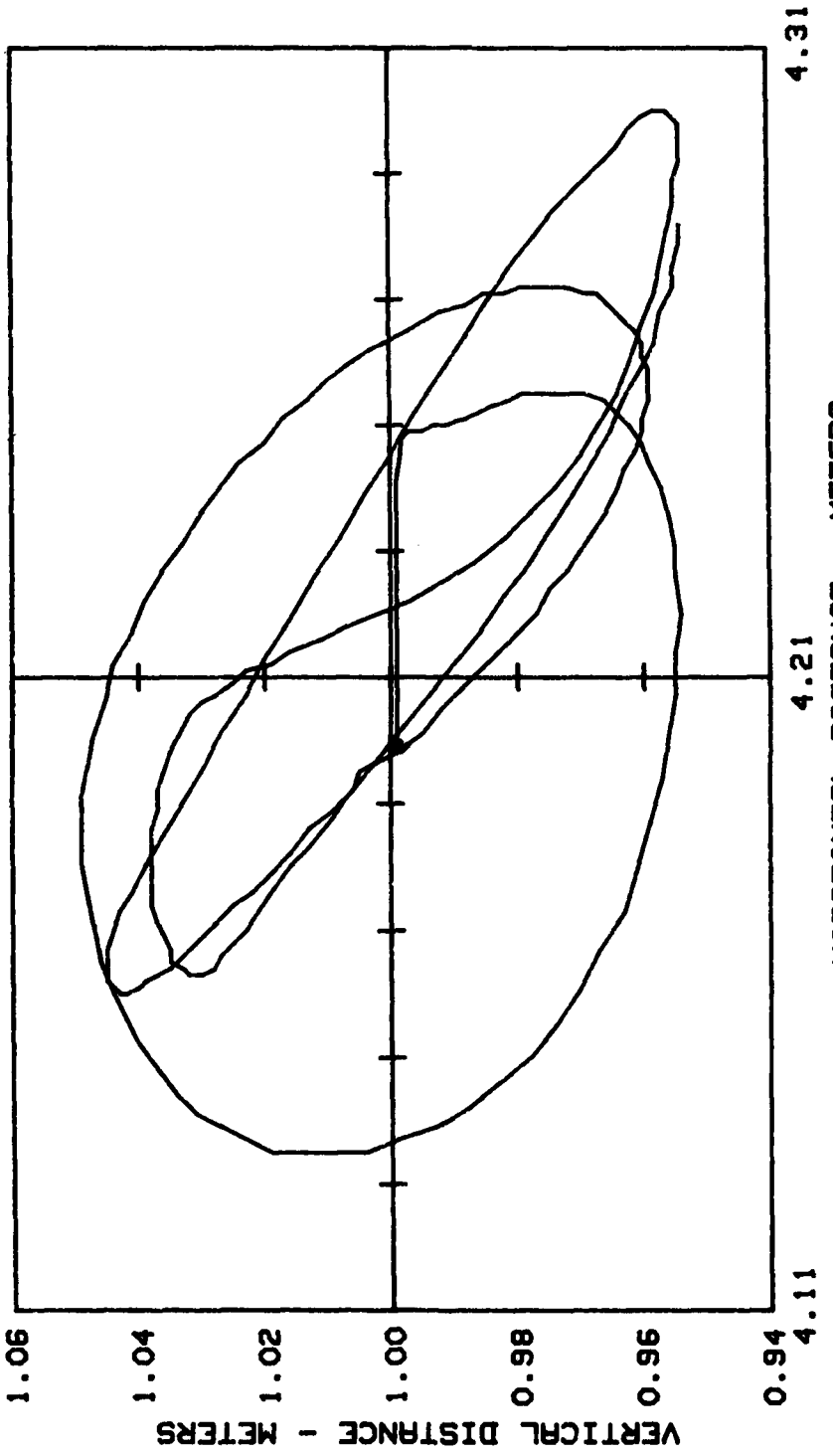

Figure 30 — The particle path (at x = 4.2 m) on the free surface from a SPLISH calculation of the high reflection flow over a bottom seated half-cylinder (wavelength λ = 8.4 m, depth d = 1 m, radius a = 0.667 m).

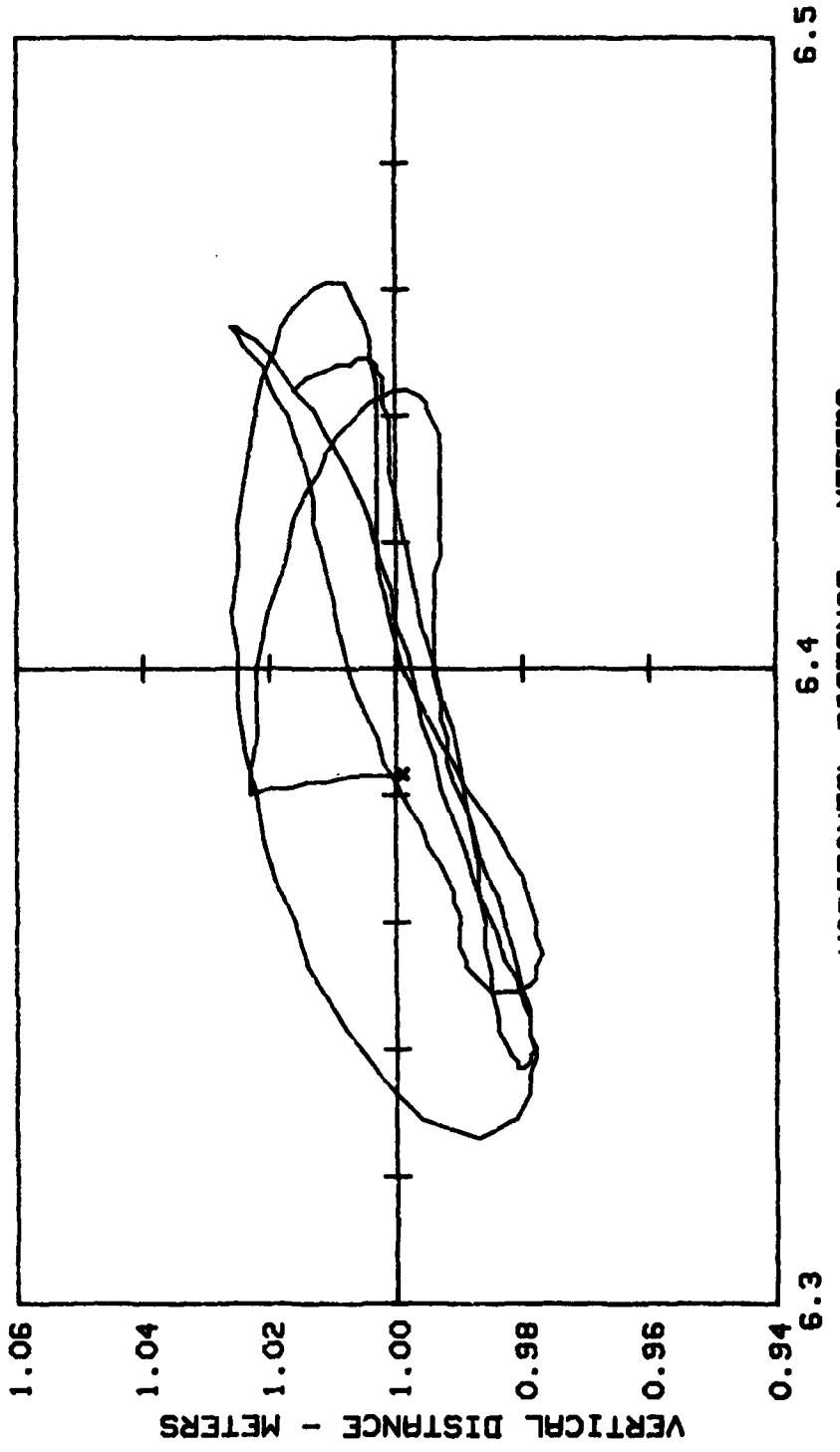

Figure 31 – The particle path (at x = 6.4 m) on the free surface from a SPLISH calculation of the high reflection wave flow flow over a bottom seated half-cylinder (wavelength λ = 8.4 m, depth d = 1 m, radius a = 0.667 m).

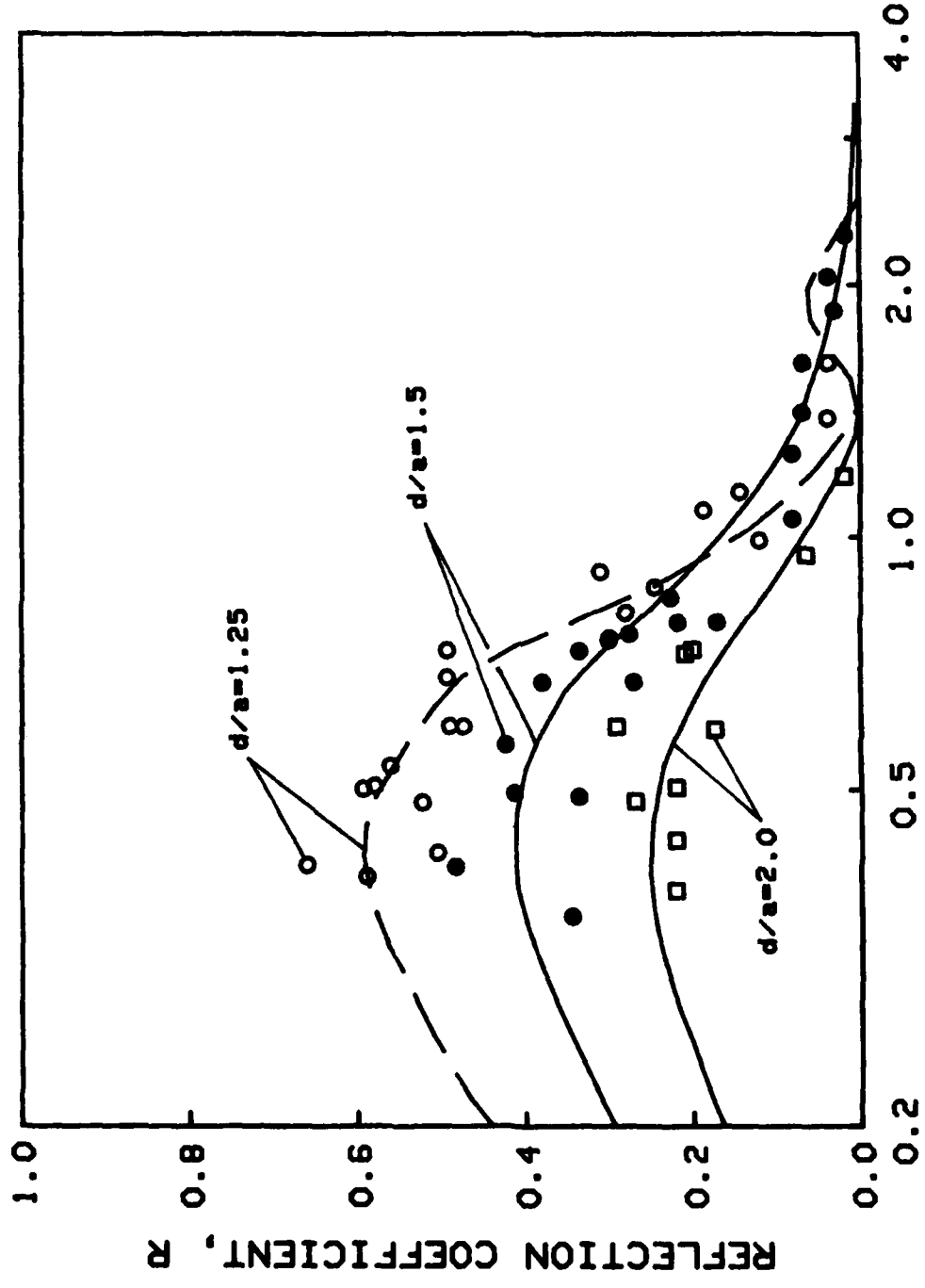

Figure 32. Experimental (•) and theoretical (—) values for the wave reflection coefficient of a bottom-seated half cylinder. Theoretical values are from Naftzger and Chakrabarti (1979).

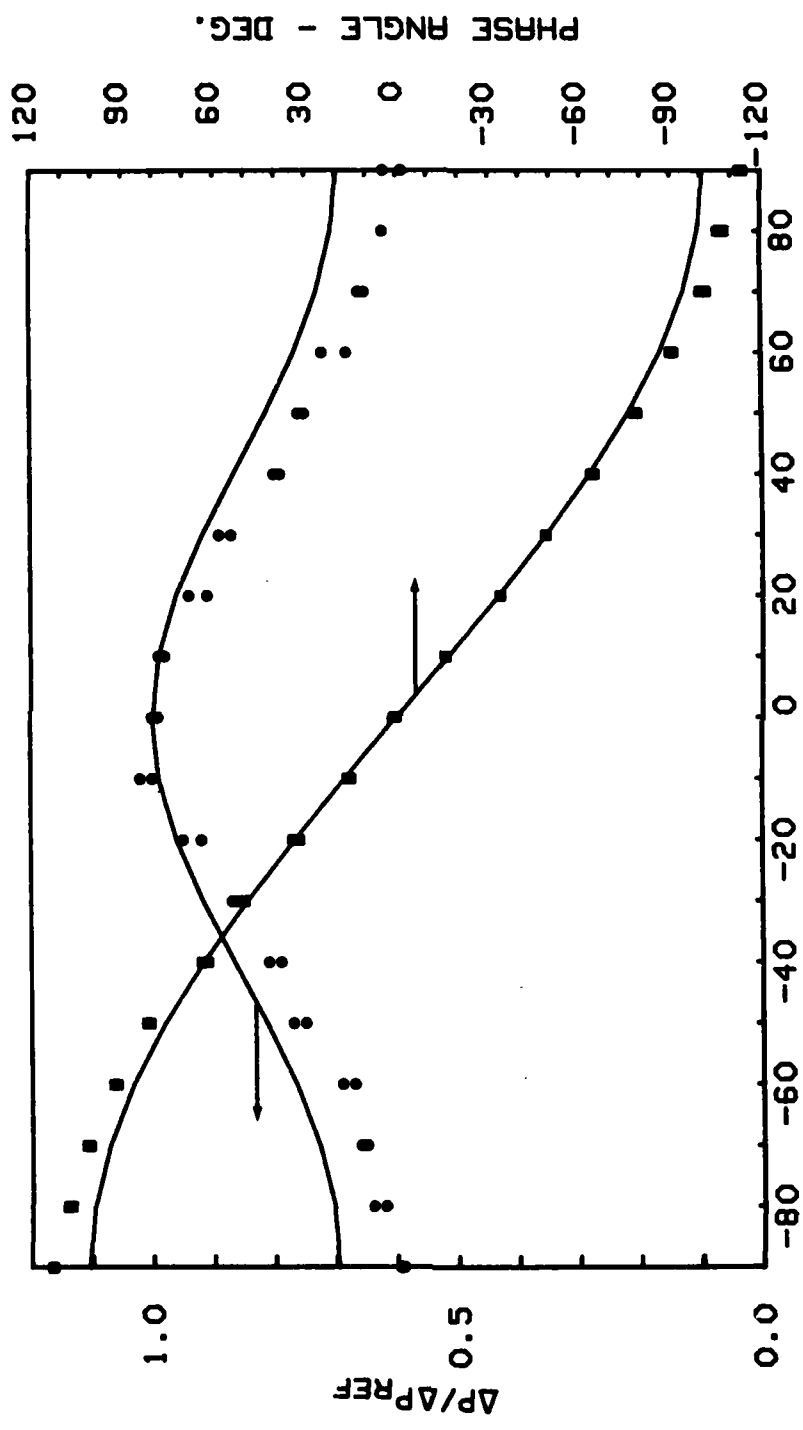

Figure 33. A comparison of theoretical (Chakrabarti and Naftzger, 1974) and experimental results for the azimuthal distribution of pressure fluctuation magnitudes and relative phases on a bottom-seated half cylinder in waves (low reflection wave flow, $d/a = 2.0$, $ka = 1.25$, $R \lesssim 0.05$).

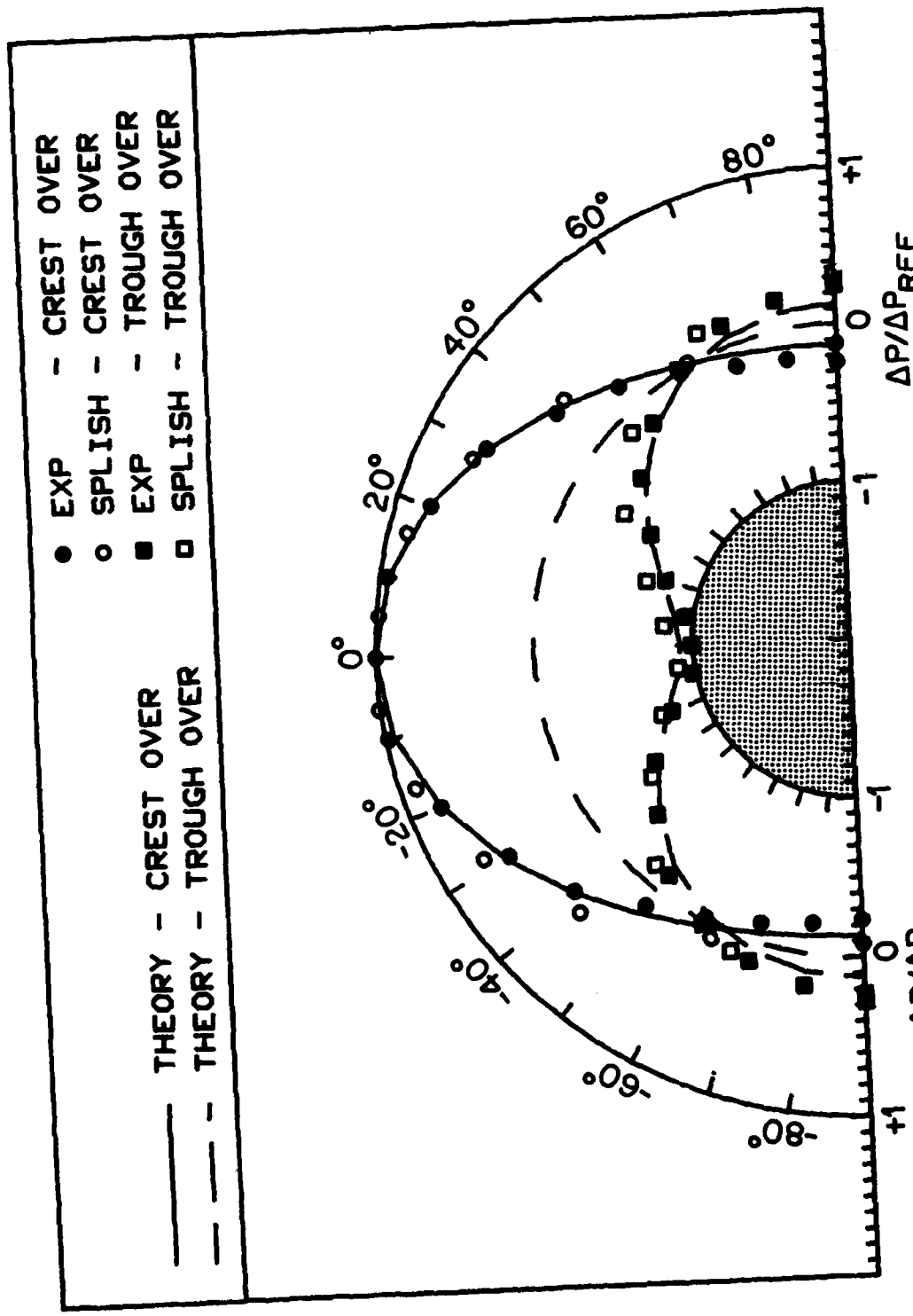

Figure 34. A comparison of theoretical (Chakrabarti and Naftzger, 1974), numerical, and experimental results for selected instantaneous pressure distributions on a bottom-seated half-cylinder in waves, for wave crest and trough passage (low reflection wave flow, $d/a = 2.0$, $ka = 1.25$, $R \leq 0.05$)

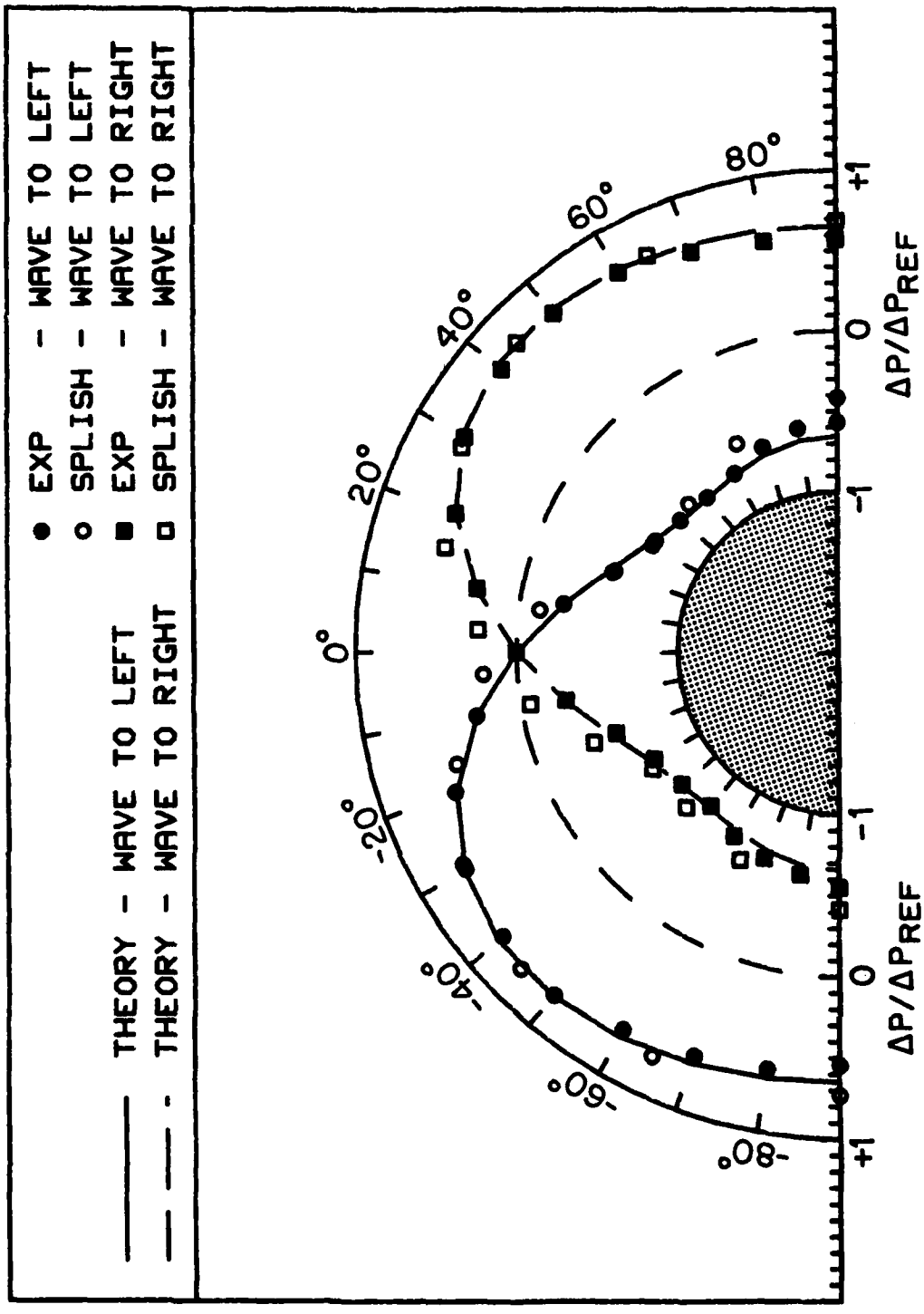

Figure 35. A comparison of theoretical (Chakrabarti and Naftzger, 1974), numerical, and experimental results for selected instantaneous pressure distributions on a bottom-seated half-cylinder in waves, for wave crest to the left and the right of the half-cylinder (low reflection wave flow, $d/a = 2.0$, $ka = 1.25$, $R \lesssim 0.05$).

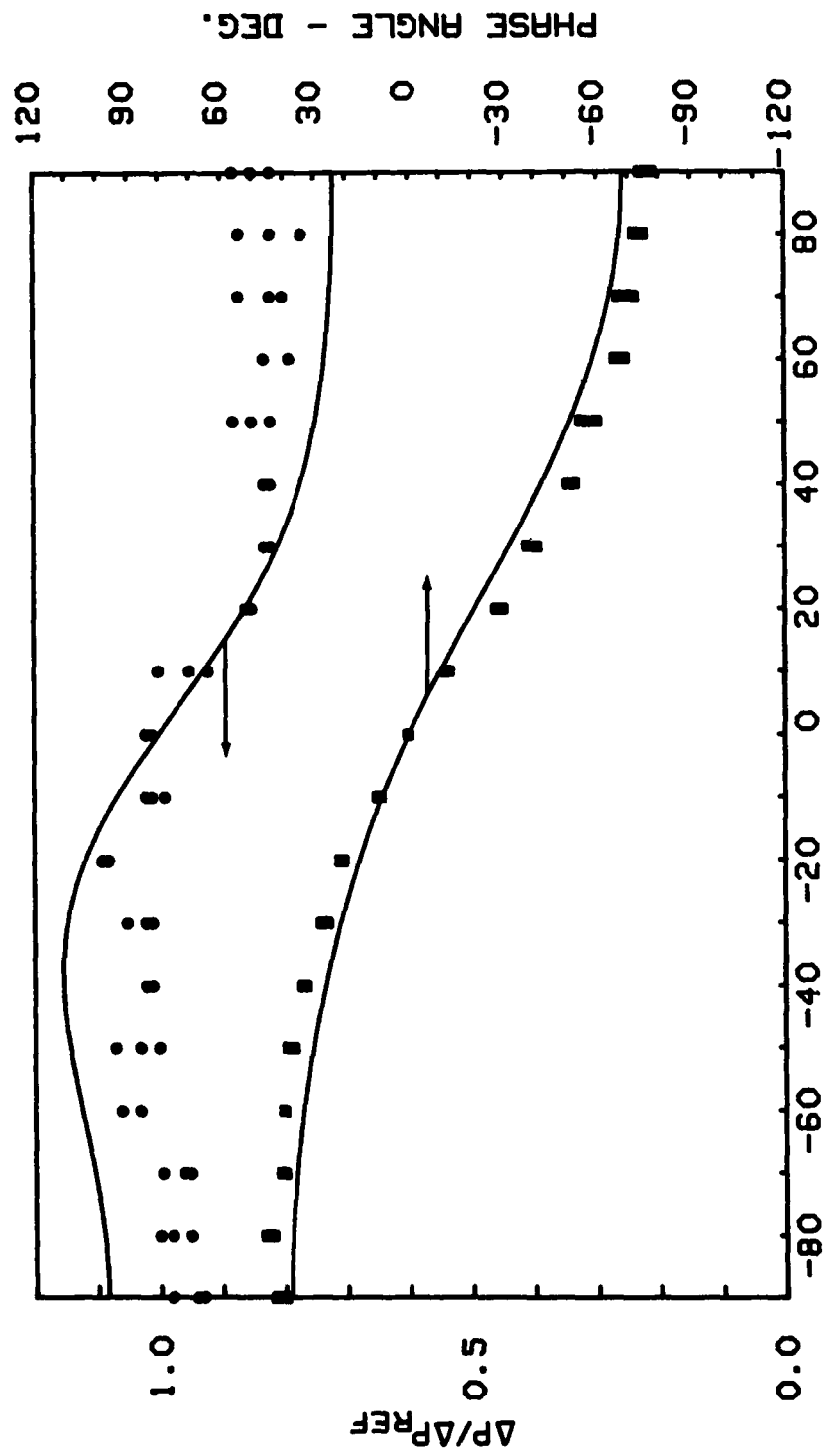

Figure 36. A comparison of theoretical (Naftzger and Chakrabarti, 1979) and experimental results for the azimuthal distribution of pressure fluctuation magnitudes and relative phases on a bottom-seated half cylinder in waves (high reflection wave flow, $d/a = 1.5$, $ka = 0.5$, $R \approx 0.4$).

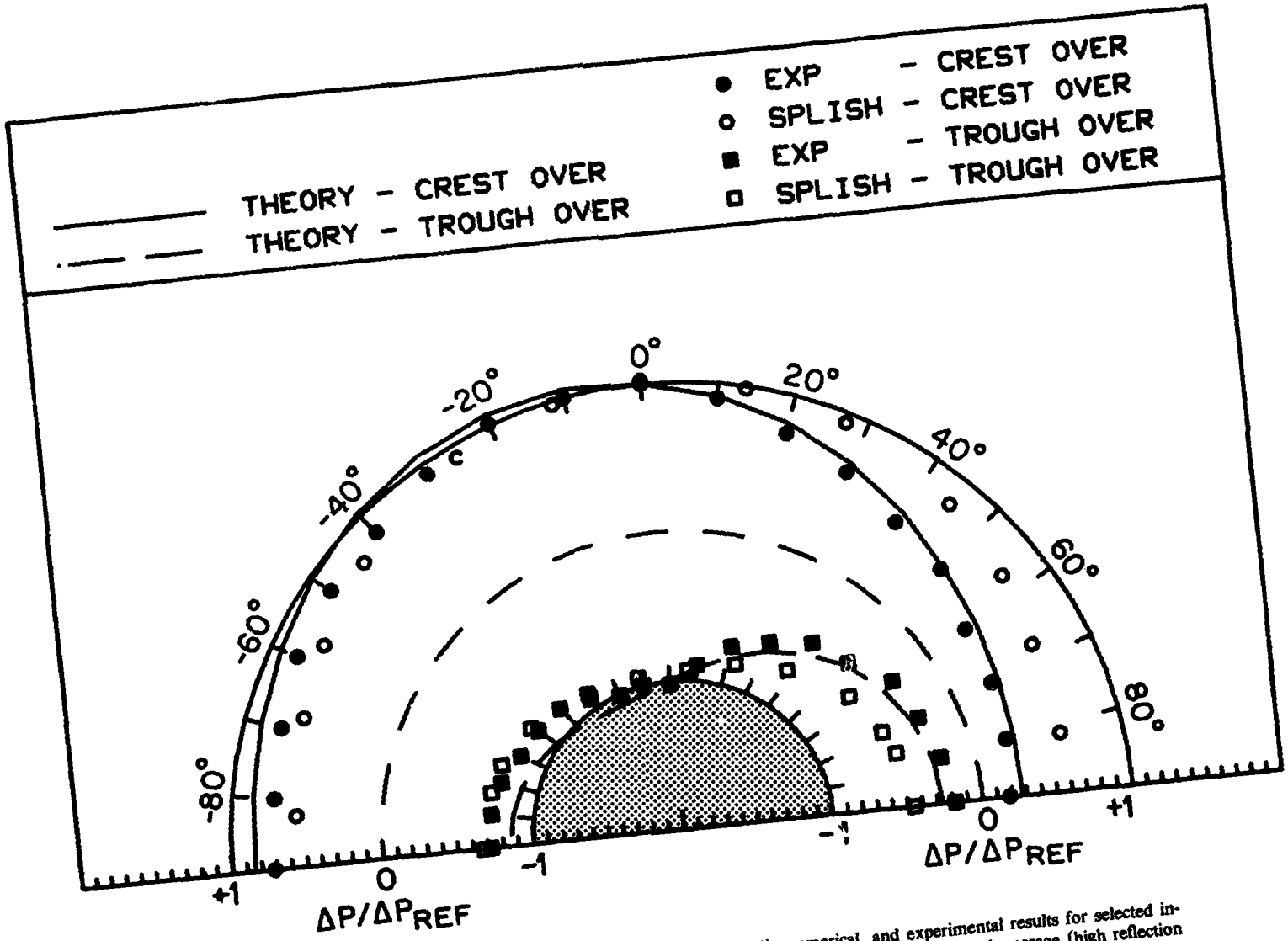

Figure 37. A comparison of theoretical (Naftzger and Chakrabarti, 1979), numerical, and experimental results for selected instantaneous pressure distributions on a bottom-seated half-cylinder in waves, for wave crest and trough passage (high reflection wave flow, $d/a = 1.5$, $ka = 0.5$, $R \approx 0.4$).

Figure 38. A comparison of theoretical (Naftzger and Chakrabarti, 1979), numerical, and experimental results for selected instantaneous pressure distributions on a bottom-seated half-cylinder in waves, for wave crest to the left and the right of the half-cylinder ($d/a = 1.5$, $ka = 0.5$, $R \approx 0.4$).

Appendix A

NUMERICAL METHODS AND ALGORITHMS FOR TRIANGULAR, LAGRANGIAN GRIDS

Numerical Methods

A Lagrangian treatment is particularly attractive due to the nature of the fluid flows of interest. For wave-body interaction problems the free surface may dominate the evolution of the flow, and the submerged or partially submerged bodies may move as well, so that a simple and accurate treatment of the flow near boundaries is essential. The strength of the Lagrangian formulation resides in the fact that fluid elements are advected with the flow. Therefore the grid points which define surfaces remain at those surfaces and permit the maximum accuracy in formulation of boundary conditions. The variation of grid resolution which must occur in Eulerian schemes as surfaces pass through cells is also alleviated and the numerical diffusion across boundaries minimized. Most importantly the nonlinear convective terms are not present in the Lagrangian formulation, resulting in higher accuracy and less stringent resolution requirements.

However, the great strength of the Lagrangian approach is also its greatest weakness. The advection of the mesh with the flow leads to large mesh deformations and a corresponding decrease in accuracy in both finite difference and finite element methods. We will first discuss the resolution of the problems associated with deformed grid resolution in standard Lagrangian computer codes. The deficiencies in earlier solutions are examined and an alternative solution is proposed and described. A detailed description of its properties, implementation and tests of accuracy are described in the next section.

Deformed Lagrangian Grids

To illustrate the effect of grid deformation let us examine first- or second-order accurate finite-difference methods. The mesh points commonly used to evaluate gradients and Laplacians are shown

in Figure A1a for a regular grid. Figure A1b illustrates a simple and common grid distortion produced by shear flow. A well-formulated Lagrangian finite-difference algorithm will properly account for the angles between grid lines and the variable mesh spacing produced by this distortion. Nevertheless, numerical approximations based on this mesh can still be grossly in error because differences no longer involve neighboring vertices. Mesh points now closer to the central vertex do not enter into the approximation, while those further removed do. As shown in Figure A2, higher order approximations may lead to even greater error. Figure A2a shows the vertices commonly used in higher-order approximations. Figure A2b illustrates that these approximations on a distorted mesh may include vertices which are even further removed from the central vertex while neglecting other vertices which lie closer. In other words the distorted mesh cannot be used to self-consistently improve the accuracy of the approximation. The problem can be resolved only by differencing over the appropriate vertices. That is, the mesh distortion must be reduced. This same conclusion holds true for the finite element method. Whether triangular or quadrilateral elements are chosen the accuracy on the deformed grid must be diminished regardless of the basis functions, simply because the grid joins the wrong vertices.

Rezoning

The traditional solution to this problem has been to perform an Eulerian rezoning phase which allows the mesh to pass through the fluid. For example, on a quadrilateral mesh a central vertex may be moved to the average position of its neighbors. The Eulerian motion of the vertex causes fluid to pass through the four quadrilateral cell sides meeting at that vertex, affecting the physical quantities specified in all four cells and the four neighboring vertices as well as the central vertex. The result of the rezone phase is therefore the introduction of artificial diffusion over one grid spacing in any direction. A related but separate question arises over the accuracy of the rezone algorithm. The rezone phase constitutes a separate Eulerian fluid flow calculation. In fluid flows with shear or near stagnation points the vertex motion accomplished during the rezone phase can be equal (and opposite) to the advective, Lagrangian vertex motion. In such cases the flow calculation is Eulerian. Unless the algorithms adopted for rezoning approach the accuracy available for finite-difference approximations of the

advective terms on an Eulerian mesh, the accuracy of the calculation is necessarily degraded and even more diffusive than a purely Eulerian calculation. A third objection to rezoning is that it is useless in fluid flows which force changes from simply-connected to multiply-connected regions, as in the case of wave-breaking or bubble collapse. In such cases no amount of rezoning can prevent mesh tangling and collapse of cells. A final fault of the rezone solution is that it does not address the proper questions. A grid deformation must force a less accurate approximation. Rezone algorithms generally seek to preserve a reasonable appearance of the grid and may obscure the question of what is the best approximation possible given the current Lagrangian vertex positions. That is, under the guise of preventing inaccuracies in the approximations, they may become the very vehicle for preserving them.

Although these remarks have been cast in the framework of finite difference techniques, they apply equally to Lagrangian finite element techniques (Strang and Fix, 1973). Regardless of the method used to calculate vertex velocities and accelerations, a Lagrangian mesh must distort and if a rezone phase is applied the same objections as to its accuracy, adequacy and appropriateness hold.

Reconnecting

The solution that rezoning offers to grid deformation is vertex motion to rectify the distortions. An alternate solution is illustrated in Figure A3. A section of a quadrilateral mesh about a shear layer is shown in Figure A3a. A Lagrangian calculation quickly leads to the mesh shown in Figure A3b, in which mesh connections about the layer no longer join neighboring vertices. In this figure one grid line has been reconnected to show the connection which is now appropriate. For a periodic system all stretched grid lines could be reconnected, thereby restoring the mesh to is original configuration *without* moving any vertices. In general, all such reconnections either are inappropriate or cannot be made due to boundaries, so that one triangular and one pentagonal cell remain. Therefore reconnection on a quadrilateral grid cannot by itself resolve the problem of distorted grids. On a triangular mesh, however, there are no such complications. As shown in Figure A4, a reconnected grid line on a triangular mesh still results in two triangular cells. This technique was first used in a computer code by Crowley (1971)

and represents a very attractive alternative to rezoning for triangular grids. There is no Eulerian vertex motion. For a given reconnection only one grid line or two cells are affected, instead of all the grid lines and cells about a given vertex in the rezone technique. Therefore at *most* diffusion is effectively over just one cell instead of two in either direction. The simplicity of the technique is particularly suited to considerations of how best to construct approximations given the current grid positions. As shown below, such questions result in very attractive conservative algorithms for the reconnection operation. Its major similarity with rezoning is that it cannot by itself solve the problem of fluids evolving into multiply-connected regions or of flows at stagnation points. However, it does aid in the remedy. The number of grid lines meeting at any vertex can be reduced to three by reconnections, with those three neighboring vertices forming a triangle which surrounds only that vertex. If the fluid is accumulating vertices locally, then that central vertex can be eliminated with the three grid lines, leaving only the surrounding triangle. The result is the desired decrease in resolution and the avoidance of the formation of thin, narrow triangles near the point of converging flow. Conversely, a vertex may be added inside any triangle or along any line simply by providing the necessary grid lines to other vertices within the affected triangles. Subsequent reconnections will link the added vertices to their neighbors. In this way the transition to multiply connected regions and the flow near stagnation points can be handled smoothly merely by decreasing or increasing resolution where appropriate. The combination of grid line reconnection with vertex addition and deletion therefore provide a means of smoothly restructuring the grid without recourse to Eulerian vertex movement.

The price that is paid for this flexibility is the loss of any global ordering for the vertices. A reconnecting grid has no fixed indexing. Partly because of this difficulty general triangular grids have not received the attention given to regular grids and are not as well understood. Solution procedures for irregular grids are currently more costly and the range of available numerical techniques is much more restricted. Fortunately grid alterations can be accommodated in finite-difference schemes with relatively mild calculational repercussions. For finite element schemes a reassembly of the system matrix is required whenever the mesh is restructured. For that reason we will focus on finite difference

techniques from this point on. The relative lack of experience in differencing over general triangular grids has historically led to some mistaken impressions, two of which are important enough to address directly — their "stiffness" and lack of accuracy.

Placement of variables

The assignation of "stiff" to triangular grids seems to have evolved from an improper placement of physical variables on the mesh. In a quadrilateral mesh, there is a one-to-one correspondence between cells and vertices. For example, each quadrilateral cell may be associated with its upper right vertex. The vertices remaining lie on boundaries, and their variables are specified by boundary conditions. If that same quadrilateral mesh is subdivided into a triangular mesh by drawing diagonals through each cell, it is clear the correspondence between cells and vertices is destroyed. The number of vertices is the same, but there are twice the number of cells. On the quadrilateral mesh it is attractive to assign pressures as cell-centered quantities, since pressure forces are easily calculated. Such a positioning on a triangular mesh can be disastrous. Twice as many pressures must be specified than in the well-formulated, quadrilateral case. Numerically, an iterative solution for pressures would converge extremely slowly, and in this sense the system of differenced equations would be stiff. If the idea of conserving cell size for incompressible flows is also carried over to triangular grids, the algorithms are stiff in a much worse sense. A vortex is shown in Figure A5, where the arrows designate local fluid velocities. All velocities are about the vortex center, and there exists a maximum speed at some radius from the center. The triangle that is shown will therefore eventually invert, since the vertex with the maximum speed must pass between the two more slowly moving vertices. If triangle areas are conserved, a pressure must build up to resist this tendency until the speeds of all vertices are commensurate with cell area conservation. The presence of such a pressure component at any stage of the calculation is totally non-physical, since it arises from improper placement of variables and is directly opposed to the physical flow. Such behavior is definitely "stiff" since the solution will tend to resemble solid body rotation rather than vortex motion. Such "stiffness" of triangular grids seems to be due entirely to such improper differencing.

The use of pressures defined on vertices will illustrate the second question, that of accuracy of difference schemes over a general triangular mesh. First let us incorporate our rather novel placement of pressures in the one-dimensional case. There are both forward and backward expansions of the pressure about the point i;

$$p_{i+1} = p_i + \frac{\partial p}{\partial x_i}\Delta x + \frac{1}{2}\frac{\partial^2 p}{\partial x^2}\Delta x^2 + \frac{1}{6}\frac{\partial^3 p}{\partial x^3}\Delta x^3 + O(\Delta x^4) \tag{A1}$$

and

$$p_{i-1} = p_i - \frac{\partial p}{\partial x_i}\Delta x + \frac{1}{2}\frac{\partial^2 p}{\partial x^2}\Delta x^2 - \frac{1}{6}\frac{\partial^3 p}{\partial x^3}\Delta x^3 + O(\Delta x^4). \tag{A2}$$

Of course the forward and backward difference approximations can be obtained directly from Equations A1 and A2;

$$\frac{\delta p}{\delta x_i} = \frac{p_{i+1} - p_i}{\Delta x} \tag{A3}$$

and

$$\frac{\delta p}{\delta x_i} = \frac{p_i - p_{i-1}}{\Delta x}. \tag{A4}$$

Both are only first-order accurate and can be viewed as cell-centered quantities. If instead Equations A1 and A2 are subtracted, the result is

$$p_{i+1} - p_{i-1} = 2\frac{\partial p}{\partial x_i}\Delta x + \frac{1}{3}\frac{\partial^3 p}{\partial x^3}\Delta x^3 + O(\Delta x^5). \tag{A5}$$

The centered difference approximation is then

$$\frac{\delta p}{\delta x_i} = \frac{p_{i+1} - p_{i-1}}{2\Delta x}, \tag{A6}$$

which is second order accurate and vertex centered. For the case of variable mesh spacing, we can replace Δx by $\Delta x'$ in Equation A2, so that Equation A5 becomes instead

$$p_{i+1} - p_{i-1} = \frac{\partial p}{\partial x_i}(\Delta x + \Delta x') + \frac{1}{2}\frac{\partial^2 p}{\partial x^2}(\Delta x^2 - \Delta x'^2) + O(\Delta x^3). \tag{A7}$$

Therefore

$$\frac{\delta p}{\delta x_i} = \frac{p_{i+1} - p_{i-1}}{(\Delta x + \Delta x')} \tag{A8}$$

which now has an accuracy between first and second order depending on the ratio $\Delta x/\Delta x'$, and which is evaluated neither directly at a vertex nor the cell center. If we rewrite Equation A4 using primes also, then Equation A8 can be rewritten as

$$\frac{\delta p}{\delta x_i} = \frac{\frac{\delta p}{\delta x_i}\Delta x_i + \frac{\delta p}{\delta x_i}\Delta x_i'}{\Delta x_i + \Delta x_i'}$$

or

$$\frac{\delta p}{\delta x_i} = \frac{\sum_{i=1}^{2} \frac{\delta p}{\delta x_i}\Delta x_i}{\Sigma \Delta x_i}. \tag{A9}$$

That is, the central difference can be obtained by an "area" weighted sum of the forward and backward differences.

This result carries over directly to general triangular grids in two dimensions. We can define the pressure gradient there as

$$\nabla p = \sum_{i=1}^{3} p_i \frac{\hat{z}x(\mathbf{r}_{i-1} - \mathbf{r}_{i+1})}{2A} \tag{A10}$$

where ∇p is the first order accurate, finite difference approximation to the gradient which is evaluated at the triangle centroid, A is the triangle area, $\hat{z}$ is a unit vector in the direction of the neglected coordinate and the sum extends over the three triangle vertices. The analogue of Equation A9 is

$$\nabla p_i = \frac{\sum_{j=1}^{n} \nabla p_j A_j}{\Sigma A_j} \tag{A11}$$

which for special geometries is second order accurate or higher. In general it is less then second order accurate, but performs reasonably close to second order accuracy for a general mesh provided that the triangle areas are roughly equal. In that case the error is determined by a formula similar to Equation A7, an algebraic sum of squared triangle altitudes. The worst that can be achieved is first order accuracy, which is obtained only in the degenerate case of a zero area triangle at the vertex. This implies that care must be taken in evaluating boundary conditions, but this task is alleviated by having the pressures specified at the boundaries. In a cell centered scheme, the pressures are located half a cell away,

and boundary conditions, particularly at free surfaces, are more difficult to implement. Accuracy in the interior of the fluid is therefore diminished primarily by narrow triangles. As shown below, this restriction is not too serious for a reconnecting grid since the grid can be made to reconnect to preserve regular triangles. In cases where this is not possible (near interfaces, for example), the grid addition or deletion vertices can be used to regularize the mesh.

The conclusion is that the "stiffness" and "diminished" accuracy of approximation on the triangular grid are both in large measure due to improper placement of physical variables on the mesh. Pressures as cell-centered quantities force not only a stiff solution, but make second-order accurate approximations difficult to achieve. Two other comments should be made about Equation A11. The first is that it can be used to recover all the usual gradient approximations for regular grids. An extension of the definition by taking the divergence of both sides of Equation A11 also yields all the usual Laplacian approximations (see below). The second feature of the equation is that the vertex pressure gradients can be viewed either as a sum over triangular gradients or in the more conventional way of a vertex sum. The former offers the possibility of vectorizing the equations even though the mesh has no inherent order, a fact which greatly enhances the utility of the method for the new vector computers.

Numerical Algorithms

The computer code SPLISH is a two-dimensional Lagrangian fluid dynamics code for incompressible fluids which was developed in accordance with the philosophy of the previous section (Boris et. al., 1975, and Fritts and Boris, 1977). The basic equations for incompressible fluid flow are

$$\rho \frac{d\mathbf{V}}{dt} = -\nabla p - \rho g \hat{y} \tag{A12}$$

and

$$\nabla \cdot \mathbf{V} = 0 \tag{A13}$$

where the fluid density ρ, pressure p and velocity $\mathbf{V}$ are assumed to vary only with x and y. With pressures specified at the vertices, ∇p is evaluated over triangles, and Equation A12 can easily be updated implicitly or explicitly if velocities are considered to be triangle-centered. This placement of velocities

as cell quantities and pressures at vertices is apparently unique to SPLISH and is the direct opposite of the usual placement. In what follows the subscript i will denote a vertex-centered quantity and j a triangle-centered quantity. In SPLISH the integration of velocities uses a split step algorithm whereby the velocities are advanced one half timestep (Equation A14), the grid is advanced a full timestep (Equation A16), and then the velocities advanced forward the other half timestep (Equation A18).

$$\mathbf{V}_j^{\frac{1}{2}} = \mathbf{V}_j^o - \frac{\delta t}{2\rho_j}(\nabla p)_j^o - \frac{\delta t}{2} g\hat{y}, \tag{A14}$$

$$\mathbf{V}_i^{\frac{1}{2}} = \frac{1}{2}(\mathbf{V}_i^o + \mathbf{V}_i^n), \tag{A15}$$

$$\mathbf{X}_i^n = \mathbf{X}_i^o + \delta t\, \mathbf{V}_i^{\frac{1}{2}}, \tag{A16}$$

$$\tilde{\mathbf{V}}_j^{\frac{1}{2}} = \mathbf{R}(\{\mathbf{X}_i^o\}, \{\mathbf{X}_i^n\}) \cdot \mathbf{V}_j^{\frac{1}{2}}, \tag{A17}$$

$$\mathbf{V}_j^n = \tilde{\mathbf{V}}_j^{\frac{1}{2}} - \frac{\delta t}{2\rho_j}(\nabla p)_j^n - \frac{\delta t}{2} g\hat{y} \tag{A18}$$

The vertex velocity $\mathbf{V}_i^n$ appearing in Equation A15 is obtained from the area-weighted $\mathbf{V}_j^n$ from the previous iteration,

$$\mathbf{V}_i^n = \frac{\sum_j \mathbf{V}_j^n A_j}{\Sigma A_j} \tag{A19}$$

The advantage of using triangle centered velocities is the ease in conceptualizing and expressing conservation laws. Because of the paucity of experience in formulating algorithms over a general triangular grid, we employed the control volume approach, which uses an integral formulation to derive the difference algorithms. Equation A17 is the first manifestation of this approach. It reflects numerically the fact that the triangle velocities must rotate and stretch as the grid rotates and stretches. The transformation R is derived by considering the circulation about each vertex. The boundaries of a vertex cell can be defined by apportioning each triangle equally to each of its vertices. One way of achieving this partitioning is to draw bisectors from the mid point of each side to the opposite vertex, as shown in Figure A6. The side bisectors meet at the centroid of the triangle and divide its area into six smaller equal area triangles. The areas of the two small triangles adjacent to each vertex are assigned to that vertex. The vertex cell of Figure A6 is constructed by summing over all the surrounding triangles.

Therefore the area of a vertex cell may be defined as

$$A_c = \sum_j \frac{1}{3} A_j \tag{A20}$$

where the sum extends over all adjacent triangles, exactly as in Equation A11. With this definition Equation A11 and Equation A19 become

$$\nabla p_i = \frac{\frac{1}{3}\sum_j \nabla p_j A_j}{A_{c_i}} \tag{A21}$$

and

$$\mathbf{V}_i = \frac{\frac{1}{3}\sum_j \mathbf{V}_j A_j}{A_{c_i}}. \tag{A22}$$

Since the triangle velocities are constant over the triangle, the circulation taken about the boundary of the vertex cell is straightforward. Circulation is conserved about each of the three triangle vertices by the transformation R of Equation A17. For constant velocities the transformation is linear and is given by the three equations;

$$\begin{aligned}
\tilde{\mathbf{V}}_j^{\frac{1}{2}} \cdot (\mathbf{X}_2^n - \mathbf{X}_1^n) &= \mathbf{V}_j^{\frac{1}{2}} \cdot (\mathbf{X}_2^o - \mathbf{X}_1^o), \\
\tilde{\mathbf{V}}_j^{\frac{1}{2}} \cdot (\mathbf{X}_3^n - \mathbf{X}_2^n) &= \mathbf{V}_j^{\frac{1}{2}} \cdot (\mathbf{X}_3^o - \mathbf{X}_2^o), \\
\tilde{\mathbf{V}}_j^{\frac{1}{2}} \cdot (\mathbf{X}_1^n - \mathbf{X}_3^n) &= \mathbf{V}_j^{\frac{1}{2}} \cdot (\mathbf{X}_1^o - \mathbf{X}_3^o).
\end{aligned} \tag{A23}$$

where the subscripts 1, 2 and 3 refer to the vertices associated with triangle j. This transformation ensures that the vorticity integral calculated about any interior vertex is invariant under the advancement of the grid. It is easy to show that the ∇p and gravity terms cannot alter the vorticity either since numerically $\nabla x \nabla p \equiv 0$ and gravity is a constant. Only the $\frac{\nabla p_j}{\rho_j}$ term can change vorticity, exactly as dictated by the physics. Since the transformation R is time reversible, so are Equations A14-A18, so that the entire algorithm advances vertex positions and velocities reversibly while evolving the correct vorticity about every interior vertex. No numerical generation of vorticity can occur, a rather unique feature of SPLISH among Lagrangian codes. The advantage of calculating triangle velocities is clearly evident in the simplicity of the transformation R, as well as in the reconnection algorithms, as shown below.

The pressure p_i^n in Equation A18 are derived from the condition that the new velocities V_j^n should be divergence free at the new timestep, satisfying Equation A13. The pressure Poisson equation is derived from Equation A18 by setting $(\nabla \cdot \mathbf{V}_j^n)_i \equiv 0$, to obtain pressure p_i^n such that

$$\frac{\delta t}{2}(\nabla \cdot \frac{1}{\rho_j}(\nabla p)_j^n)_i = (\nabla \cdot \tilde{\mathbf{V}}_j^{1/2})_i. \tag{A24}$$

The right hand side of Equation (A24) is the numerical analogue of the $\nabla \cdot (\mathbf{V} \cdot \nabla \mathbf{V})\delta t$ term which arises when the divergence of Equation A12 is taken. Both terms in Equation A24 are simple to evaluate since the divergence is taken over triangle centered quantities. The paths are the "surfaces" bounding the vertex volume of Figure A6, where the normal is directed outward from the vertex. The Poisson equation (Equation A24) that resulted from this integration has two advantages. First it is derived from $\nabla^2\phi = \nabla \cdot \nabla\phi$ as in the continuum case. Secondly the left-hand side results in the more familiar second order accurate templates (such as the five-point formula) for the Laplacians for homogeneous fluids and regular mesh geometries.

In summary the finite difference formulas for SPLISH are derived using a control volume approach. Specifications of pressure at vertices leads naturally to the choice of positioning velocities at triangles. Although pressure gradients are constant over triangles, the resultant algorithms are expected to be nearly second order accurate since vertex velocities are derived from pressure gradient forces through sums about vertices, which in effect takes the central differences. The code has been tested extensively on finite amplitude standing waves and has been shown to be basically second order accurate by the variation in period with mesh size (Fritts, 1976a and Fritts and Boris, 1979).

Grid restructing algorithms

The derivation of the reconnection and vertex addition and deletion algorithms is accomplished in the same manner through the control volume approach and the use of triangle velocities. The accuracy of a computer code which uses a reconnecting grid is determined by two aspects of the algorithms—how accurately post-reconnection physical variables are chosen and when the reconnections occur. As mentioned above, a reconnection offers the possibility of much less diffusion since fluid passes through only

one grid line for reconnections, whereas four grid lines are involved in every vertex rezone movement. Every mesh line can be viewed as one diagonal of the quadrilateral formed by the triangles to either side. A reconnection merely chooses the other diagonal. During a reconnection the smallest definable cell is the quadrilateral, not the two triangles, and it is necessary to ensure that quadrilateral properties are unchanged during a reconnection. That is, the quadrilateral is a control volume over which certain physical variables are conserved. As shown in Figure A7, a reconnection alters the vertex cells for each of the four quadrilateral vertices. To keep vorticity and divergence conserved the portions of the integrals $\int \nabla \cdot \mathbf{V} dV$ and $\int \nabla \times \mathbf{V} \cdot d\mathbf{A}$ about each vertex which lie within the quadrilateral must be the same before and after the reconnection. Since there are four velocity components to be specified after the reconnection, it would seem possible only to keep either the divergence or the vorticity about each vertex constant, but not both. However, the divergence and vorticity equations are not all independent and it is possible to exactly conserve both vorticity and divergence about each vertex with a unique set of triangle velocities. This same solution also conserves the quadrilateral velocity and has the added feature of time reversibility. Re-reconnecting a line yields the identical grid and physical variables both on vertices and triangles. This is extremely desirable since the basic finite-difference equations were also time reversible, as are the physical equations themselves.

The question of when to reconnect remains unresolved. As mentioned above, the accuracy of a general triangular mesh is diminished by narrow triangles. With reconnections, accuracy can be recovered by ensuring that small angles are preferentially eliminated. There are many ways of quantifying such an algorithm. The one we have chosen arises naturally from the pressure Poisson equation. Since the equation is solved in SPLISH by iteration, it is desirable that the convergence of the iteration be as rapid as possible. Mathematically, convergence is assured if the equation exhibits diagonal dominance. For a general triangle mesh diagonal dominance is obtained only if all coefficients

$$a = 1/2(\cot \theta^- + \cot \theta^+) \tag{A25}$$

are positive, where θ^+ and θ^- are defined in Figure A8a. For positive area triangles θ^+ and θ^- are both between 0° and 180°, so that each term is negative only when $\theta^+ + \theta^- > 180°$, since

$$a = \frac{\sin(\theta^+ + \theta^-)}{2\sin\theta^+\sin\theta-}. \tag{A26}$$

In SPLISH the reconnection algorithm is chosen to be exactly the algorithm needed to preserve diagonal dominance. If $\theta^+ + \theta^-$ is greater than 180°, the grid line is reconnected as shown in Figure A8b. The new angles θ'^+ and θ'^- must seem to less than 180° since $\theta^+ + \theta^- + \theta'^+ + \theta'^-$ is the sum of the interior quadrilateral angles, which must be 360°. Therefore the reconnection algorithm is unique as well as straightforward. It also preferentially eliminates small angles for triangles, since the diagonal is chosen which divides the largest opposing angles.

The second-order accuracy of SPLISH may be expected to be preserved, because the reconnection algorithms are specified to ensure diagonal dominance and eliminate small angle triangles. As yet no test has been made of the accuracy of the reconnection algorithms for the complete range of gridding situations. This is mainly because reconnections cannot themselves ensure second-order accuracy, since flows near stagnation points *must* force narrow triangles regardless. That is, vertex addition and deletion must be employed at the same time. The reconnection algorithms have been tested extensively, however, through the Kelvin-Helmholtz instability. In the linear, non-linear and turbulent regimes, the algorithms have been shown to provide accurate calculations by comparisons with both theory and experiment (Fritts, 1976b and Fritts and Boris, 1979).

The derivation of the remaining grid restructuring algorithms proceeds in exactly the same manner as above. For vertex addition satisfaction of conservation integrals is particularly simple. A vertex added at the centroid of a triangle subdivides that triangle into three smaller triangles. If the new triangle velocities are all the same as the velocity of the subdivided triangle, all conservation laws are trivially satisfied. Since the reconnection algorithm is also conservative, subsequent reconnections to other vertices ensure that the only effect of the addition is an increase in resolution.

The case is not as obvious for vertex deletion. Reconnections can be used to surround any interior vertex within a triangle. It can be shown, however, that once the vertex is surrounded by a triangle, the motion of that triangle is not altered if the vertex is removed and the new larger triangle given

a velocity which is the area-weighted sum of the old velocities,

$$A_4\mathbf{V}_4 = A_1\mathbf{V}_1 + A_2\mathbf{V}_2 + A_3\mathbf{V}_3. \tag{A27}$$

Such a substitution also conserves vorticity exactly, and effects a redistribution in accordance with area coordinates. Figure A9 illustrates the triangles before and after vertex removal. If ξ_4 is the vorticity about vertex 4 before removal, then the vorticity about each of the other three vertices is increased by an amount ξ'_i where

$$\begin{aligned} \xi'_1 &= A_j\xi_4/A_l \\ \xi'_2 &= A_k\xi_4/A_l \\ \xi'_3 &= A_i\xi_4/A_l \end{aligned} \tag{A28}$$

where $\xi'_1 + \xi'_2 + \xi'_3 = \xi_4$ since $A_i + A_j + A_k \equiv A_l$. Therefore total vorticity is conserved and redistributed in a reasonable and natural manner. Since the behavior of the divergence is governed by a similar set of equations and conservation of momentum is ensured by Equations A27, the conservation of the flow variables is guaranteed and a loss in resolution is the primary effect of deletion.

The vertex addition and deletion routines, together with the reconnection algorithms are incorporated in SPLISH through driving routines which test for large or small grid lines and large, small or skewed triangles, as well as special tests at boundaries and interfaces. The resultant code automatically restructures the grid under constraints in the form of a maximum allowable skewness and maximum and minimum areas and line lengths. The complete routine has been tested using the Rayleigh-Taylor instability and in flows about hydrofoils. Preliminary results of these tests are extremely satisfying, providing the first totally Lagrangian calculations of these phenomena at long times (Fritts, 1977 and 1979).

The tests performed using this code for the wave-structure interaction program are specifically aimed at the nonlinear free surface effects to answer the question of whether the code does indeed still behave as a basically second-order code and if the boundary conditions used thus far are realistic.

References

A1. Boris, J. P., K. L. Hain, and M. J. Fritts (1975). *Proceedings of the First Int'l. Conference on Numerical Ship Hydrodynamic*, NBS, Gaithersburg, Md.

A2. Crowley, W. P. (1971), *Proceedings of the Second International Conference on Numerical Methods in Fluid Dynamics*, Springer-Verlag

A3. Fritts, M. J. (1976), "A Numerical Study of Free-surface Waves." Science Applications, Inc. Report SAI-76-528-WA.

A4. Fritts, M. J. (1976). "Lagrangian Simulations of the Kelvin-Helmholtz Instability," Science Applications, Inc., Report SAI-76-632-WA.

A5. Fritts, M. J. and J. P. Boris (1977), "Solution of Transient Problems in Free-Surface Hydrodynamics," NRL Memorandum Report 3446.

A6. Fritts, M. J. (1977). "Transient Free-Surface Hydrodynamics." NRL Memorandum Report 3651.

A7. Fritts, M. J. and J. P. Boris (1979). "The Lagrangian Solution of Transient Problems in Hydrodynamics using a Triangular Mesh." *J. Comp. Phys.* Vol. 31, p. 173.

A8. Fritts, M. J. (1979), "Numerical Approximations on Distorted Lagrangian Grids," *Proceedings of the Third Int'l. Symposium on Computer Methods for Partial Differential Equations*, Bethlehem, Pa.

A9. Strang, G. and G. F. Fix (1973). *An Analysis of the Finite Element Method*, Prentice-Hall, p. 136.

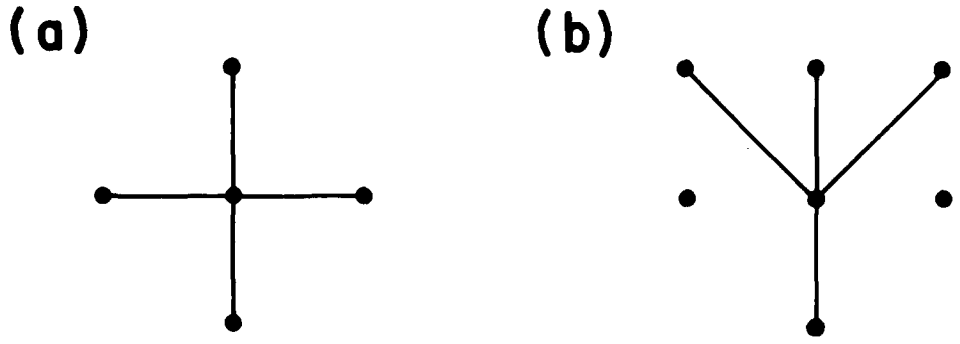

Figure A1. (a) Grid connections for a regular mesh, and (b) a distorted mesh formed by shear motion of the central column relative to its neighbors.

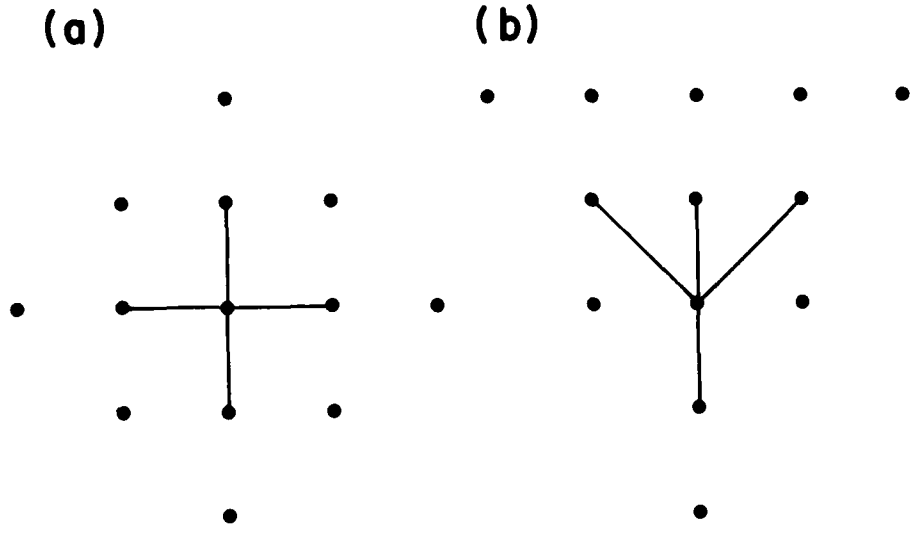

Figure A2. (a) Vertices used in higher order approximations. (b) The vertex positions on the mesh distorted by shear.

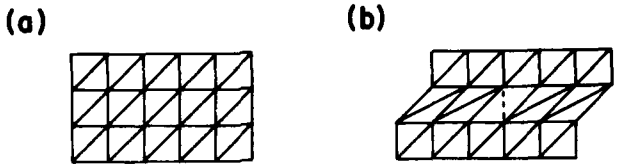

Figure A3. (a) A quadrilateral mesh about a shear interface. (b) Distortions induced in the Lagrangian mesh by the shear. A reconnection has been made to join nearest neighbors for a single vertex.

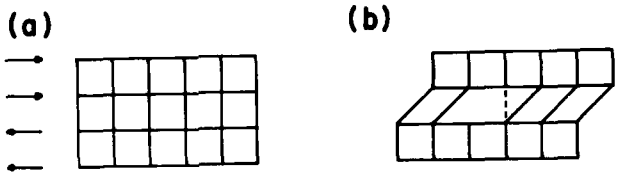

Figure A4. (a) A triangular grid formed by drawing diagonals through the mesh of Figure A3a. (b) The reconnection of Figure A3a on a triangular mesh.

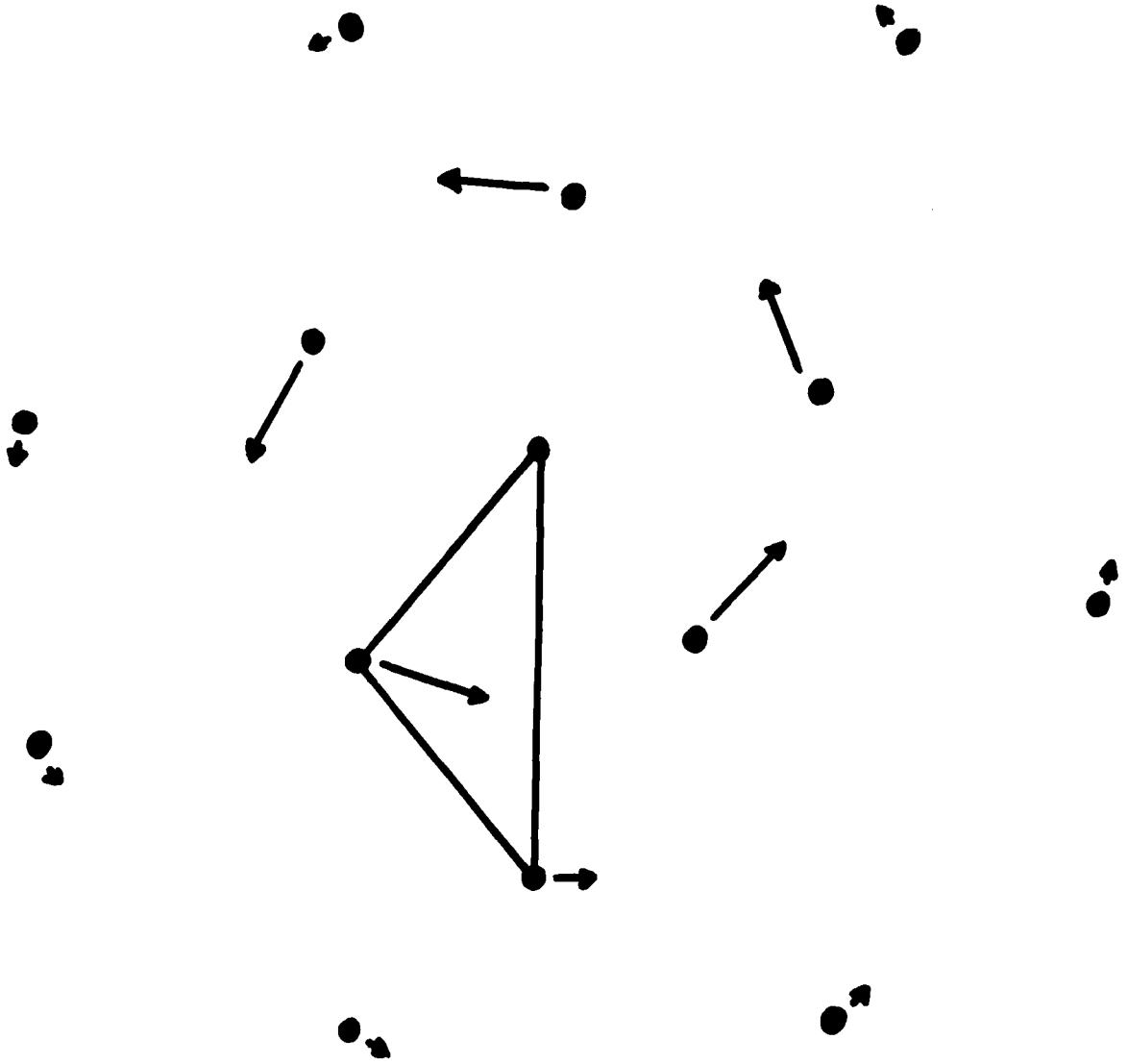

Figure A5. An isolated vortex about a central vertex. Velocities of neighboring vertices reach a maximum at some radius from the central vertex and diminish further out.

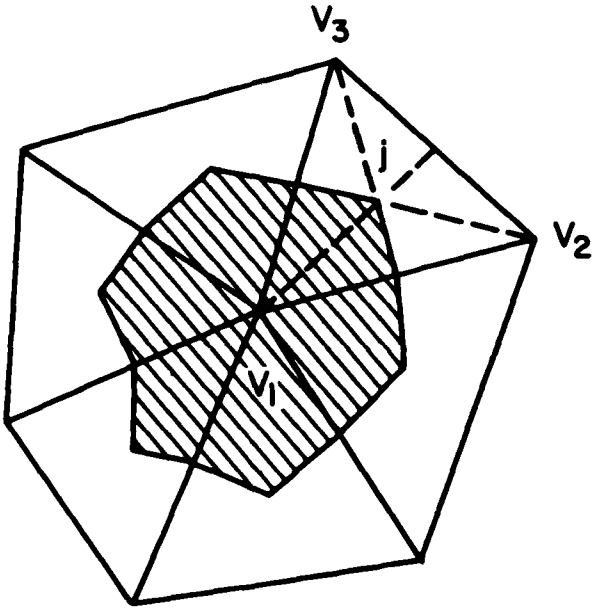

Figure A6. A definition of a vertex cell for a general triangular mesh.

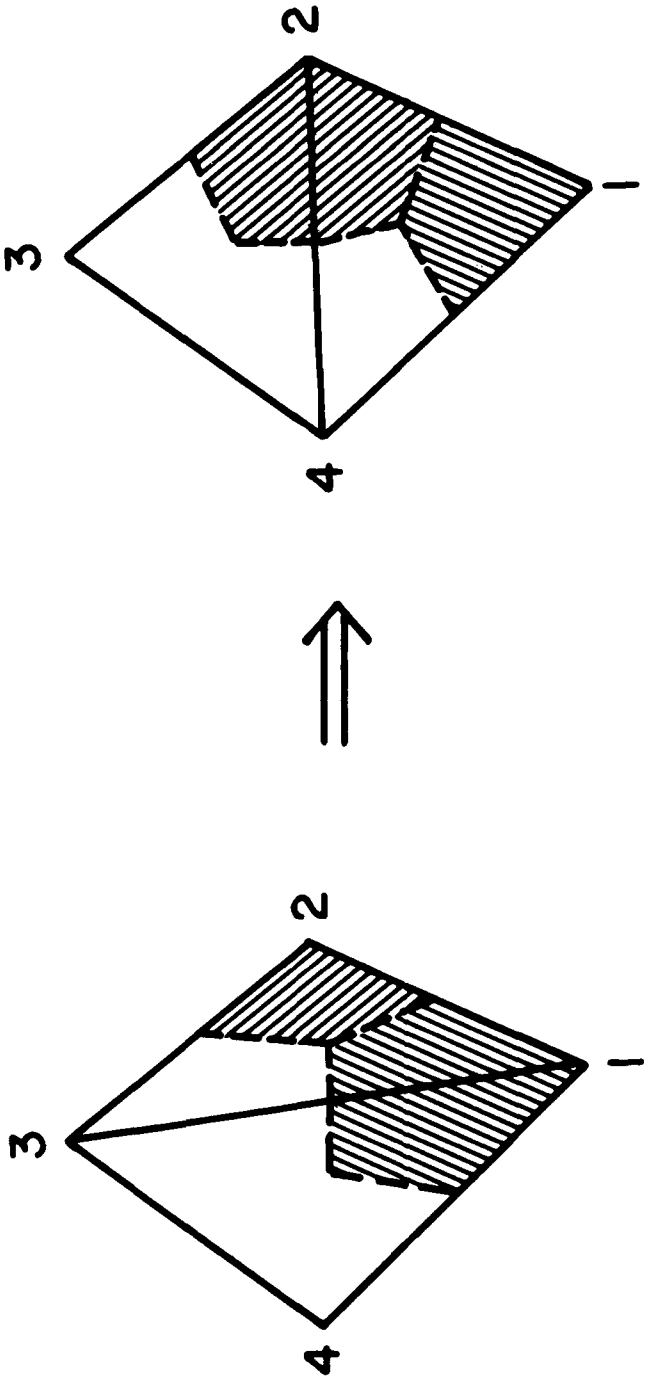

Figure A7. The vertex cells associated with two vertices before and after a reconnection.

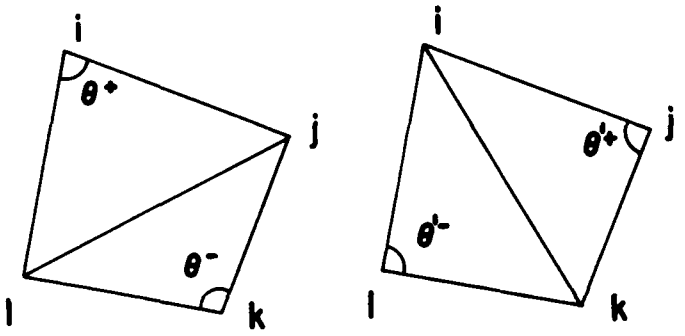

Figure A8. (a) Definition of the angles θ^+ and θ^- for the diagonal line drawn from j to l. (b) The angles θ'^+ and θ'^- formed by connecting the other quadrilateral diagonal.

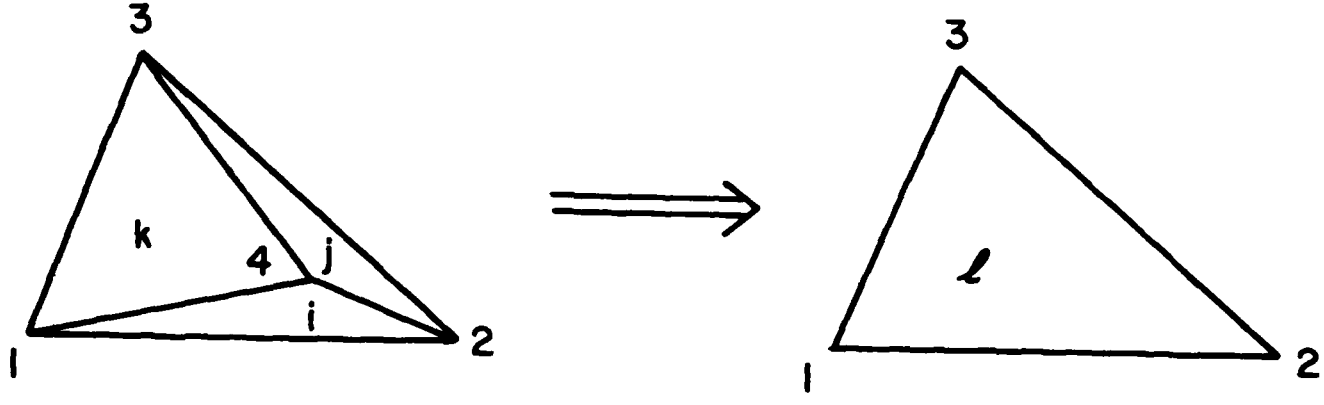

Figure A9. (a) Vertex 4 isolated within a larger triangle before its removal. (b) The larger triangle remaining after deletion of vertex 4 and three associated sides and triangles.

Appendix B

WAVE INDUCED FLUID PARTICLE MOTIONS

It is straightforward to compare the Lagrangian numerical computations with classical solutions to the equations of motion for inviscid, irrotational flow. Moreover, as demonstrated originally by Stokes (1847) and more recently by Phillips (1966), Newman (1977) and Longuet-Higgins (1980), it is convenient to derive the properties of the wave motion from existing Eulerian solutions and their Lagrangian analogues.

A two-dimensional coordinate system is chosen with $y = 0$ in the plane of the undisturbed free surface and with the y axis positive upwards. The positive x axis is taken from left to right in the direction of wave motion. If the velocity of a fluid element in Lagrangian terms is denoted by the vector $\mathbf{u}_l(\mathbf{a}, t)$, with the initial condition $\mathbf{x} = \mathbf{a}$ at $t = 0$, then the position of the element at a later time is

$$\mathbf{x} = \mathbf{a} + \int_0^t \mathbf{u}_l(\mathbf{a}, t)\, dt. \tag{B1}$$

The velocity $\mathbf{u}_l$ is given by the Taylor series expansion

$$\mathbf{u}_l(\mathbf{a}, t) = \mathbf{u}(\mathbf{a}, t) + \left(\int_0^t \mathbf{u}_l(\mathbf{a}, t)\, dt\right) \cdot \nabla_a \mathbf{u}(\mathbf{a}, t) + \ldots, \tag{B2}$$

where $\mathbf{u}(\mathbf{a}, t)$ is the Eulerian vector velocity and ∇_a is the gradient operator in the direction $\mathbf{a}$. To first order Stokes' solutions for the velocity fields are identical in Lagrangian and Eulerian terms, so that

$$\mathbf{u}_l(\mathbf{a}, t) = \mathbf{u}(\mathbf{a}, t) + \left(\int_0^t \mathbf{u}(\mathbf{a}, t)\, dt\right) \cdot \nabla_a \mathbf{u}(\mathbf{a}, t), \tag{B3}$$

correct to second order in the surface displacement amplitude. A wave with the displacement profile (where H is the wake amplitude)

$$\eta = H \cos(kx - \sigma t) \tag{B4}$$

from the undisturbed free surface is satisfied by the first-order Eulerian velocity potential

$$\phi(x, y) = \frac{\sigma H \cosh k(y + d)}{k \sinh kd} \sin(kx - \sigma t), \tag{B5}$$

and the corresponding dispersion relation

$$\sigma^2 = gk \tanh(kd) \tag{B6}$$

for water of uniform, finite depth d. Here σ denotes the wave frequency $\sigma = 2\pi/T$, where T is the wave period; and k denotes the wave number $k = 2\pi/\lambda$, where λ is the wavelength. For deep water waves with $d/\lambda \geq 0.5$ the dispersion relation reduces to $\sigma^2 = gk$. The expressions for the velocity potential and dispersion relation satisfy the continuity equation $\nabla \cdot \mathbf{u} = 0$, which reduces to Laplace's equation

$$\nabla^2\phi = 0 \tag{B7}$$

since $u = \frac{\partial\phi}{\partial x}$ and $v = \frac{\partial\phi}{\partial y}$. Also satisfied are the linearized boundary conditions

$$\text{Kinematic:} \quad \frac{\partial\phi}{\partial y} = \frac{\partial\eta}{\partial t} \tag{B8}$$

$$\text{Dynamic:} \quad \eta = -\frac{1}{g}\frac{\partial\phi}{\partial t} \tag{B9}$$

at the undisturbed free surface, $y = 0$. The normal velocity is assumed to vanish at the plane bottom, thus satisfying the additional boundary condition

$$v = \frac{\partial\phi}{\partial y} = 0 \text{ at } y = -d. \tag{B10}$$

The Eulerian fluid velocities which are obtained from this system of equations are

$$u = \frac{\partial\phi}{\partial x} = \frac{\sigma H \cosh k(y+d)}{\sinh kd} \cos(kx - \sigma t) \tag{B11}$$

and

$$v = \frac{\partial\phi}{\partial y} = \frac{\sigma H \sinh k(y+d)}{\cosh kd} \sin(kx - \sigma t). \tag{B12}$$

In Cartesian form the vector equation $\mathbf{u}_l = \left(\frac{dx}{dt}, \frac{dy}{dt}\right)$ for the Lagrangian velocity of a fluid particle with the initial position $\mathbf{a} = (x_o, y_o)$ is given by

$$\frac{dx}{dt} = u(x_o, y_o, t) + (x - x_o)\frac{\partial u}{\partial x_o} + (y - y_o)\frac{\partial u}{\partial y_o}, \tag{B13}$$

$$\frac{dy}{dt} = v(x_o, y_o, t) + (x - x_o)\frac{\partial v}{\partial x_o} + (y - y_o)\frac{\partial v}{\partial y_o}, \tag{B14}$$

correct to second order. Here the velocities u and v are given by Equations B11 and B12 evaluated at the point (x_o, y_o), and the first-order trajectories are given by

$$x - x_o = \int_0^t u(x_o, y_o, t)\, dt \tag{B15}$$

and

$$y - y_o = \int_0^t v(x_o, y_o, t)\, dt. \tag{B16}$$

An interesting finding that is derived from Equations B13 and B14 is the existence of a second-order mean motion of the fluid particles in the x direction. The particle paths are not closed and elliptical as in the first-order solution, but instead there is a slow, depth-dependent drift of the fluid particles in the direction of the wave motion. There is no mean flow in the y direction and v remains periodic, so that one obtains the mean velocities

$$\bar{u}_l = \frac{\sigma k H^2 \cosh 2k\ (y_o + d)}{2 \sinh^2 kd} \tag{B17}$$

$$\bar{v}_l = 0. \tag{B18}$$

This second-order mean motion in the direction of the wave propagation is often called the "Stokes drift."

References

B1. Longuet-Higgins, M. S. (1980), "Spin and Angular Momentum in Gravity Waves" *Journal of Fluid Mechanics*, Vol. 97, 1-24.

B2. Newman, J. N. (1977), *Marine Hydrodynamics.* MIT Press.

B3. Phillips, O. M. (1966), *The Dynamics of the Upper Ocean.* Cambridge University Press.

B4. Stokes, G. G. (1847), "On the Theory of Oscillatory Waves," *Transactions of the Cambridge Philosophical Society*, Vol. 8, 441-455, reprinted 1966, *STOKES: Mathematical and Physical Papers*, Vol. 1, 197-229, Johnson Reprint Corporation.

Appendix C

EXPERIMENTAL EQUIPMENT AND METHODS

The wave channel employed in the present experiments is housed in Building A59 at NRL. An overview of the channel, the wind generator, and the mechanical wave generator is shown in Figure C1. A photograph of the bottom-sealed half cylinder in the channel is shown in Figure C2. The channel is 30.5m (100 ft) in length and 1.22m (4 ft) wide, and the maximum water depth is 1.07m (3.5 ft). The regular waves required for the experimental program discussed in this report were generated by a bulkhead-type mechanical wavemaker driven by a variable-speed DC motor and a scotch yoke mechanism. A sloping beach is located in the channel at the opposite end from the wavemaker in order to absorb the incident waves. The beach is an open frame construction covered with porous acrylic plates and a rubberized hair blanket. This combination results in beach reflection coefficients (H_R/H_I) of 0.05 or less over most of the wavelength range of interest in the present experiments. Larger beach reflections were encountered in the longer wavelength experiments and this point is discussed later in this appendix. Details of the channel and the laboratory facility are given in another NRL report (C1).

Significant beach reflections ($\gtrsim$ 2%), in the absence of a submerged object, are readily detected as a modulation in waveheight along the channel (C2). In its simplest form, this amplitude modulation arises from the superposition of three linear progressive wave trains: the incident waves, the partially reflected waves, and the essentially total reflection of the latter waves by the wavemaker. The beach reflection coefficient R_b in this case is given by the modulation extremes arranged as (C2)

$$R_b = \frac{H_{max} - H_{min}}{H_{max} + H_{min}}, \tag{C1}$$

and clearly requires that any additional or secondary beach reflections are negligible, i.e. $R_b^2 << 1$. The same procedure can be used to determine the cylinder reflection coefficient R_c, however, secondary reflections tend to be significant depending, of course, on the magnitude of R_c^2. In fact one can easily

envision between the cylinder and the wavemaker a progression of higher order standing waves whose relative importance grows rapidly with increasing R_c.

A further complication arose in the present experiments because the beach performance was degraded at the longer wavelengths and lower water levels. Under those conditions, the waves transmitted by the cylinder were partially reflected by the beach and returned to strike the "back" of the submerged half-cylinder. The initial transmitted waves, denoted by the transmission coefficient T and satisfying the energy balance (C3)

$$T^2 = 1 - R_c^2, \tag{C2}$$

are themselves transmitted and reflected by the cylinder. This gives rise to additional standing wave components in front of and behind the cylinder. The essential difficulty in this type of laboratory experiment is clear. Each wave train that is incident upon the cylinder produces two outgoing wave trains which are returned either partially or totally to establish two additional standing wave components and two additional incident waves for the next interactions. It is important to note that only part of this difficulty is associated with large beach reflections and, in fact, large corrections will be required for seemingly simply cases. For example, consider a case where $R_b = 0.05$, acceptable by common standards, and $R_c = 0.10$. A modulation measurement on the wavemaker or upstream side of the half cylinder includes not only a standing wave due to cylinder reflection but also a comparable standing wave due to transmission past the cylinder and to beach reflection. An expression for the observed modulation coefficient R_m in this instance can be found by an extension of the earlier simple method (C2) and is of the form

$$R_m^2 = R_c^2 + (R_b\ T^2)^2 + 2R_c R_b T^2 \cos\phi \tag{C3}$$

where ϕ is the phase angle between the two standing waves. The difference between the observed modulation coefficient and the actual cylinder reflection for the above example can be nearly as much as $\pm$ 50 percent. This equation was employed to determine the cylinder reflection coefficients shown in Figure 32. The waveheight modulations and relative phases, with and without the cylinder in place, were obtained from stripchart recordings of the output from a pair of traversing, capacitance-type wave

gages. For the present ranges of wave steepnesses and reflection coefficients, second harmonic corrections to the modulation measurement (C3) were considerably smaller than the above correction and therefore were neglected. It is important to note, however, that the above method neglects secondary reflections by the assumptions that R_b^2, R_c^2, and R_bR_c are all much less than unity. This was not the case during the experiments, and, in fact, the discrepancies in Figures 33 and 36 are comparable to these quantities for each case.

The wave-induced pressures on the submerged half-cylinder were obtained from nineteen equally-spaced ($\Delta\theta = 10°$) pressure taps located around the circumference of the cylinder at its midsection. The individual taps were connected to a differential pressure transducer (Celesco P7D) by a 24 position, remotely-operated, rotary pressure switch (Scanivalve). The extra switch positions were used to obtain the wave-induced pressures away from the cylinder and to purge the lines of air by means of a solenoid valve arrangement. The resolution of the pressure measurements was enhanced by approximately balancing the relatively large hydrostatic pressure with a separate column of water connected to the reference side of the pressure transducer. Calibration of the pressure sensor was achieved by varying this reference pressure over a known range. The pressure signals were digitized and processed for each tap position by means of a Hewlett-Packard 5420A Digital Signal Analyzer. The signal magnitudes and their relative phases were obtained from the autospectra and cross-correlation (phase) functions, respectively. The overall accuracy of the measurement system was better than 5 percent. Instantaneous pressure distributions were reconstructed from the measured distributions of the pressure fluctuation magnitudes and relative phases. The presence of additional waves in the channel, as described earlier, often had a large influence on the measured pressures and this was taken into account by removing the unwanted wave contribution(s) according to linear wave theory and by using the observed wave modulation envelopes both upstream and downstream of the cylinder.

REFERENCES

C1. Griffin, O.M. and J.W. Wright (1976), "A New Wave-Wind Channel for Fluid Dynamics Research at the Naval Research Laboratory" NRL Memorandum Report 3352.

C2. Ursell, F., R.G. Dean and Y.S. Yu (1959), "Forced small-amplitude water waves: a comparison of theory and experiment" Journal of Fluid Mechanics, Vol. 7, 33-52.

C3. Madsen, O.S., and White, S.M. (March 1976), "Reflection and Transmission Characteristics of Porous Rubble-Mound Breakwater," Coastal Engineering Research Center Report No. 76-5.

AD-A093 109 NAVAL RESEARCH LAB WASHINGTON DC F/G 13/10
NUMERICAL CALCULATION OF SURFACE WAVE EFFECTS ON MARINE STRUCTU--ETC(U)
DEC 80 E W MINER, O M GRIFFIN, S E RAMBERG
UNCLASSIFIED NRL-MR-4395 NL

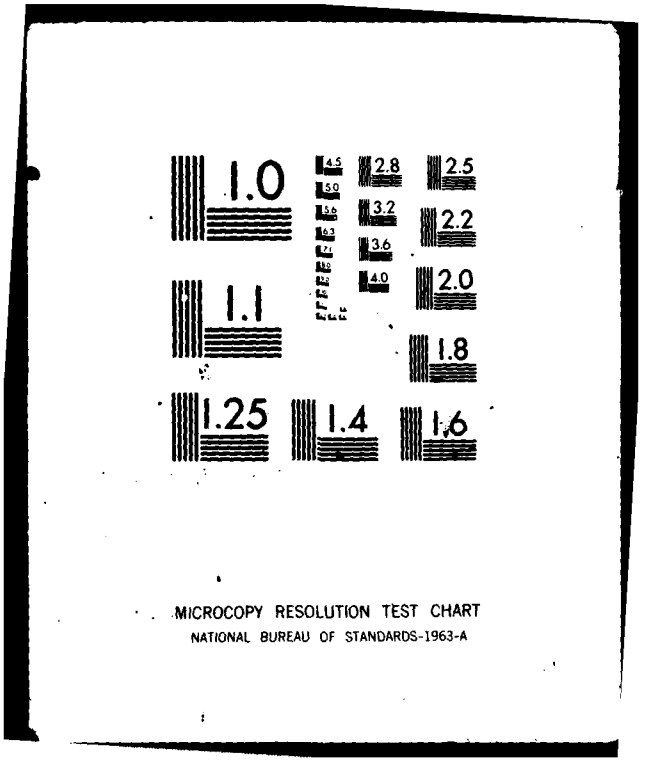

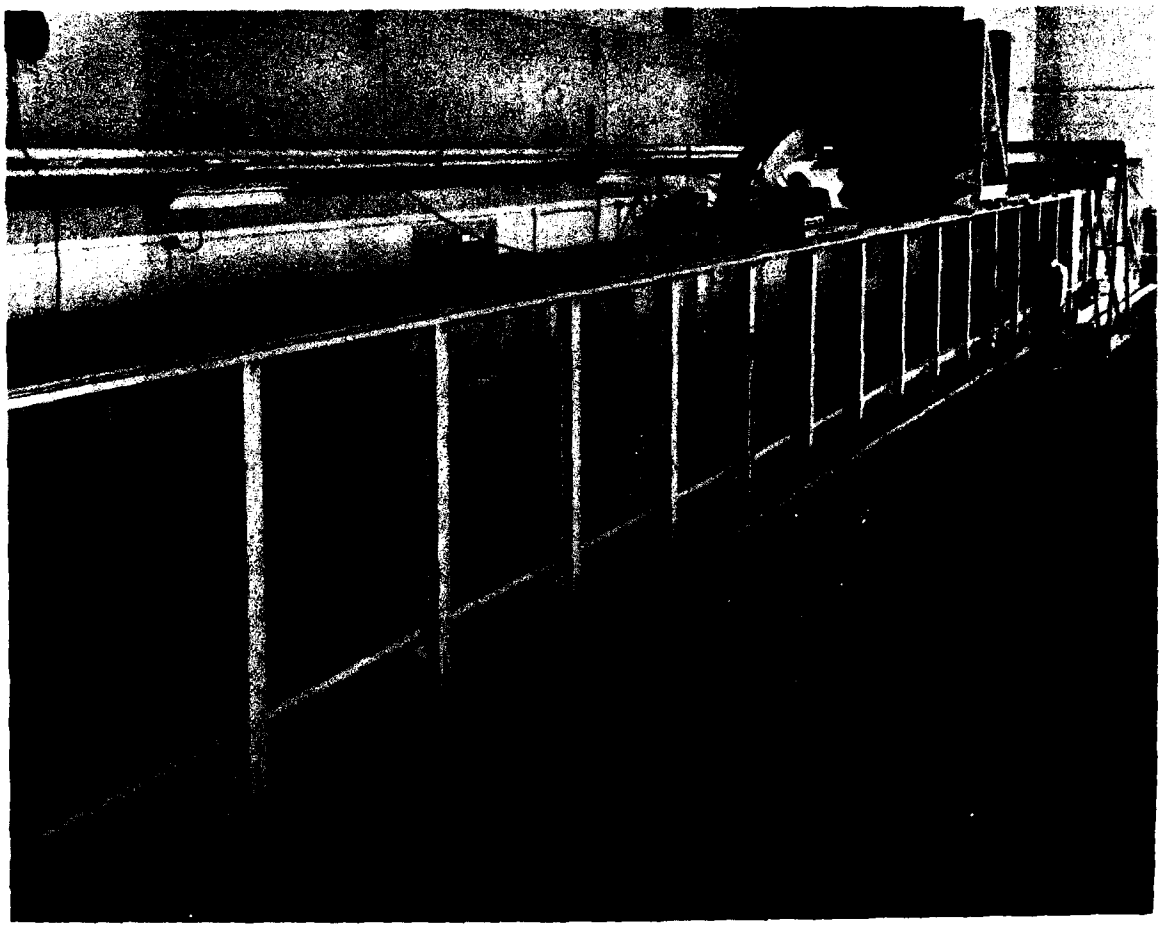

Figure C1 – An overview of the NRL wave channel and laboratory.

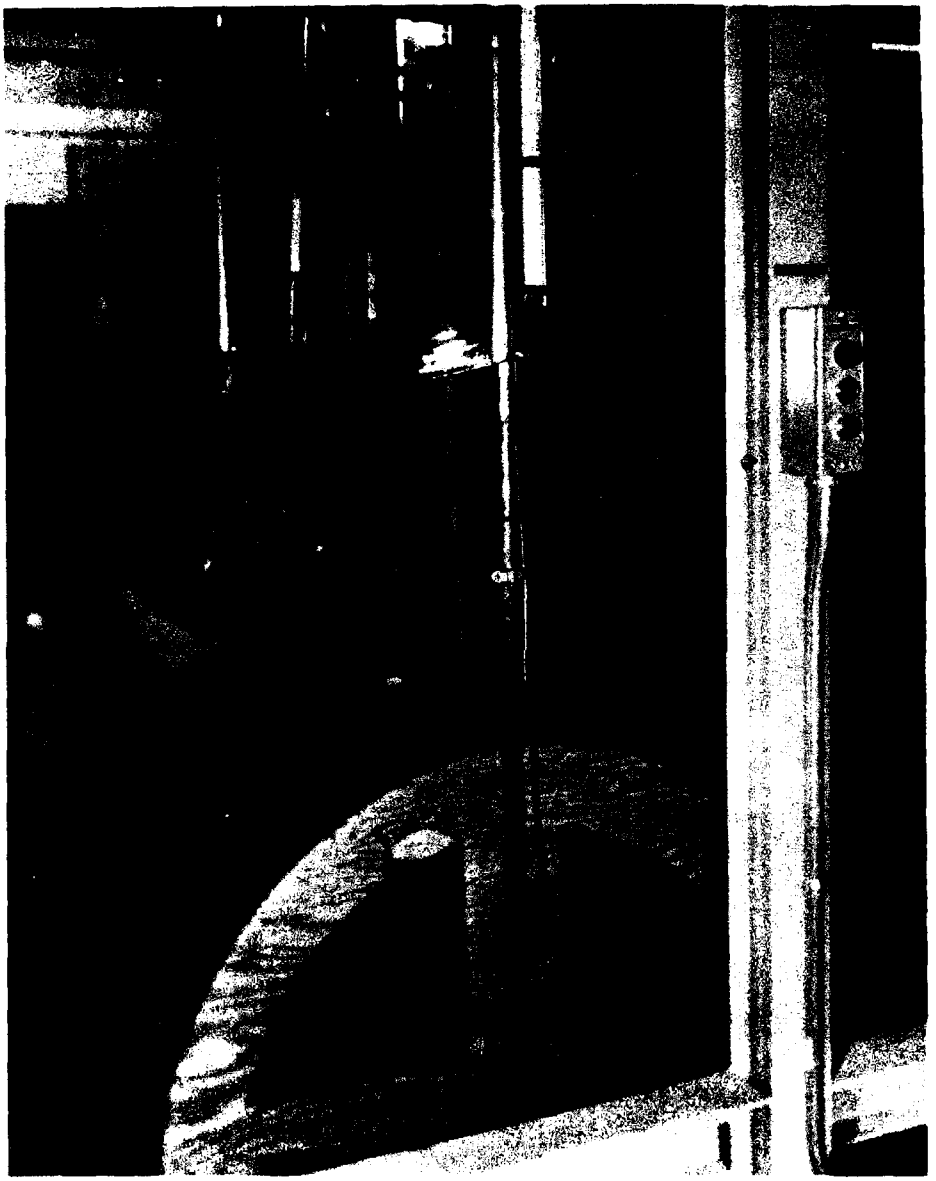

Figure C2 – A photograph of the bottom seated half-cylinder in the wave channel.

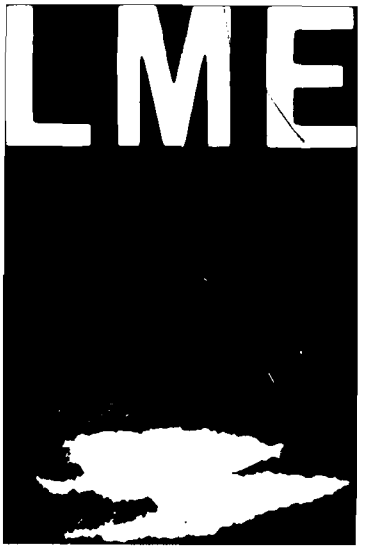
LME